Self-Consistent Modelling of Non-Thermal Atmospheric Argon Plasma During Arc Discharge and Its Interaction with Metal Electrodes

Vom Fachbereich Produktionstechnik

der

UNIVERSITÄT BREMEN

zur Erlangung des Grades
Doktor-Ingenieur
Genehmigte

Dissertation

von

M.Sc. Peng Liang

Gutachter: Prof. Dr. rer. nat. Claus Lämmerzahl
Prof. Dr.-Ing. Johannes Kiefer

Tag der mündlichen Prüfung: 9. Juli 2018

Acknowledgements

After over four years of dedicated research and intensive trial and error work in coding and debugging with my sometimes annoying but at the same time the most intimate “working partner” OpenFOAM, I am very lucky to sit in front of my computer to write down what I’ve achieved with pain and joy. The famous German proverb by Bertolt Brecht tells me:” Wer kämpft, kann verlieren. Wer nicht kämpt, hat schon verloren. “It always gives me support and power when I failed to get satisfactory results and felt exhausted after almost hundreds and thousands of times of adjusting boundary conditions, parameter values or editing transport equations. But when someone asks me if I had regretted. The answer is always no.

The persons to whom I shall give my sincere thankfulness at first are my supervisor Prof. Claus Lämmerzahl and Dr. Rodion Groll. They gave me such a splendid chance to conduct my scientific research and pursue my Ph.D. degree in a such splendid institute and country. Besides, they’ve provided me with all the possible helps and instructions they could in both my life and research.

Secondly, I’d like also to convey my thanks to China Scholarship Council to have given me three years of financial support during my research in Germany. I think the best way that I can repay is to use all I have learned here to make contributions to my motherland.

Besides, I will give my gratefulness to some team members of Rodion, namely Charles, Till, Christoph, Andre and colleagues from other groups such as Zeli and Diana. Their helpfulness, kindness and above all the erudition have impressed me a lot and made my stay in Germany most colorful and unforgettable.

My special thank goes to my dear colleague, Dr. Jakob Hauschildt. He has been my indispensable friend and tutor during the last three years, gave me all kinds of the academic advises, suggestions or sometimes even the very solutions directly that he had. He has told me how to be a real researcher, and the courage and attitude a researcher should have when facing problems and how to solve them in my own way. I will never forget what he has taught me and will always follow the example he has set in the rest of my academic life.

Finally, I will give my greatest thankfulness to my parents, who always stand by my side, support me and give me warmness to help me overcome all the obstacles.

Abstract

Heat transfer processes associated with arc plasmas are important for many industrial applications such as electric propulsion, plasma spray and arc welding. In these applications, an electric arc is used because it offers high energy densities and a controlled environment. However, it is sometimes not realizable or not economic to get the parameters within the high temperature region of plasma precisely by means of experimental measurements. A numerical model that offers reliable description of discharging process is a good choice. Any model of arc plasmas must contain not only the conservation of mass, momentum and energy, but also electromagnetic description that follows Maxwell's equations. Since the last 30 years, intensive researches embarking on nonequilibrium plasmas have led to fruitful achievements, among them NLTE (non-Local Thermal Equilibrium) model plays an important role in numerical modelling due to its superiority over LTE (Local Thermal Equilibrium) model in accounting for the difference of two phase temperatures (heavy species and electrons) that cannot be neglected near electrodes. However, deeper researches meet obstacles when the discharging system needs to be simulated self-consistently as a whole and with as few presumed conditions as possible. On one hand, discharging under high current operation tends to overheat its electrodes leading to melting or evaporating, particles from electrode material that enter the plasma will change its composition and the heat transfer process. On the other hand, there's still a "mysterious" region whose physical structure is so different from the main arc plasma region that cannot be accounted by conventional transport equations or theories without any extra treatments for it. This region, sometimes called sheath layer or space-charge layer, plays an important role in bridging the thermal and electric energy of arc column to electrodes. To develop a reasonable model in this region and make it compatible with the two other regions will extend the applicability of CFD model in discharging devices. The motivation of this doctoral thesis is based on my special interest in sheath region, or in other words, my pursuit of developing a self-consistent model that is capable of solving the whole plasma-electrode system. Concerning the complexity of sheath, no secondary physical phenomena such as melting and evaporating are considered in this study. For the main arc region, the plasma composition is calculated based on species conservation equations that consider both diffusion and production/loss activities of particles. And for the sake of high temperature of plasma core, ionization up to third level is applied. In the sheath layer, the effective sheath electrical conductivity is utilized, which is based on the assumption of Child's collisionless sheath and Lowke's expression. The ionization degree of plasma sheath plays an important role in this self-consistent method. To validate the model proposed here, several simple benchmark simulations are made and the numerical results concerning temperature, velocity and magnetic field yield satisfactory agreements with experimental or theoretical results. With the model being validated, a D.C. non-transferred plasma torch is studied. The total voltages of both situations are compared with experimental measurements. It shows that the sheath model developed in this scope make the numerical results closer to reality and is responsible for the strong fluctuation of arc jets, which also makes cathode surface temperature fluctuate accordingly. Finally, pros and cons of some new design patterns of plasma torches are discussed, with the multi anode/single cathode type *DeltaGun* simulated for the comparison of performances with the original type. It reveals that such kind of configuration helps to damp the unwanted arc fluctuation with multiple arc roots. It is also numerically confirmed that when an external coil is added around anode to produce a proper magnetic field, the temperature of anode attachment can be reduced due to enhanced circumferential movement of arc roots by Lorentz force, which lowers the possibility of erosion and promotes a longer lifetime.

Zusammenfassung

Wärmeübertragungsprozesse, die mit Lichtbogenplasmen verbunden sind, sind wichtig für viele industrielle Anwendungen, wie etwa elektrische Antriebe, Plasmaspritzen und Lichtbogenschweißen. Bei diesen Anwendungen wird ein Lichtbogen verwendet, da er hohe Energiedichten und eine kontrollierbare Umgebung bietet. Es ist jedoch manchmal nicht realisierbar oder nicht wirtschaftlich, die Parameter innerhalb des Hochtemperaturbereichs des Plasmas präzise mittels direkter Messungen zu ermitteln. Dieses Problem kann jedoch durch eine numerische Simulation, die eine zuverlässige Beschreibung des Entladeprozesses liefert, gelöst werden. Jedes Modell von Lichtbogenplasmen muss nicht nur die Erhaltung von Masse, Impuls und Energie enthalten, sondern auch die Beschreibung der elektromagnetischen Phänomene, die den Maxwell-Gleichungen genügt. Seit den letzten 30 Jahren haben intensive Forschungen, die sich mit Nichtgleichgewichtsplasmen befassen, zu fruchtbaren Erfolgen geführt: dabei spielt das NLTE-Modell (Non-Local Thermal Equilibrium), welches dem LTE-Modell (Local Thermal Equilibrium) überlegen ist, eine wichtige Rolle, da dieses die beiden Phasentemperaturen (von schwere Spezies und von Elektronen), die in der Nähe von Elektroden auftreten und deren Unterschiede nicht vernachlässigt werden dürfen, genau modellieren kann. Falls das Entladesystem als Ganzes und mit möglichst wenig angenommenen Bedingungen selbstkonsistent simuliert wird, treten Schwierigkeiten auf: Zum einen neigen die Elektroden beim Entladen unter Hochstrombetrieb dazu zu überhitzen, was zum Schmelzen oder Verdampfen dieser Elektroden führt, wodurch Teilchen aus dem Elektrodenmaterial in das Plasma gelangen und damit dieses und den Wärmeübertragungsprozess verändern. Darüber hinaus gibt es dabei immer noch einen bestimmten Bereich, innerhalb dessen die physikalischen Eigenschaften der Plasma-Randschicht sich von den üblichen Eigenschaften des Plasmas so stark unterscheiden, dass diese nicht mit konventionellen Transportgleichungen oder Theorien ohne zusätzliche Annahmen erklärt werden kann. Diese Plasma-Randschicht, auch Raumladungsschicht genannt, spielt eine wichtige Rolle bei der Überbrückung der thermischen und elektrischen Energie der Lichtbogensäule zu den Elektroden. Die Entwicklung eines vernünftigen Modells in dieser Region zusammen mit der Kompatibilität mit den beiden anderen Regionen wird die Anwendbarkeit des CFD-Modells in Entladungsvorrichtungen erweitern. Die Motivation dieser Doktorarbeit liegt somit darin, ein selbstkonsistentes Modell zu entwickeln, das in der Lage ist, das gesamte Plasma-Elektrodensystem zu lösen. Aufgrund der Komplexität der Plasma-Randschicht werden in dieser Arbeit sekundäre physikalische Phänomene wie Schmelzen und Verdampfen nicht berücksichtigt. Für den Plasmakern wird die Plasmazusammensetzung vermöge der Erhaltungsgleichungen bestimmt, die sowohl die Diffusion als auch Erzeugung und Verluste von Teilchen berücksichtigen. Wegen der hohen Temperatur des Plasmakerns wird die Ionisation bis zum dritten Grad berücksichtigt. In der Grenzschicht wird die effektive elektrische Leitfähigkeit verwendet, die auf der Annahme von Childs stoßfreier Plasmagrenzschicht und der Lowkeschen Formel basiert. Der Ionisationsgrad der Grenzschicht spielt bei dieser selbstkonsistenten Methode eine wichtige Rolle. Um das hier vorgeschlagene Modell zu validieren, werden mehrere einfache Benchmark-Simulationen durchgeführt. Die numerischen Ergebnisse bezüglich Temperatur, Geschwindigkeit und Magnetfeld ergeben eine zufriedenstellende Übereinstimmung mit den experimentellen oder theoretischen Ergebnissen. Mit dem validierten Modell wird ein Lichtbogenplasmabrenner mit nichtübertragenem Bogen unter Gleichstrom untersucht. Die Gesamtspannungen dabei werden einmal mit und ohne Plasmarandschichtmodell simuliert und mit experimentellen Messungen verglichen. Es zeigt sich, dass die numerischen Ergebnisse des entwickelten Randschichtmodells die Realität besser beschreiben, insbesondere auch die starke Fluktuation der Lichtbogenstrahlen, aufgrund derer die Temperatur an den Kathodenoberflächen entsprechend schwankt. Abschließend werden die Vor- und Nachteile einiger neuer Designmuster von Plasmabrennern diskutiert, wobei *DeltaGun* mit drei Anoden und Einzelkathoden simuliert wird, um die Leistungen mit dem Originaltyp zu vergleichen. Es zeigt sich,

dass eine solche Konfiguration dazu beiträgt, die unerwünschte Bogenschwankung mit mehreren Lichtbogenwurzeln zu dämpfen. Es wird auch numerisch bestätigt, dass, wenn eine externe Spule um die Anode herum hinzugefügt wird um ein richtiges Magnetfeld zu erzeugen, die Temperatur der Anodenbefestigung aufgrund der verstärkten Umfangsbewegung der Lichtbogenwurzeln durch Lorentzkraft verringert werden kann, was die Möglichkeit von Erosion verringert und eine längere Lebensdauer ermöglicht.

Table of Contents

Nomenclature

Name	Description	Units
$\vec{A}$	Magnetic vector potential	V·s·m^{-1}
A	Voltage fluctuation ratio	—
A_G	Material-specific constant of Richardson-Dushman current	A·m^{-2}·K^{-2}
$\vec{B}$	Magnetic field	T
B_λ	Spectral radiance in wavelength	W·sr^{-1}·m^{-3}
c_p	Specific heat at constant pressure	J·kg^{-1}·K^{-1}
C_o	Courant number	—
e	Elementary charge, e=1.6022× 10^{-19}	C
e_{in}	Specific internal excitation energy	J·kg^{-1}
e_{io}	Specific reactive energy	J·kg^{-1}
$\vec{e}$	Iteration error vector	—
$\vec{E}$	Electric field	V·m^{-1}
E_c	Electric field magnitude at cathode surface	V·m^{-1}
E_i	Ionization potential of heavy species i	J
E_1^*	The first excitation energy	J
∇E_i	Lowering of ionization potential	J
f_H	Oscillation frequency in cathode cavity	s^{-1}
G	Incident radiation intensity	W·sr^{-1}
h	Planck's constant, h=6.625× 10^{-34}	J·s
h_e	Specific enthalpy of electrons	J·kg^{-1}
h_h	Specific enthalpy of heavy species	J·kg^{-1}
h_s	Specific enthalpy of metal electrodes	J·kg^{-1}
H_a	Hartmann number	—
I	Identity tensor	—
I_g	Ionization degree	—
$\vec{J}$	Current density	A·m^{-2}
$\vec{J}_{D,i}$	Mass diffusion flux of species i	kg·m^{-2}·s^{-1}
$\vec{J}_{D,\mathrm{e}}$	Mass diffusion flux of electron	kg·m^{-2}·s^{-1}
J_0	Child-Langmuir law of space-charge-limited current density	A·m^{-2}
J_i	Ion current density	A·m^{-2}
J_{em}	Thermionic emission current density	A·m^{-2}
J_{sem}	Secondary emission current density	A·m^{-2}
J_{bd}	Back diffusion current density	A·m^{-2}
J_s	Magnitude of electrode current density	A·m^{-2}
$\vec{J}_{ex}$	External coil current density	A·m^{-2}
k	Turbulence kinetic energy	J·kg^{-1}
k_B	Boltzmann's constant, k_B=1.38× 10^{-23}	J·K^{-1}
k_λ	Spectral absorption coefficient in wavelength	m^{-1}
$k_{b,i}$	Recombination rate of heavy species i	m^6·S^{-1}
$k_{f,i}$	Ionization rate of heavy species i	m^3·S^{-1}
k_n	Knudsen number	—
K_i	Constant of Saha equilibrium	m^{-3}
L	Characteristic length	m
m_h	Mass of heavy species	kg

m_e	Mass of electron, m_e=9.11× 10^{-31}	kg
$\dot{m}$	Inlet mass flow rate	kg· s^{-1}
n_e	Electron number density	m^{-3}
n_i	Number density of heavy species i	m^{-3}
n_p	Ion number density at plasma-presheath interface	m^{-3}
n_s	Ion number density at presheath-sheath interface	m^{-3}
p	Plasma static pressure	Pa
p_e	Partial pressure of electron	Pa
p_h	Partial pressure of heavy species	Pa
p_0	Atmospheric pressure, p_0=1.013× 10^5	Pa
P_i	Binding energy of electrons in i-th subshell	J
q_a	Heat flux density at anode surface	W·m^{-2}
q_c	Heat flux density at cathode surface	W·m^{-2}
q_R	Radiative heat flux density at electrodes	W·m^{-2}
Q_{ei}	Electron-ion elastic collision cross section	m^2
Q_{eh}	Energy exchange between electrons and heavy species	W·m^{-3}
Q_{ij}	Ion-ion elastic collision cross section	m^2
$Q_{i,n}$	Internal partition function of heavy species i	—
Q_r	Volumetric radiation heat flux	W·m^{-3}
R	Optical depth	m
s	Sheath thickness	m
T_e	Electron temperature	K
T_h	Heavy species temperature	K
T_w	Electrode surface temperature	K
$\vec{u}$	Plasma flow velocity	m·s^{-1}
u_B	Bohm velocity	m·s^{-1}
$\overrightarrow{u_e}$	Electron flow velocity	m·s^{-1}
U_a	Anode sheath voltage drop	V
U_d	Cathode sheath voltage drop	V
V_B	Breakdown voltage of Paschen's Law	V
z	Charge number	—
z_{eff}	Effective charge number	—
z_{eff}^2	Effective squared charge number	—
α	Band-averaged absorption coefficient	m^{-1}
δ_{ie}	Inelastic collision factor	—
ε_A	Net emission coefficient	W· m^{-3} ·sr^{-1}
ε_0	Vacuum permittivity, ε_0 = 8.5542× 10^{-12}	A^2·s^4·kg^{-1}·m^{-3}
ϵ	Thermal emissivity	—
ϕ_a	Work function of anode material	J
ϕ_c	Work function of cathode material	J
$\nabla\phi$	Decrease of work function by Schottky effect	J
γ_{se}	Secondary electron emission coefficient	—
η_s	Computing speedup factor of Amdahl's law	—
φ	Electric potential	V
λ_D	Debye length	m
λ_h	Thermal conductivity of heavy species	W· m^{-1} ·K^{-1}
λ_e	Thermal conductivity of electrons	W· m^{-1} ·K^{-1}
λ_s	Thermal conductivity of electrodes	W· m^{-1} ·K^{-1}

μ	Dynamic viscosity	kg· m^{-1} ·s^{-1}
μ_m	Magnetic permeability of material, for vacuum μ_m=4$\pi \times 10^{-7}$	H·m^{-1}
ν_{ee}	Elastic collision frequency of electron-electron	s^{-1}
ν_{ei}	Elastic collision frequency of electron-heavy species i	s^{-1}
ν_{ie}	Elastic collision frequency of heavy species i-electron	s^{-1}
ν_{ij}	Elastic collision frequency of heavy species i-j	s^{-1}
ω	Turbulence frequency	s^{-1}
θ	Degree of thermal nonequilibrium, θ=T_e/T_h	—
ϑ	Swirl angle of injection	rad
ρ	Plasma flow density	kg·m^{-3}
ρ_s	Metal electrode density	kg·m^{-3}
σ	Electrical conductivity of plasma	S·m^{-1}
σ_s	Electrical conductivity of metal electrodes	S·m^{-1}
σ_{eff}	Effective electrical conductivity of sheath	S·m^{-1}
σ_{sh}	Electrical conductivity of Child's sheath	S·m^{-1}
σ_{ST}	Stefan-Boltzmann constant, σ_{ST}= 5.67$\times 10^{-8}$	W·m^{-2}·K^{-4}

Chapter 1

Introduction

1.1 Background

1.1.1 LTE and NLTE plasmas

The plasma state is frequently referred to as the fourth state of matter apart from the common states of solids, liquids and ordinary gases which we can well perceive from our daily lives. This state of matter has been justified by the fact that more than 99% of the known universe is in the plasma state. For example, the sun, whose interior temperature exceed 10^7K, is a huge plasma ball. The term "plasma" which will be frequently addressed in the following sections of this thesis is restricted to gaseous plasma, which means it consists of electrons, ions and neutral particles. Because the mass of ions and neutral particles is always much heavier than that of electrons (for example, argon atom mass is 6.6×10^{-26}kg, which is almost 10^5 times heavier than electron), these two kinds of particles are called heavy species. If a plasma is located in a closed system, each process is in equilibrium with its reverse process and the plasma is in thermodynamic equilibrium (TE) state. Such a plasma can be characterized with the extremely high temperature, pressure, and number densities of each single species. However, in a real plasma, deviations from equilibrium often occur. For example, radiation escapes out of the plasma, disturbing the detailed balance. If in such situation, the plasma temperature is still so high that the energy loss due to radiation can be neglected, the plasma can be considered as in a Local Thermodynamic Equilibrium(LTE). Such LTE state often occurs inside the plasma core, where collision process dominates. With LTE state, the characteristic time of the slowest reaction in plasma is negligible compared to that of convection and diffusion along temperature and composition gradients. If the temperature of heavy species is much lower than the electron temperature, in such situation (for example in the plasma-electrode interaction region, the plasma heavy species temperature approaches electrode surface temperature due to energy exchange with electrode surface while electron temperature remains much higher for conducting electric current), the plasma is in a thermal nonequilibrium state and cannot be described by a unified temperature. For this case, a more elaborate approach is necessary to describe the Non-Local Thermodynamic Equilibrium (NLTE) plasma along with drift-diffusion calculation of plasma composition. As the plasma-electrode interaction region is intensively researched and simulated in this scope, to avoid unrealistic assumption of local parameters in the plasma fringes, LTE plasma model is abandoned and only NLTE description is applied for the coupled simulation of plasma-electrode interaction.

1.1.2 Stages of electrical discharge

An electrical discharge results from the creation of a conducting path between two points of different electric potential in the medium in which the points are immersed. Usually, the medium is gas, such as air, argon, helium etc. If two points are separated by a vacuum, there's usually no discharge if cathode material is refractory. Although arc and glow discharges are the two most typical regimes or stages for researchers, they cannot fully describe the whole process for this highly complicated physical phenomenon. From the very first stage till a stable arc discharge there are typically three main stages with many important substages.

(1). Townsend discharge

After the initiation of ionization by cosmic rays or other sources of ionization radiation which will produce current of only femtoamperes, this stage, also called Townsend avalanche, is a starting state for massive electron production. It is usually initiated by a high-voltage source to form a stark electric field. The electric field and the mean free path of the electron must allow free electrons to acquire an energy level that can cause impact ionization. In this stage, Townsend believed that it is the electrons from cathode surface due to impact of positive ions that sustain the appearance of enough electrons for discharge initiation. This is called secondary emission mechanism which will be taken into account in later sections. If electron energy gained from electric field is not high enough, ionization will not happen. If in dilute gas, where mean free path for electrons is long, it is possible that most of the electrons reach anode before colliding with any atom or molecules. On the contrary, if the mean free path of electrons is too short, due to the too frequent colliding with atoms, electrons will have little chance gaining enough energy for ionization. Hence the condition for Townsend avalanche is not easy to achieve especially for high and low discharge pressures. When an electron with sufficient velocity causes impact ionization successfully, it will liberate another free electron. These two electrons then cause further electrons provided that they gain sufficient energy from electric field. Therefore step by step, a chain reaction comes into play which justifies its name avalanche.

(2) Glow discharge

While the process has already started with the discharge regimes mentioned above, they are not visible to eyes except for Corona regime [1], as a result, they are sometimes called dark discharge. When the applied voltage between two electrodes exceeds the striking voltage or breakdown voltage V_B, the gas in the tube ionizes, becoming a plasma. And electric current flow through it, making it visible and glow with a certain color according to the gas used. Such regime is called glow discharge. Friedrich Paschen discovered in 1889 that the striking voltage between two electrodes in a gas is related to the gas pressure and gap length [2], the Paschen's law is as follows:

$$V_B=\frac{Bpd}{\ln(Apd)-\ln[\ln\left(1+\frac{1}{\gamma_{se}}\right)]}, \tag{1.1}$$

where p is gas pressure in Pascals, d is the gap distance in meters, γ_{se} is the secondary electron emission coefficient. A and B are determined experimentally and found to be roughly constant over a certain $\frac{E}{p}$ range. By setting $\frac{\partial V_B}{\partial(pd)}$ = 0, it leads to a minimum breakdown voltage V_{Bmin} for a certain pd value:

$$(pd)_{min}=\frac{2.718}{A}\ln(1+\frac{1}{\gamma_{se}}), \tag{1.2}$$

$$V_{Bmin}=2.718\frac{B}{A}\ln(1+\frac{1}{\gamma_{se}}). \tag{1.3}$$

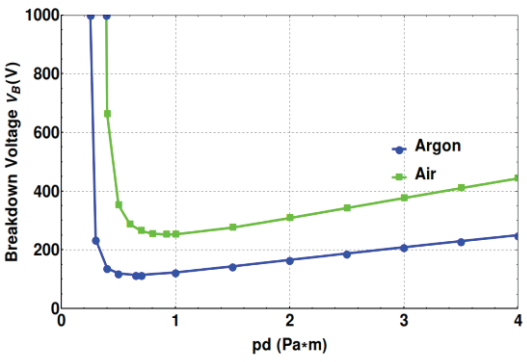

Fig.1.1. Paschen's curve for Argon and Air (coefficients taken from [3])

From Paschen's curve (Fig.1.1) it can be found that in case of a too low or too high *pd* value, V_{Bmin} becomes very high. It results from Townsend avalanche discussed above, which has a strict precondition for electric field strength and electron mean free path. When the voltage is increased above the normal glow range, abnormal glow begins.

(3) Arc discharge

If the applied voltage continues to increase and the cathode glow covers the entire cathode, then arc discharge begins. Arc discharge, which occurs in the ampere range of the current, is within the research scope of this study as most discharge applications are related to this regime. Industrially, electric arcs are used for welding, plasma cutting, electrical discharge machining. In astronautic fields, arc discharge inside an Arcjet thruster heats the gas propellant to produce huge thrust as an alternative way of traditional thrust by chemical fuel. It is characterized by a stark voltage drop from glow discharge with increasing current intensity. If the cathode voltage drop in a glow discharge is approximately of the order of 100V or more, in an arc discharge it is only 10~15V [4]. The voltage drop results from the increase of the electrical conductivity of a gas in the transition process to a plasma state so there is less and less resistivity for the current to flow though. If the intensity of current discharges continues to increase, the increase of the number of electron impacts give rise to the temperature increase of the gas in the vicinity of cathode and, thermal ionization starts to play the main role in ionization of the gas. Consequently, it is necessary to ensure a large electric potential drop in the vicinity of cathode in order to maintain quasi-neutrality in the main body of plasma. This region, characterized by a drastic electron rejection is defined as sheath region and will be discussed in later sections. The exit of the electron from the cathode surface take place now mainly due to thermionic and field emission instead of secondary emission, which is active in earlier stages.

1.1.3 Fluid description of a plasma

In arc discharge devices, such as Arcjet Thruster or Plasma Torch, the charge particles undergo a large number of collisions with each other. It is impractical to analyze the motion of each particle to obtain a macroscopic picture of plasma processes that is useful for evaluating the device life or performance. Fortunately, in most cases it is not necessary to track individual particles to understand the plasma dynamics. In statistics, the Maxwell–Boltzmann distribution is a particular probability distribution named after James Clerk Maxwell and Ludwig Boltzmann. It is used in physics (in particular in statistical mechanics) for describing particle speeds in idealized gases where the particles move freely inside a stationary container without interacting with one another, except for very brief collisions in which they exchange energy and momentum with each other or with their thermal environment. Therefore, it can be safely assumed that in collision-dominated, high-temperature plasma the velocities of each species will follow Maxwellian distribution (except for near-electrode regions), thus random motions can be calculated by making integrations of distribution functions.

The form of the Maxwell velocity probability density in three dimensions is:

$$f(\vec{u}\,,\vec{v}\,,\vec{w}\,)=\left(\frac{m}{2\pi k_B T}\right)^{3/2}\exp\left[-\frac{m}{2k_B T}(\vec{u}^2+v^2+\vec{w}^2)\right], \tag{1.4}$$

where $\vec{u}$, $\vec{v}$, $\vec{w}$ represent the velocity components in the three coordinate axes. k_B is the Boltzmann constant. The average kinetic energy of a particle in the Maxwellian distribution in three dimensions can be calculated using the following integration:

$$\bar{E}=\frac{\iiint_{-\infty}^{\infty}\frac{1}{2}m(\vec{u}^2+v^2+\vec{w}^2)f(\vec{u}\,,\vec{v}\,,\vec{w}\,)\mathrm{d}\vec{u}d\vec{v}d\vec{w}}{\iiint_{-\infty}^{\infty}f(\vec{u}\,,\vec{v}\,,\vec{w}\,)\mathrm{d}\vec{u}d\vec{v}d\vec{w}}, \tag{1.5}$$

By inserting Eq.1.4 into Eq.1.5, the averaged translation energy per particle in three-dimensional situation is:

$$\bar{E} = \frac{3}{2} k_B \mathrm{T}. \tag{1.6}$$

Therefore, for monatomic gas for example Argon which has three degrees of freedom, the averaged enthalpy neglecting internal excitation and reactive energy is:

$$\bar{H} = \bar{E} + \frac{p}{\rho} = \frac{5}{3}\bar{E} = \frac{5}{2} k_B T. \tag{1.7}$$

The averaged absolute velocity of a particle in the Maxwellian distribution is:

$$\overline{|u|} = \int_0^\infty |u| \left(\frac{m}{2\pi k_B T}\right)^{3/2} \exp\left(-\frac{m}{2k_B T}|u|^2\right) 4\pi |u|^2 \mathrm{d}|u| = \sqrt{\frac{8k_B T}{\pi m}}, \tag{1.8}$$

We know that plasma consists of multiple components with different number, mass and charges, the collision situation among them becomes very important as the method we choose to simulate plasma depends directly on it. There are generally two methods in simulating plasmas, namely continuum method (CFD) and microscopic method "particle-in-cell" (PIC). The latter is universally applicable since it takes into account almost all complex phenomena using combined Eulerian-Lagrangian method. However, it is computationally too expensive despite the progressive technology. Besides, the coupling of bulk plasma with sheath and metal electrode using this kind of method will be difficult. Therefore, this method is not applied in this dissertation. For conventional fluid description of plasma, there's strong limitation in relation to plasma Knudsen number and will lose validity in dilute gases. In terms of fluid dynamics, the fluid approximation is valid only when Knudsen number K_n is less than 0.01[5]:

$$K_n = \frac{1}{L_c n_j Q_{ij}} < 0.01, \tag{1.9}$$

where L_c is the characteristic length of plasma, for example the diameter of the tubular anode in a commercial plasma torch. n_j , Q_{ij} are number density and collision cross section respectively. For typical atmospheric LTE state of an argon plasma, n_e is within the order of $10^{23}/m^3$, Q_{ie} about the order of $10^{-16}\ m^2$, L_c always between 10^{-2} and 10^{-3} m, so K_n is $\ll 0.01$. The choice of using a continuum CFD method to simulate atmospheric argon plasma core in this study can thus be justified, whereas for plasma fringes or sheath regions, where number density and collision frequencies drastically decrease, this method may not be accurate enough. For a self-consistent modeling of plasma-electrode interaction, sheath region can be very important and thus needs treatment with care.

1.1.4 D.C. plasma torches

The application of thermal plasma technology has experienced a gradual transition stage from space-oriented activities in 1960s to a more and more material-oriented focus since 1980s as the mechanism of particulate interaction and the chemistry in thermal plasmas became well understood. Today, thermal plasma technology covers a wide range of applications. Among them plasma spraying has become a well-established and widely used technology with applications ranging from corrosion, coatings to the production of metallic and ceramic parts. The Direct Current (D.C.) arc plasma torches are one of the most typical devices used with this technology. D.C. plasma torches can work under common atmospheric pressure, low pressures, controlled ambient conditions or even under water. No matter under which conditions, the design of plasma spray torches for various plasma spray processes is essentially the same: a stick-type cathode (usually thermionic), a nozzle-shaped cathode and the plasma-forming gas injection stage (usually used for a swirl injection). The temperature that a gas

attained from arc discharge process in a plasma torch ranges from 10^4~5×10^4K and the velocity from 10~10^4m/s [6].

Arc plasma torches can be classified by two different categories. In the first situation, if the anode that's grounded inside torch body, so the arc created is inside the torch itself, it is called non-transferred plasma torch. On the contrary, if the grounded anode is outside (usually is the conductive material to be treated), in such condition the arc length is much longer than the non-transferred situation and it is called transferred plasma torch. Both of them has its advantages. For example, a benefit of transferred plasma torches is that the plasma arc is formed outside the water-cooled body, avoiding heat loss, which will otherwise lower the thermal efficiency. For non-transferred situation, the cutting object is outside the electrical circuit, this allows the plasma processing of not only the conducting materials but also the non-conducting ones which is a huge advantage over the transferred one. Due to its practicality, the non-transferred D.C. plasma torch is chosen to be researched and numerically simulated in this study. Another way of defining a plasma torch is to distinguish the way an arc set its root on an anode. If the arc sets foot freely onto the anode according to the interaction of gas dynamic and induced magnetic force and changes its position with time, it is called plasma torch with self-setting arc length [4]. Because of their simple design, thermal plasma torches with self-setting arc length are used widely. However, such kind of torch configuration always suffers from high level of fluctuations of arc voltage and the drooping of volt-ampere characteristic creates certain difficulties in matching of the arc with electric power sources. Those shortcomings may be eliminated by fixing the mean arc length in a specific range of variation of current density. A typical way to achieve that is to expand the diameter of the nozzle at the end of cylindrical anode suddenly. This produces a ledge that fixes the arc attachment. Another way of introducing a fixed anode attachment is to insert a neutral insulator between cathode and tubular anode and then divide anode into multiple (usually 3) segmented parts which are insulated to each other. Such device, sometimes called *DeltaGun* [7], creates multiple fixed arc roots and is in favor of damping arc instabilities and allowing uniform particle treatment. The numerical simulation in this study will also address it and the results are presented in section 5.3.

1.1.5 Design considerations

As for the design of a plasma torch, there're always two main questions that need to be considered in detail: how can a plasma torch work longer and how can it work more efficiently. However, for plasma torch design these two goals often contradicts each other.

The equivalent question for the former is how to reduce electrode erosion. We know that for a common commercial plasma torch, a non-refractory electrode is always chosen, for example tungsten or thoriated tungsten, whose melting point is over 3600K. Choosing suitable current intensities can avoid cathode erosion effectively. However, for anode material the candidates are always copper or steel, which will melt between 1300 ~1500K. The erosion of anode is always a research focus in order to increase the device lifetime. The anode erosion results from the strong heat flux of the constricted arc attachment between arc column and anode surface. However, anode attachment is always hard to predict because it moves from time to time as a result of interaction between magnetic body force and gas dynamic drag force [8]. Experiment [9] showed that an increase in residence time of anode attachment resulted in accelerated erosion. That means, to avoid anode erosion, measures should be taken to make arc roots move more frequently around anode surface than usual to reduce heat load at a certain spot, which always results in a more unstable arc.

However, to make plasma torch work more efficiently, for example, for better control of coating architectures, plasma treatments of liquids or nano-sized solid particles require a stable high

temperature arc region. This situation is always hard to achieve because of arc instability. According to the definitions from Duan et al. [10], the arc instability is divided to four modes based on two factors:

$$S=\frac{t_{up}}{t_{down}}, \tag{1.10}$$

$$A=\frac{\Delta V}{V}\times 100\%, \tag{1.11}$$

where t_{up} and t_{down} are the time duration of voltage rise and drop, ΔV is the amplitude of arc voltage fluctuation, V is the mean arc voltage.

(1). Steady mode (A $< 2\%$)

To archive this mode, the gas dynamic drag force should be balanced by magnetic body force. Because of its negligible arc jet fluctuation, the voltage fluctuation is also negligible, and the anode attachment is almost fixed. The anode erosion is thus severe, and the lifetime is always very poor.

(2). Takeover mode (A$\geq 10\%$ and S$<$1.1)

This mode occurs mostly with monatomic gases, the relatively small amplitude of the arc voltage fluctuation indicates a small movement of the arc attachment in axial direction. The previous attachment will not disappear immediately when new attachment builds at other places. The time for voltage drop and rise is almost the same. This is a most desirable work mode. Because too stable an arc will result in considerable erosion while too unstable will affect plasma spray efficiency as discussed previously.

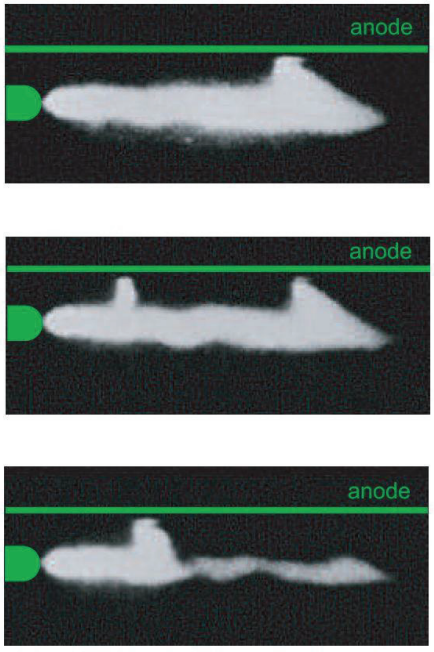

Fig. 1.2. Experimental high-speed images of arc reattachment process from Wutzke [11]

(3). Restrike mode (A$\geq 10\%$ ans S$\geq$5)

This mode occurs mostly with diatomic gases. It is characterized by strong voltage fluctuations. The difficulty in predicting this mode numerically is mainly due to a so-called “reattachment” process, which has been experimentally observed by Wutzke [11] shown in Fig.1.2. This microscopic process happens only within the cold boundary layer between arc core and anode surface. The real mechanism

for this process is still not clear. One physical explanation for it is the “micro-breakdown” theory [12]. In this case, the gasdynamic force dominates over magnetic body force. The cold gas that surrounds the arc core in the boundary layer pushes the current path further downstream when voltage rises and suddenly somewhere upstream exceeds the critical electric field strength and a new breakdown happens, forcing the previous attachment disappear and voltage curve drops down quickly. Other possible reasons responsible for a restrike mode may be the application of external magnetic field or the acoustic resonance by the compressibility effects of plasma in cathode cavity [13].

(4). Mixed Mode

Under different mass flow rates and total currents, the different work modes can take place simultaneously to form a mixed mode. Another two modes are namely restrike-takeover mixing mode ($A \geq 10\%$ and S<5) and takeover-steady mixing mode (2%<A<10%).

To find a compromise between two contradictory design goals there are usually several strategies, one common way is to simply increase working current to form an arc column with larger radius, the arc jet is thus wall-stabilized, the attachment region on anode surface is large enough to avoid erosion. However, this requires more input electric energy. Another way is to apply vortex injection at gas inlet, it contributes to the cooling of anode surface through intensified convective heat transfer by introducing cold rotating secondary gas around arc core and making it stable along the symmetry axis. If needed, a so-called magnetic-stabilization can also be applied. It is achieved by rotating a permanent magnet or adding a solenoid outside flow field, due to the Lorentz force, the “bridge” between arc core and anode surface will rotate circumferentially making the attachment move with a relative high frequency to avoid erosion. However, such configuration will add complexity to structure and operation. The effect of such design considerations will be numerically studied and discussed in section 5.3.

1.2 Research background and motivation

For a reliable modelling of the whole D.C. plasma torch system one needs to have a comprehensive knowledge regarding all its participants. The main part of the plasma torch is the electric arc between the electrodes. For fluid approximation, such part is simulated through the combination of conventional Navier-Stokes equations with Maxwell electromagnetic equations. For the simulation inside metal electrodes, this is even simpler as the complexity of solid transport equations are greatly reduced compared with LTE or NLTE arc models. The most complicated part of a self-consistent simulation is bound to be in its interaction region. Because there’s a black-box region between electrodes and main arc plasma called sheath region, which determines the energy transfer between the other two regions but exhibits a rather different physical process which even the most novel simulation methods developed for plasma core cannot solve it.

For common CFD simulation of arc plasma, metal electrodes are not considered due to the complexity of cathode layers (sheath, pre-sheath). Usually, the electron thermal and field emissions or temperature at electrode surface are represented by a set of imposed current density and temperature boundary conditions according to experimental measurements [14] or empirical arc spot radius according to the theory of [15]. However, these methods are all over-simplified and cannot reflect the arc-electrode interaction precisely. The necessity of building a self-consistent model of plasma-electrode system mainly results from the need of a reliable prediction of electrode temperature. For example, for plasma processing of minerals, one needs to know the current for the onset of melting for different electrode and current configurations in order to avoid or reduce electrode erosion in advance more effectively. On the contrary, to improve productivity, for arc welding applications such as GMAW (Gas Metal Arc Welding), knowing electrode temperature in advance can also maximize

melting [16]. A lot of work has been done by researchers through extensive theoretical and experimental study of arc-electrode interactions since properties of electric arcs depend not only on the arc plasma medium, but also on the bulk electrodes and the related electrode layers. When it comes to theoretical researches, Hsu et al. [17] developed an iteration method that calculates the electron number density inside sheath according to Boltzmann relation while the pre-sheath region according to Saha equation. The electric potential inside sheath is attained strictly from Poisson equation. The criterion dividing the two regions is the variation of electron number density over one electron mean free path. Zhou et al. [18] improved that model and included the bulk cathode into it. The cathode thermal conduction takes part in the whole iteration loop to yield cathode temperature and sheath potential drop with an auxiliary condition that the Steenbeck's minimum principle should be fulfilled. However, Benilov et al. [19] have found out later that Steenbeck's principle is not a corollary of mathematical models of gas discharges and it contradicts the mathematical models. Cayla [20] described a 1-D self-consistent model of interaction between an electric arc and a solid refractory cathode where current density conservation, balance of energy at sheath/pre-sheath interface and at the sheath-cathode interface are considered, whose calculated values of cathode sheath voltage drop and the power flux transmitted to the cathode are in good agreement with related literature. Gonzalez [21] used the same interaction model but included a two-temperature electrical conductivity inside sheath while assuming LTE in the plasma column, who drew the conclusion that the length of the ionization layer(pre-sheath) and the value of the secondary emission coefficient have significant influences on the whole interaction process. Among experimental researches, Haidar at al. [22] made an experimental study of the relationship between plasma temperature and cathode geometry with different cone angles. The measurements highlight a strong dependence of the plasma temperature on the cathode angles, because the cathode surface area attached by plasma is directly related to the cathode angle, where the most thermionic electrons are produced and in turn decide the heating area of plasma. This finding manifest again the importance of a fully coupled arc-electrode simulation.

Among the early numerical investigations, Zhu et al. [23] may be the first to have put forward a universally applicable theory and simulation method of the interaction between burning arcs and their electrodes. The simplified theory is applied in a two-dimensional simulation of arc-electrodes interaction which is combined with a one-dimensional sheath model. The sheath electron number density is calculated by an electron continuity equation considering the ambipolar diffusion and ionization nonequilibrium. A generalized Ohm's Law is used to describe the smooth transition from the hot, fully ionized arc spot to the cold sheath layer. The same simulation method was then used in the paper of Lowke et al. [24,25], which has achieved good experimental agreement. However, except for the fact that this model did not include space-charge effect, the most manifest disadvantage of this method is that, it is a grid-sensitive method. The interface boundary cells which located in the cathode spot should be greatly stretched until it reaches the LTE arc core as a unified temperature is assumed and number density derived from one-temperature model near cathode can be easily underestimated. This method is for the usual CFD simulation inapplicable because the over-stretched mesh cells will add to the degree of mesh non-orthogonality and give rise to much higher numerical instability and uncertainty. Maruzewski et.al. [26] used almost the same model from Zhu and divided the fluid region into hot arc plasma and cold SF_6 gas according to an empirical temperature value. However, this critical value that forces current flow through a predefined area will produce great temperature gradient in- and outside cathode and cannot reflect the interaction process properly. Recently, more and more sophisticated methods addressing this research area begin to appear. Shirvan [27] developed a self-consistent interaction model which utilizes the energy balance in the ionization layer to yield parameters that decide the specific coupled boundary condition at cathode surface. The author attributed the non-uniform electron emission at cathode surface to the diffusion or redistribution of rare earth activators. This model, although self-consistent as the author claimed, still requires cut-off

parameters such as critical current density and melting point of ThO_2 to make results more realistic. However, there're many circumstances in which the cathode surface temperature cannot reach melting point due to the low current intensity or material work functions. More sophisticated model such as Baeva's [28] fully nonequilibrium approach (thermal and chemical) makes it possible to link plasma model to sheath directly without the necessity to account for pre-sheath layer additionally. Despite its novelty in diffusion representation and boundary conditions for sheath, it accounts for only the singly ionized plasma, which may not be accurate at elevated plasma temperatures. As for anode layers, Nemchinsky et al. [29] divided it into three different zones: the outmost layer which is significantly influenced by plasma bulk and is thermal nonequilibrium; the middle layer which is dominated by diffusion and is both thermal and chemical nonequilibrium; the innermost space-charge layer which is also with the thickness of several Debye length as the cathode sheath. However, the measurement of anode sheath potential fall itself is still a problem, according to [28], the major reason for it is the difficulty in defining a reference point for measurement, as a result, for similar conditions, experiments by different authors failed to agree with each other. In some papers, anode sheath fall is ignored by setting it to 0 [28] or manually enlarging the boundary grids to include diffusion-dominated regions [30] due to lack of reliable anode sheath models.

This research is motivated by the need of finding a universally applicable description of plasma-sheath-electrode system and help to predict working situations of electrodes under different arc discharge conditions precisely for a better control of production process. For conventional arc discharge simulations which utilize finite volume method, it is difficult to include the complicated plasma boundary layer. Because the sheath layer itself has an extremely small thickness (usually of 10^{-8}m), if one tends to further divide such region with enough resolutions for calculation, it would be meaningless since the respect ratio of sheath cells will be infinitely high, causing collapse of numerical stability. An acceptable way to do this is to manipulate the single layer of boundary cells at interfaces and make them capable of reflecting the sheath region in an averaged way to avoid large gradients of related parameters induced by space-charge effect within extreme small dimension that cause numerical instability and unphysical results. A detailed description of interaction model and solving procedures will be presented in section 2.5.4.

1.3 Preview of research focus and methods

As is mentioned previously, a predefined boundary condition at cathode surface concerned with current density and temperature distribution cannot reflect the electron emission from cathode and its interaction with plasma properly. According to classic separation of physical regions, the whole discharge system should be separated into anode - anode sheath - anode presheath- plasma - cathode presheath-cathode sheath - cathode regions, while cathode presheath can be further divided into ionization and Knudsen layer (Fig.1.3). Theoretically, the simulation should be able to start at any one of the regions with arbitrary initial values and connect each other by energy conservation and charge conservation. However, due to the limitation of fluid approximation, the detailed space-charge effect cannot be modelled precisely in connection with continuum regions. In this study, sheath layer at cathode is simplified so that a macroscopic estimation is attained that can be applied as an extra parameter into the Navier-Stokes equations to allow a unified description of plasma and sheath. One advantage of it is that the arc attachment at cathode can be simulated dynamically, or in other words, some unnecessary estimations such as cathode spot radius or cut-off parameters, which fixes unrealistic conduction region can be spared. Besides, several important boundary conditions for plasma-electrode interface concerned with temperature, electric potential, magnetic field that ensure continuity are discussed and applied. With the combination with NLTE plasma model a self-consistent model can be built. Several benchmark simulations will be presented to validate the model, which provide a reliable basis for the numerical study of plasma torch. For this chapter both a conventional

D.C. plasma torch and a new type *DeltaGun* are simulated, not in an effort to judge which is superior on the whole, but to evaluate the effect and practicability of specific design considerations taking into account the device lifetime and efficiency.

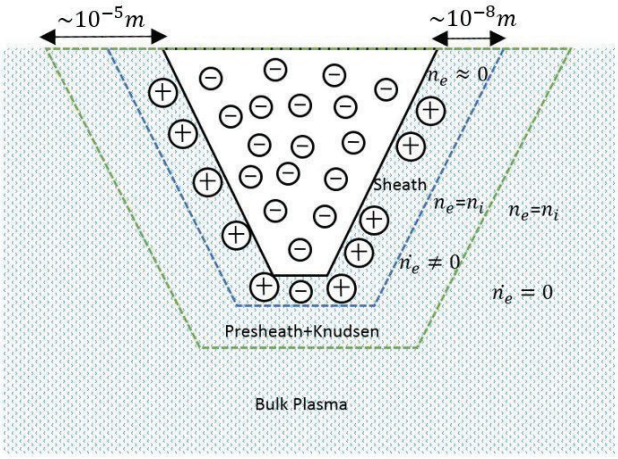

Fig. 1.3. Schematic description of cathode boundary layer

However, as the whole system needs to be simulated, considerable computation costs need to be reduced to an acceptable extent. Here Knudsen layer of cathode is ignored, which is replaced by Bohm's criterium into the interface boundary conditions. Anode sheath and presheath are also ignored as potential drop or rise is small in comparison to cathode layer. The thermal radiation cannot be simulated with its absorptivity within the whole range of wavelength due to the limitation of mathematical treatment, a band-averaged approximation within certain interval of wavelength and with certain optical depth can be considered as reasonable. The complicated calculation of nonequilibrium transport properties according to Chapman-Enskog theory is replaced by implementing the interpolation of accessible data from literature.

Thanks to the open source CFD simulation tool OpenFOAM, all the model considerations including transport equations, transport properties, radiation model and boundary conditions etc. can be implemented by C++ coding to help to carry out the numerical studies in this thesis. While OpenFOAM has already provided users with abundant example syntaxes covering a full range of basic CFD solvers aiming at different usage purposes, such as Electromagnetics, Buoyancy-driven flow, Multiphase flow and Particle-tracking problems, the standard solver which has been developed here is called *chtMultiRegionFoam*. It is meant to solve transient conjugate heat transfer between solid regions and compressible fluid region and handles secondary fluid or solid circuits which can be coupled thermally with the main fluid region. PISO algorithm is applied to correct and yield pressure and velocity fields. The detailed global coupling procedure including differencing schemes and iteration methods will be presented in following chapters.

Chapter 2

Mathematical descriptions of the interaction model

Before tackling the global interaction model that connects all the necessities of the discharge system, it is necessary to get all the primary physical processes described by mathematical equations in each region which are more or less simplified based on the requirement of precisions. As is introduced previously, this interaction model can be subdivided by several sub-regions that can only calculated by different set of transport equations or properties. As this set of transport equations is highly non-linear and differs from each other by its complexity, it is impossible to consider all the kinetic descriptions of plasma within the CFD simulations, therefore it is absolute necessary to reduce it to a computation affordable extent by reasonable assumptions and simplifications. As is suggested by many researchers [14,26] that the anode sheath plays no significant role due to its electrically conducting property caused by electron ambipolar diffusion and small magnitude of potential drop/rise, there's no need to apply extra anode sheath model. In this scope, only the plasma core, cathode sheath and metal electrodes are simulated explicitly according to their physical properties and interaction processes with each other.

2.1 The non-thermal plasma core

2.1.1 Plasma composition

Early models of the arc considered the arc mostly as a component in an electrical circuit and treated the arc properties empirically. This includes arcs in interruption devices. A more physical model based on energy conservation was derived by Heller [31] for the case of a one-dimensional steady state situation. The explosive growth of arc plasma applications since 1970s resulted in the development of modeling approaches of increased sophistication. Due to that experimental evidences [32,33] for departures from LTE in the cathode regions of a free burning arc are attained, the one-fluid, two-temperature method accounting for thermal nonequilibrium phenomena in the plasma is considered as suitable. On the assumption of Maxwell distribution described in 1.1.3, in this scope the Maxwellian distribution of particles with temperature T_e and T_h accordingly is assumed in electronic and heavy particles (neutral atoms and ions).

To get the plasma temperature distribution in the arc column, the first step is to calculate the particle number densities inside it. Generally, there are two ways to determine the particle number densities: chemical equilibrium and nonequilibrium models. The former utilizes the famous Saha–Langmuir equation, which relates the ionization state of a gas in thermal equilibrium to the temperature and pressure:

$$K_i = \frac{n_e n_i}{n_{i-1}} = \frac{2Q_{i,n}}{Q_{i-1,n}} \left(\frac{2\pi k_B m_e T_e}{h^2}\right)^{3/2} \exp\left(-\frac{E_i - \nabla E_i}{k_B T_e}\right), \tag{2.1}$$

where $Q_{i,n}$ is the internal partition function of heavy species i at the corresponding ionization level (i=0 for atom), whose temperature-dependent values are obtained from [34], ∇E_i is the lowering of ionization potential which is neglected in this scope.

However, due to the specific reaction time of different inelastic collisions, the state of ionization equilibrium is seldom achievable due to the local macroscopic velocity of plasma flow. For example, in a arcjet or MPD thruster, the plasma flow is usually accelerated to over 1000m/s due to thermal

expansion and magnetic pinch effect, the chemical process cannot catch up with the macroscopic translation of charged particles hence the real population deviates a lot from equilibrium results. Besides, in the near-electrode regions, due to the need to maintain quasi-neutrality of plasma core, the charged particles (ions and electrons) diffuse to the electrode surface with quite different velocities, and this so-called ambipolar diffusion has a dominant effect on the local particle population. As in this scope, electrodes are included into the computation model, the inclusion of diffusion transport is inevitable. According to the equilibrium results of plasma number density (Saha results) shown in Fig. 2.1, the number of Ar^{2+}exceeds that of Ar^{+}at over 26000 K so single ionization calculation is not adequate. The assumption of 3 level ionization still holds its validity at 35000 K, because at that temperature the ion number density of fourth level is still negligible. Hence plasma composition up to 3. ionization level (Ar^{+}, Ar^{2+}, Ar^{3+}) is considered in this scope to ensure a precise account of argon plasma composition at high temperatures:

$$Ar + e^{-} \rightleftharpoons Ar^{+} + 2e^{-} \tag{2.2a}$$

$$Ar^{+} + e^{-} \rightleftharpoons Ar^{2+} + 2e^{-} \tag{2.2b}$$

$$Ar^{2+} + e^{-} \rightleftharpoons Ar^{3+} + 2e^{-} \tag{2.2c}$$

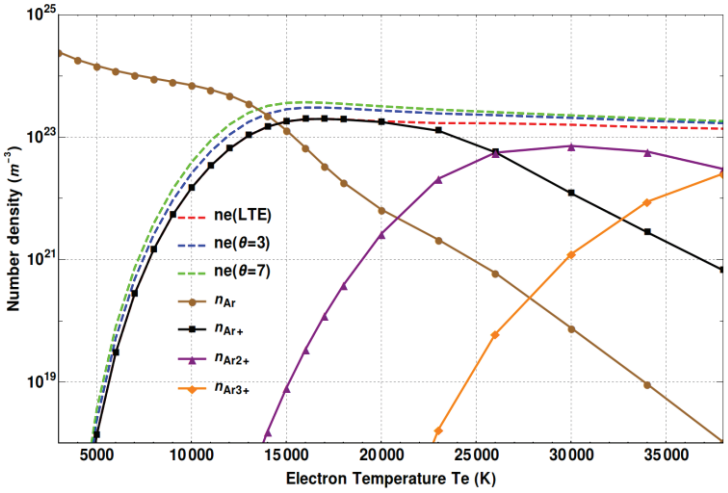

Fig. 2.1. Chemical equilibrium composition of triply ionized atmospheric argon plasma (electron results in 2T and heavy species in LTE)

The species conservation equations which account for ambipolar diffusion and ionization nonequilibrium give the following form:

$$\frac{\partial n_i}{\partial t} = -\nabla\cdot(n_i\vec{u}) - \nabla\cdot\vec{J}_{D,i} + \omega_i, \tag{2.3}$$

where i=0~3, $\vec{J}_{D,i}$ is the mass diffusion flux for heavy species:

$$\vec{J}_{D,i} = -n_s D_{fi}\nabla\left(\frac{n_i}{n_s+n_e}\right) - \xi_i\sum_{m=0}^{3}\left(-n_s D_{fm}\nabla\left(\frac{n_m}{n_s+n_e}\right)\right), \tag{2.4}$$

n_s is the total heavy species number density, ξ_i is the mass fraction of species i. The effective diffusion coefficient D_{fm} is approximated by the relation introduced in [35]. ω_i in Eq.2.3 is the source of net production/loss of heavy species i describing chemical nonequilibrium:

$$\omega_0 = -n_0 n_e k_{f,1} + n_1 n_e^2 k_{b,1}, \tag{2.5a}$$

$$\omega_i = -n_i n_e k_{f,i+1} + n_{i+1} n_e^2 k_{b,i+1} - n_i n_e^2 k_{b,i} + n_{i-1} n_e k_{f,i}, \text{ (i=1,2)} \tag{2.5b}$$

$$\omega_3 = -n_3 n_e^2 k_{b,3} + n_2 n_e k_{f,3}. \quad (2.5c)$$

where $k_{f,i}$ and $k_{b,i}$ are the for- and backward reaction rates. The Lotz [36] model for predicting the rate coefficients has the advantage to include all ground states on the assumption of a Maxwellian distribution of impacting electrons, which is particularly suitable in this scope as multi-ionization is considered. However, for electron production, the main mechanism for it is the collision by electron and excited atom and for electron loss the three-body recombination [37], which means the model of Lotz will underestimate this coefficient as only particles of ground state are considered. The Hoffert-Lien model [38] has been widely accepted due to its excellent agreement with experimental measurement. It considers the excitation to the first excited state for rate-controlling. In this scope, the Hoffert-Lien model is applied to calculate $k_{f,1}$ to account for first excited state, while other higher excited states are not considered in this scope:

$$k_{f,1} = 8S_1(2\pi m_e)^{-1/2}(k_B T_e)^{3/2}\left(\frac{E_1^*}{2k_B T_e} + 1\right)\exp\left(-\frac{E_1^*}{k_B T_e}\right), \quad (2.6)$$

where S_1 is the cross-section parameter, for argon it is $7\times 10^{-18}\mathrm{cm}^2/\mathrm{eV}$. E_1^* is the first excitation energy, which is 11.67eV for argon. For the rest of the ionization level, Lotz model is applied to account for only ground states:

$$k_{f,i} = 6.7\times 10^{-13}\left(\frac{e}{k_B T_e}\right)^{3/2}\sum_{i=1}^{3} a_i q_i\left[\frac{1}{A_i}\int_{A_i}^{\infty}\frac{e^{-x}}{x}dx - \frac{b_i e^{c_i}}{A_i + c_i}\int_{A_i+c_i}^{\infty}\frac{e^{-x}}{x}dx\right], \text{(i=2,3)} \quad (2.7)$$

where $A_i = \frac{P_i}{k_B T_e}$, P_i is the binding energy of electrons in i-th subshell of each ionization level. Other coefficients appear in Eq. 2.7 are constants taken from [35]. The calculated impact ionization rate based on these two models are presented in Fig.2.2.

As in case of equilibrium ionization, the net production rate ω_i=0, this leads to the approximation of three-body recombination rate coefficients $k_{b,i}$:

$$k_{b,i} = \frac{k_{f,i}}{K_i}. \quad (2.8)$$

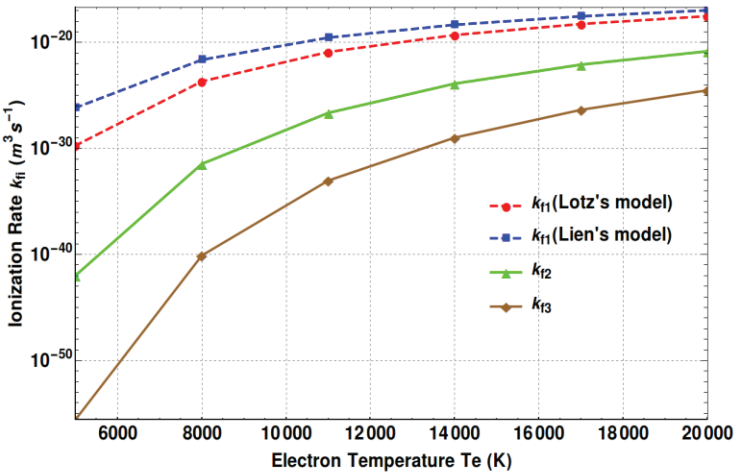

Fig. 2.2. Impact ionization rate of triply ionized argon plasma

Besides, all the particles in the plasma core must fulfill the requirement of quasi-neutrality:

$$\sum_{i=1}^{3} z * n_i = n_e, \quad (2.9)$$

as well as the Dalton's law of partial pressures:

$$(\sum_{i=0}^{3} n_i)k_B T_h + n_e k_B T_e = p, \tag{2.10}$$

where z is charge number, p is total pressure.

2.1.2 Transport equations

Apart from a reasonable estimation of plasma composition, the main factor that determines if the transport equations could calculate properly to reflect arc discharge is the full set of transport properties. However, the calculation of the transport properties related to inhomogeneous plasmas is quite complicated. It is therefore valuable to develop simple approximate methods that yield physical insight into basic mechanisms. It is necessary to get transport properties for arc discharge model such as thermal conductivities, electric conductivities, viscosities, inelastic collision cross sections and collision frequencies for heavy species and electron gases after determining the composition of two-temperature plasmas. However, as we cannot get the nonequilibrium composition beforehand, in most cases, transport properties are simplified based on results of equilibrium composition. The theory of transport properties of nonreactive gases is based on the Chapman-Enskog approximation theory of Boltzmann's equation. The Chapman-Enskog method is developed in the form of a series of Sonine polynomials, and is used to express, according to the chosen approximation order, the transport coefficients as determinants depending on collision integrals taking into account the interaction potential between two colliding species [39]. However, the high order of approximation causes large computational cost, especially when the degree of thermal nonequilibrium $\theta = \frac{T_e}{T_h}$ is taken into account. To reduce computation load, simple functions on the assumption of LTE for atmospheric argon plasma transport properties such as heavy species translational thermal conductivities λ_h, electron translational thermal conductivities λ_e and dynamic viscosity μ are taken from [40,41] ,which are used in the following chapters of arc discharge simulations, expect for the two-temperature electrical conductivities taken from [42] shown in Fig.2.3, which is a decisive transport property that will produce correct current path and joule heating and thus help to obtain a realistic voltage development.

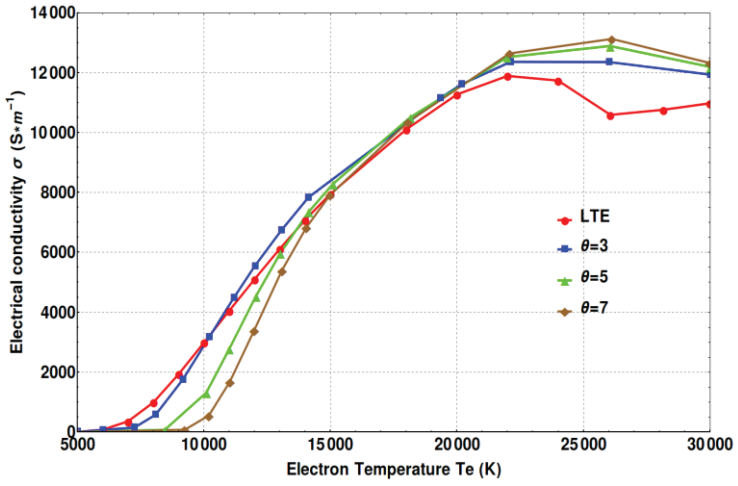

Fig. 2.3. Electrical conductivity of thermal nonequilibrium atmospheric argon plasma (with θ up to 7)

The energy-weighted average of momentum transfer collision cross sections of electron-positive charged ions Q_{ei} (i=1~3) and ion-ion Q_{ij} are approximated as :

$$Q_{ei} = \frac{\pi}{4}\left(\frac{z_i e^2}{4\pi\varepsilon_0 k T_e}\right)^2 \ln\left(1+\frac{144\pi^2(\varepsilon_0 k T_e)^3}{n_e e^6 z_{eff}^2 (z_{eff}+1)}\right), \tag{2.11a}$$

$$Q_{ij} = \frac{\pi}{4}\left(\frac{z_i z_j e^2}{4\pi\varepsilon_0 kT_h}\right)^2 \ln\left(1+\frac{144\pi^2(\varepsilon_0 kT_e)^3}{n_e e^6 z_{eff}^2(z_{eff}+1)}\right), \tag{2.11b}$$

where ε_0 is the permittivity of free space, the effective charge number z_{eff} ,z_{eff}^2 are expressed as:

$$z_{eff}=\frac{n_e}{\sum_{i=1}^{3} n_i}, \tag{2.12a}$$

$$z_{eff}^2= \frac{\sum_{i=1}^{3} i^2 n_i}{\sum_{i=1}^{3} n_i}. \tag{2.12b}$$

The electron-neutral collision cross section for argon Q_{e0} is approximated by $4.0\times 10^{-20} m^2$[40].

The collision frequencies of electron-electron, electron-ion and ion-ion/neutral atom ν_{ee}, ν_{ei}, ν_{ie},and ν_{ij} are calculated based on the hard sphere model:

$$\nu_{ee}=\sqrt{2} n_e Q_{ee}\sqrt{\frac{8k_B T_e}{\pi m_e}}, \tag{2.13}$$

$$\nu_{ei}=n_i Q_{ei}\sqrt{\frac{8k_B T_e}{\pi m_e}}, \tag{2.14}$$

$$\nu_{ie}=2 n_e Q_{ei}\sqrt{\frac{8k_B T_e}{\pi m_h}}\sqrt{\frac{m_e}{m_h}}, \tag{2.15}$$

$$\nu_{ij}=\sqrt{2} n_j Q_{ij}\sqrt{\frac{8k_B T_h}{\pi m_h}}. \tag{2.16}$$

With the above simplifications of transport properties, the transport equations based on the one-fluid, two-temperature, chemical nonequilibrium regime can be used to describe the transient atmospheric compressible plasma flow.

(1). The mass conservation equation

From Eq. 2.4 and 2.5 it is clear when all the heavy species (i=0-3) are added up together, the total mass diffusion flux $\sum \vec{J}_{D,i}$ and production source $\sum \omega_i$ will be 0, which meets the requirement of mass continuity automatically:

$$\frac{\partial \rho}{\partial t} + \nabla\cdot(\rho\vec{u})=0, \tag{2.17}$$

where plasma density $\rho= (\sum_{i=0}^{3} n_i)m_h$. The electron gas density $n_e m_e$ is very small compared with heavy species density, so it can be neglected.

(2). The momentum conservation equation

$$\frac{\partial \rho\vec{u}}{\partial t} + \nabla\cdot(\rho\vec{u}\,\vec{u}) = -\nabla p +\nabla\cdot\left(\mu(\nabla\vec{u}+(\nabla\overrightarrow{u})^T)-\frac{2}{3}\mu(\nabla\cdot\vec{u})\mathbf{I}\right)+\vec{J}\times\vec{B}, \tag{2.18}$$

where μ is the plasma heavy species dynamic viscosity, **I** is the identity tensor and the body force $\vec{J}\times\vec{B}$ is Lorentz force caused by electromagnetic induction.

(3). The enthalpy equation of heavy species

When discussing the exact form of two-temperature enthalpy equations, however, there's hardly consensus. Freton et al. [43] made a series of numerical tests concerning different forms of two-temperature equations. According to [43], the ionization term e_{io} in the total enthalpy should be allocated to electron equation. Besides, as we know that the internal energy term e_{in} takes the following form:

$$e_{in} = \sum \frac{n_i k_B T_e^2}{\rho} \frac{\partial ln Q_{in}}{\partial T_e}, \tag{2.19}$$

For electron, e_{in}=0 as Q_{in} equals to 2. Hence e_{in} should be allocated to heavy species equation. Based on the theory above, the heavy species enthalpy equations used in this study are shown as follows:

$$\frac{\partial(\rho h_h)}{\partial t} + \nabla\cdot(\rho h_h \vec{u}) = \nabla\cdot(\lambda_h \nabla T_h) + p_e \nabla\cdot\vec{u} + \frac{\partial p_h}{\partial t} + Q_{eh} + \vec{u}\cdot(\vec{j}\times\vec{B}), \tag{2.20}$$

where the specific enthalpy of heavy species $h_h = (2.5 n_s k_B T_h + e_{in})/(n_s m_h)$, Q_{eh} is the energy-exchange term between electrons and heavy species which is expressed as:

$$Q_{eh} = 3k_B \frac{m_e}{m_h} n_e \left(\sum_{i=1}^{3} \nu_{ei} + \nu_{ea}\right)(T_e - T_h)\delta_{ie}, \tag{2.21}$$

As $\sum \vec{J}_{D,i}$ is equal to zero, so there's no flux of enthalpy by diffusion in heavy species equation. This is consistent with the conclusion by [43] that for chemical equilibrium computation, the reactive thermal conductivity should be associated with electron equations. The term $p_e \nabla\cdot\vec{u}$ is the work done by electrons through electrostatic field onto the heavy species, δ_{ie} is the inelastic collision factor, for monatomic gas argon considered in this scope it equals 1. $\vec{u}\cdot(\vec{j}\times\vec{B})$ is the kinetic energy of heavy species gained from the induced magnetic field, which is also one part of the total joule heating term $\vec{j}\cdot\vec{E}$:

$$\vec{j}\cdot\vec{E} = \vec{u}\cdot(\vec{j}\times\vec{B}) + \frac{J^2}{\sigma} - \frac{1}{e n_e}\vec{j}\cdot\nabla p_e. \tag{2.22}$$

As the electron velocity is much larger than that of heavy species and thus more capable of conducting energy, it can be assumed that most of the joule heating (last two terms on R.H.S. of Eq.2.22) contributes solely to electron energy/enthalpy transport.

(4). The enthalpy equation of electron gas

Similar to enthalpy equation of heavy species, the enthalpy equation of electron gas can be written as:

$$\frac{\partial(\rho h_e)}{\partial t} - \nabla\cdot(\rho h_e \overrightarrow{u_e}) = \nabla\cdot(\lambda_e \nabla T_e) - Q_{eh} + \frac{J^2}{\sigma} - Q_r - p_e \nabla\cdot\vec{u} - \frac{1}{e n_e}\vec{j}\cdot\nabla p_e - \nabla\cdot(2.5 k_B T_e \vec{J}_{D,e}), \tag{2.23}$$

where $h_e = 2.5 n_e k_B T_e + e_{io}$, $e_{io} = \sum n_i E_i$, by allocating this term to electron enthalpy, the sink term due to inelastic collision $-\sum_{i=1}^{3} \omega_i * E_i$ can be offset. $\overrightarrow{u_e}$ is electron velocity, the mass diffusion flux for electron is $\vec{J}_{D,e} = \sum_{i=1}^{3} z\vec{J}_{D,i}$ in order to maintain quasi-neutrality condition and Q_r is volumetric radiation heat loss calculated according to a modified method based on Lowke's [44] net Emission model which will be discussed in section 2.1.3.

To reduce the number of unknown parameters, the electron velocity u_e can be replaced by heavy species velocity $\vec{u}$ with the following relation to current density $\vec{J}$:

$$\vec{J} = e n_e (\vec{u} - \overrightarrow{u_e}), \tag{2.24}$$

$$\overrightarrow{u_e} = \vec{u} - \frac{\vec{j}}{e n_e}. \tag{2.25}$$

Replacing $\overrightarrow{u_e}$ in Eq.2.23 by expression of Eq.2.25 and setting the divergence of current density $\nabla\cdot\vec{J}$ to zero due to charge conservation, the enthalpy equation of electron gas can be rearranged as:

$$\frac{\partial(\rho h_e)}{\partial t} + \nabla\cdot(\rho h_e \vec{u}) = \nabla\cdot(\lambda_e \nabla T_e) - Q_{eh} + \frac{J^2}{\sigma} - \frac{1}{e n_e}\vec{j}\cdot\nabla p_e - Q_r + 2.5\frac{k_B \vec{j}}{e}\nabla T_e$$
$$- p_e \nabla\cdot\vec{u} - \nabla\cdot(2.5 k_B T_e \vec{J}_{D,e}). \tag{2.26}$$

(5) Electromagnetic Field Equations

The electromagnetic problems inside the arcjet or plasma flow are solved by Maxwell's Equations. These are a set of partial differential equations that, together with the Lorentz force law, form the foundation of classical electromagnetism, classical optics, and electric circuits. These equations describe how electric and magnetic fields propagate, interact, and how they are influenced by objects.

When the plasma is moving with respect to the external magnetic field at the velocity $\vec{u}$, the total electric field applying Lorentz transformation is:

$$\vec{E}'=\vec{E}+\vec{u}\times\vec{B}-\frac{\vec{J}\times\vec{B}}{en_e}. \tag{2.27}$$

As the contribution of the Hall effects $\frac{\vec{J}\times\vec{B}}{en_e}$ is usually small if no intense external magnetic field is applied, it is not considered in this study. So the generalized Ohm's law in a conducting flow such as plasma can be written as:

$$\vec{J}=\sigma(\vec{E}+\vec{u}\times\vec{B}). \tag{2.28}$$

According to Gauss's law and quasi-neutrality assumption of a plasma:

$$\nabla\cdot\overrightarrow{E'}=0. \tag{2.29}$$

$$\nabla\cdot\vec{J}=0. \tag{2.30}$$

The Maxwell–Faraday equation is a generalization of Faraday's law that states that a time-varying magnetic field will always accompany a spatially-varying, non-conservative electric field, and vice versa. The Maxwell–Faraday equation is:

$$\nabla\times\vec{E}=-\frac{\partial\vec{B}}{\partial t}. \tag{2.31}$$

Ampère's law relates magnetic fields to electric currents that produce them, and the displacement current considered in Maxwell's corrected version is neglected here:

$$\nabla\times\vec{B}=\mu_m\vec{J}, \tag{2.32}$$

where μ_m is magnetic permeability of material, for argon plasma, it is equal to 1.237×10^{-6} H·m^{-1}.

Gauss's law for magnetism states that the magnetic field B has divergence equal to zero. In other words, that it is a solenoidal vector field. It is equivalent to the statement that magnetic monopoles do not exist:

$$\nabla\cdot\vec{B}=0. \tag{2.33}$$

The calculation of electric and magnetic fields using electric scalar potential φ and magnetic vector potential $\vec{A}$ has been an appropriate method modeling plasma electromagnetic properties. These potentials can be used to yield their associated fields as follows:

$$\vec{E}=-\nabla\varphi-\frac{\partial\vec{A}}{\partial t}. \tag{2.34}$$

$$\vec{B}=\nabla\times\vec{A}. \tag{2.35}$$

As the current density of cathode surface cannot be determined beforehand, the treatment of $\vec{B}$ at interface can be rather difficult whereas $\vec{A}$ at this place is always continuous regardless of emission

current (this will be discussed in section 2.5.5), hence the so-called $\vec{A}$-φ formulation is applied. Another major advantages of $\vec{A}$-φ formulation is that as in Eq.2.35, $\vec{B}$ is the rotation of field $\vec{A}$, and $\nabla \cdot (\nabla \times \vec{A}) \equiv 0$, so the solenoidal constraint of Eq.2.33 is fulfilled automatically. Besides, as $\nabla \times (\nabla(\varphi)) \equiv 0$, according to Eq. 2.34, $\nabla \times \vec{E} = -\frac{\partial}{\partial t}(\nabla \times \vec{A}) = -\frac{\partial \vec{B}}{\partial t}$, so Eq. 2.31 is also fulfilled. The total number of Maxwell's equations with this formulation can be reduced from 5 to 3. Substitute Eq.2.30 and Eq.2.32 by the relation expressed in Eq. 2.28, Eq. 2.34 and Eq.2.35, and by using the Coulomb Gauge $\nabla \cdot \vec{A} = 0$, supposing $\nabla \cdot \sigma$ is negligible in the whole gas region, the $\vec{A}$-φ formulation of Maxwell's equation can be expressed as follows:

$$\frac{\partial \vec{A}}{\partial t} + \nabla\varphi - \vec{u} \times (\nabla \times \vec{A}) - \frac{1}{\mu_m \sigma} \Delta \vec{A} = 0. \tag{2.36}$$

$$\nabla \cdot (\sigma \nabla\varphi - \sigma \vec{u} \times (\nabla \times \vec{A})) = 0. \tag{2.37}$$

2.1.3 The Net Emission radiation model

While the gases radiate in general very selectively at various frequencies or wavelengths, it is possible to have a radiative energy balance at the radiating frequency taking into account the emission and the absorption of the energy by gas. In most cases of D.C. or R.F. plasma torch jets, the temperature distribution along the jet radius at a distance z from the torch exit can be described by the following function:

$$\frac{T}{T_{max}} = (1 - \frac{r}{R})^n, \tag{2.38}$$

where T_{max} is the temperature at the axis of the jet (r=0), R is the jet radius at position z, using the diffusion approximation by Siegel and Howell [45] to calculate Eq.2.38 will be very complicated. Lowke [44] made this calculation simplified by the assumption of a isothermal cylinder. i.e., T= T_{max} for r<R and T=0 for r $\geq$ R. The fraction of total power radiated per unit volume and unit solid angle into a volume element surrounding the axis of a cylinder and escapes from the cylinder after crossing a Thickness (or it can be called optical depth) R of the isothermal plasma. He defined an approximate net emission coefficient ε_A obtained from calculations of net emission of radiation at the center of cylindrical isothermal plasmas of various temperatures and radius. The net emission coefficient at the center of an isothermal cylinder can be calculated through the integration throughout all the wavelengths:

$$\varepsilon_A = \int_0^\infty B_\lambda \, k_\lambda G_1(k_\lambda, R) d\lambda, \tag{2.39}$$

where G_1 is a function accounting for cylindrical geometry of the plasma. To further simplify this model, Liebermann et.al. [46] have demonstrated that the isothermal cylinder could be approximated by an isothermal sphere with a precision better than 90%:

$$\varepsilon_A = \int_0^\infty B_\lambda \, k_\lambda \exp(-k_\lambda R) \, d\lambda, \tag{2.40}$$

where k_λ is absorption coefficient, B_λ is the spectral radiance of a body proposed by Max Planck, which describes the amount of energy it gives off as radiation of different frequencies or wavelengths. It is given in the form of per unit wavelength by:

$$B_\lambda(\lambda, T) = \frac{2hc^2}{\lambda^5} \frac{1}{e^{\frac{hc}{\lambda k_B T}} - 1}. \tag{2.41}$$

R is cylindrical plasma column radius which is assumed 1mm in this scope. Thus, the total volumetric net radiation flux per unit time used in Eq. 2.26 can be calculated as:

$$Q_r = 4\pi\varepsilon_A. \tag{2.42}$$

The prediction of the approximated net emission coefficient above requires the knowledge of spectral coefficients of absorption k_λ as a function of radiation wavelength. Vitel et al. [47] studied experimentally the continuous absorption spectra of dense plasmas by measuring their optical thickness. The absorption coefficient is deduced knowing the radial profiles of particles and temperature. According to Vitel, the total spectral absorption coefficient k(λ, T) is described as a function of temperature T and wavelength λ combining the free-bound with free-free radiation effect:

$$\mathrm{k}(\lambda, T) = \mathrm{C}\lambda^3 \frac{n_e^2}{T^{1/2}} \exp\left(\frac{hc}{\lambda k_B T}\right)\xi(\lambda, \mathrm{T}), \tag{2.43}$$

$$\xi(\lambda, T) = \frac{g_0}{\Sigma_1}\left[1 - \exp\left(-\frac{hc}{\lambda k_B T}\right)\right]\xi^{fb}(\lambda, T) + \exp\left(-\frac{hc}{\lambda k_B T}\right)\xi^{ff}(\lambda, T), \tag{2.44}$$

where C=1.45× 10^{-27}, the factor ξ^{fb} has been introduced and calculated by Biberman et al [48] and is 1.5 on average for argon plasma according to the experimental measurements of [47]. The factor ξ^{ff} is practically constant, close to 1.2 [49].

However, in order to calculate the approximate net emission coefficient, the term $B_\lambda k_\lambda \exp(-k_\lambda R)$ in Eq.2.35 needs to be integrated at all wavelength scales. Clearly, that is not acceptable concerning computational cost. A multi-band approach was introduced by Dixon et.al. [50], who assumes that within each band the plasma acts similarly to a grey body, i.e. the plasma within a certain band range has an emissivity which is not dependent on wavelength but only on temperature. This is achieved by certain method to yield an average value in each band. Such an ideal body does not exist in practice, but the assumption is a good approximation for many objects used in engineering. Besides, Dixon et al. [50] made a comprehensive model comparison concerning the three radiation models, including the semi-empirical net emission model, 5-band P1 model and the method of partial characteristics. It is concluded that all three models give similar distributions of radiative heat loss. The net emission and P1 model give more accurate results when compared with experimental measurements, whereas the net emission model requires the lowest computational cost among others. Due to this advantage, this multi-band approach based on Lowke's net emission model is applied in this scope.

Following Dixon's multi-band approach, the spectrum is divided into five bands and an average absorption coefficient is calculated for each band, and the Planck function needs also to be integrated for each band (λ_1~λ_2, λ_2~λ_3, λ_3~λ_4, λ_4~λ_5, λ_5~λ_6):

$$\overline{k_N} = \frac{\int_{\lambda_n}^{\lambda_{n+1}} k_\lambda B_\lambda d\lambda}{B_N}, \tag{2.45}$$

$$B_N = \int_{\lambda_n}^{\lambda_{n+1}} B_\lambda \, d\lambda. \tag{2.46}$$

Following the band division of Dixon, the total spectrum ranging from 30nm to 3000nm is divided into five bands: 30nm to 72 nm, 72nm to 124 nm, 124nm to 181nm, 181nm to 1240nm, and 1240nm to 3000nm. Thus the five-band approximate net emission radiation model used here can be summarized as:

$$Q_r = 4\pi\left[\sum_{N=1}^{N=5} \overline{k_N}\, B_N \exp(-\overline{k_N} R)\right]. \tag{2.47}$$

To integrate the spectral radiance B_λ alone over a finite range, Widger et al. [51] introduced a practical method to yield B_N to avoid crude interpolation:

$$B_\sigma = \int_\sigma^\infty B(\sigma)\, d\sigma = \int_\sigma^\infty 2 \times 10^8 hc^2\, \sigma^3 \frac{1}{e^{\frac{100hc\sigma}{k_B T}} - 1} d\sigma$$

$$=\frac{2k_B^4T^4}{h^3c^2}\sum_{n=1}^{\infty}(\frac{x^3}{n}+\frac{3x^2}{n^2}+\frac{6x}{n^3}+\frac{6}{n^4})e^{-nx}\ , \tag{2.48}$$

where $\sigma=\frac{1}{\lambda}$ /cm is called wavenumber, x= $\frac{100hc\sigma}{k_BT}$. It is proved that to carry the above summation up to n=min(2+20/x,512) will provide convergence with accuracy to as many as 10 significant figures.

Thus B_N can be attained with the following relation:

$$B_N = \int_{\lambda_n}^{\lambda_{n+1}} B_\lambda \, d\lambda = \int_{\sigma_1}^{\sigma_2} B(\sigma)\, d\sigma = \int_{\sigma_1}^{\infty} B(\sigma)\, d\sigma - \int_{\sigma_2}^{\infty} B(\sigma)\, d\sigma = B_{\sigma_1} - B_{\sigma_2}. \tag{2.49}$$

Table 2.1. Integrated spectral radiance value in each band for selected temperatures

	Wavelength range(nm)	500K	5000K	15000K	25000K
B_1	30~72	0	4.9×10^{-7}	671436	2.73×10^{8}
B_2	72~124	0	1.99	4.21×10^{7}	1.8×10^{9}
B_3	124~181	0	1024.66	1.47×10^{8}	1.91×10^{9}
B_4	181~1240	2×10^{-4}	8.45×10^{6}	7.04×10^{8}	3×10^{9}
B_5	1240~3000	14.25	2.45×10^{6}	1.5×10^{7}	3×10^{7}

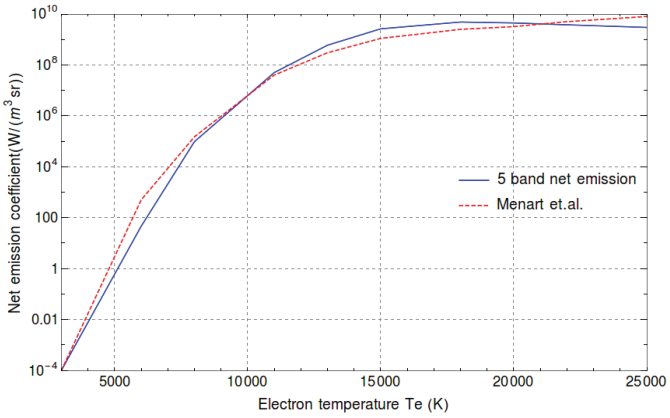

Fig.2.4. Comparison of calculated net emission coefficient of pure argon at R=1mm with the results from Menart et al.

Here the calculated net emission coefficient result is compared with that of Menart et al. [52] with the same plasma column radius at atmospheric pressure. The difference between both results can be possibly originated from the different expressions of the spectral absorption coefficient or the spectrum range taken into account.

2.2 The metal electrodes

The electrodes play an important role in discharge applications. Under different working conditions or for different purposes of usage, the anode is merely a passive collector of electrons unless its area attached by arc is small or the discharge current is high, in these conditions, anode spots or erosion may appear, which usually limits the device lifetime. On the contrary, the cathode is versatile and has a wide variety of different functionalities according to their specific properties and input parameters. As for the devices designed for daily use and long lifetime, such as gas-discharge lamps, the electrons emitted from cathode surface are not due to thermionic emission, but secondary emission or field emission, this is usually achieved by special treatment of cathode surface to reduce the work function. Due to the high discharge voltage (usually several hundred volt), the current between the two electrodes for given power are small, thus the cathode temperature rarely reaches melting point, so it can work for a long time. This kind of cathode is always called cold cathode. On the contrary, if the cathode is heated intensively by the current through it, that most of its emitted electrons are due to

thermionic emission, it is called hot cathode. Hot cathodes are often used in welding applications, for example in GTAW (Gas Tungsten Arc Welding) or Tungsten/Inert-Gas (TIG) welding, which is a manual welding process that uses a non-consumable electrode made of tungsten, an inert or semi-inert gas mixture, and a separate filler material. It is especially useful for welding thin materials and is characterized by a stable arc and high quality welds. If non-refractory materials serve as hot cathode, such as steels, the cathode is now expected to melt as much and as efficiently as possible, such application is called gas metal arc welding (GMAW), or more commonly called MIG (for Metal/Inert-Gas), which is a semi-automatic or automatic welding process with a continuously fed consumable wire acting as both electrode and filler metal, along with an inert or semi-inert shielding gas flowed around the wire to protect the weld site from contamination. Besides, if cathode works under vacuum or very low pressure, due to the dilute gas and large mean free path of molecules, the working gas cannot be ionized by common discharge conditions, or in other words, the plasma cannot be produced solely by gas particles, the hot cathode needs to be fed by high current to give rise to explosive or evaporative emission at cathode surface, and then the vaporized cathode material is ionized, joining the local plasma and providing high electrical conductivity to sustain the arc, which is usually called cathodic arc. If a reactive gas is introduced during the evaporation process, dissociation, ionization and excitation can occur during interaction with the ion flux and a compound film will be deposited. This kind of arc is often used to synthesize extremely hard film to protect the surface of cutting tools and extend their life significantly.

Despite of the diversity of cathode applications, in this study, a hot, refractory cathode with atmospheric arc is researched and simulated. An attempt to describe the electrode process could be started by addressing its general transport equations. Inside the electrodes, the temperature distribution is calculated through the three-dimensional transient thermal conduction equation in form of the solid enthalpy h_s with a heat source represented by the joule heating:

$$\frac{\partial(\rho_s h_s)}{\partial t} + \nabla \cdot (\frac{\lambda_s}{c_p}\nabla h_s) + \frac{j_s^2}{\sigma_s} = 0, \tag{2.50}$$

where the joule heating term $\frac{j_s^2}{\sigma_s}$ is caused by the transfer of kinetic energy of free electrons in the bulk metal to phonons.

By setting $\vec{u}$ =0, the $\vec{A}$ -φ formulation of Maxwell equations (see Eq.2.36 and 2.37) derived for solid region is attained:

$$\frac{\partial \vec{A}}{\partial t} + \nabla\varphi - \frac{1}{\mu_m \sigma_s}\Delta\vec{A} = 0. \tag{2.51}$$

$$\nabla \cdot (\sigma_s \nabla\varphi) = 0. \tag{2.52}$$

The calculated electrode potential results from Eq.2.52 will lead to the result of electrode current density by $\vec{J_s}$=- $\sigma_s\nabla\varphi$ for the calculation of joule heating term in Eq.2.50. The temperature-dependent electrical conductivity data of thoriated tungsten cathode σ_s are taken from [53]. The secondary phenomenon that accompany the discharge process including phase change, evaporation and erosions of solid materials are neglected here.

Apart from the energy transport and dissipation phenomena represented by Eq.2.50, the electrode surface temperatures are determined by the complicated interactions caused by energy fluxes associated with ion, atom and electron fluxes of different physical origins, as well as radiation process. The calculation of energy transport fluxes between plasma and both electrodes is indispensable because in this scope the electrode surface temperature is not imposed as a presumed boundary

condition but is the result of interaction model, these are discussed as follows with certain degree of simplification.

2.2.1 Heat flux on the plasma-anode interface

The energy transfer to the anode has been modelled and determined experimentally with a wide range of approaches [54,55]. Except for the heat transfer mechanisms due to temperature gradients and radiative transport, the energy transfer due to current flow must be considered. Considering a complex of that, the specific anode heat flux can be generally expressed as:

$$q_a=j_e\phi_a+q_{el}-\lambda_e\nabla T_e-\lambda_h\nabla T_h+j_i(E_a-\phi_a)+q_R, \tag{2.53}$$

where j_e is the electron current, ϕ_a the anode material work function, q_{el} the heat flux associated with electron flux into anode, j_i the ion current density, q_R the surface radiative heat flux from arc. The first term on the R.H.S. of Eq.2.53 is the energy released due to incorporation of electrons into the metal lattice. The third and fourth term is the conductive heat transfer term due to electron and heavy species from plasma. The fifth term represents the energy released when ions reach the anode surface and recombined with electrons. The electron enthalpy flux q_{el} can be defined as follows when a diffuse attachment and a positive anode fall U_a is assumed [56]:

$$q_{el}=j_e(2.5\frac{k_BT_e}{e}+U_a) \tag{2.54}$$

However, the positive anode fall has been proven unsatisfactory since 1980s. First of all, when anode fall is positive, all the electrons are accelerated toward anode, heating the anode though bombardment energy gained from acceleration. But with this assumption the electron current density due to the high thermal velocity is much higher than the actually observed current density and violates Kirchhoff's Law, so there must be a "slow down" process in front of anode to reject some electrons, this makes the electric potential at anode sheath a little higher than that of anode surface, namely a slight negative anode fall, which is usually about 1V. Compared with the cathode sheath voltage fall (usually over 10V), the anode sheath effect is negligible.

Dinulescu et.al. [57] suggested the following anode heat flux expression considering the negative anode sheath voltage fall and electron diffusion current:

$$q_{el}= \mathrm{j}(3.2\frac{k_BT_e}{e}+\phi_a)\ , \tag{2.55a}$$

$$q_a=-\lambda_e\nabla T_e-\lambda_h\nabla T_h+q_{el}+q_R, \tag{2.55b}$$

where the factor 3.2 originates from $\frac{eD_T}{k_B\sigma}$ defined in [57] for atmospheric argon plasma, D_T is the thermal diffusion coefficient, the surface radiation heat fluxq_R can be calculated by $-\epsilon\sigma_{ST}T^4$, where σ_{ST} is the Stefan-Boltzmann constant, thermal emissivity ϵ for copper anode is 0.02. As anode sheath model is not considered in this scope, the exact value of U_a required in Eq.2.54 cannot be attained, the heat flux expression of Eq.2.55b is utilized in this study.

2.2.2 Heat flux on the plasma-cathode interface

Heat transfer between cathode and plasma makes itself more complicated in comparison with anode region due to the heating effect on its surface by ion bombardment, cooling effect by thermionic emission and many other secondary current categories. The total current density in front of cathode surface can be described using a complex of four partial current densities:

$$J = \bar{z}_iJ_i+J_{em}+J_{sem}-J_{bd}, \tag{2.56}$$

where J_i denotes the positive ion current density at cathode surface, $\overline{z_i}$ is the averaged ion charge number. The positive ions are accelerated due to the cathode sheath voltage fall and bombard with cathode surface and finally recombine with electrons around, thus convert its kinetic energy and neutralization energy to the heat flux onto the cathode surface.

J_{em} is the thermionic emission current density, which is due to electron emission from a high temperature metal surface. It is the most important surface ionization process in thermal plasmas. The electrons which stay inside metal cathode are heated up until the kinetic energy of those electrons surpass the potential barrier or the so-called work function. The emitted electrons can stay in the surface vicinity, creating space-charge and preventing further emission. This space-charge effect will be discussed in the next section. It is quantified by the Richardson-Dushman formula:

$$J_{em} = A_G T_w^2 \exp[-\frac{e}{k_B T_e}(\phi_c - \nabla\phi)], \tag{2.57}$$

where T_w is cathode surface temperature, A_G = 3.2× 10^4 A /(m^2K^2) for thoriated tungsten cathode which is simulated here, and the work function ϕ_c is 2.6 eV [30].The decrease of work function $\nabla\phi$ caused by the field-enhanced thermionic emission or the so-called Schottky effect is defined as :

$$\nabla\phi = \sqrt{\frac{e^3 E_c}{4\pi\varepsilon_0}}, \tag{2.58}$$

where E_c is the electric field at the cathode surface, this is calculated according to the following expressions [58]:

$$E_c = \sqrt{\frac{2n_{is}}{\varepsilon_0}\left[m_h\left(\frac{v_+^3 - v_-^3}{6u_i} - v_s^2 - \frac{u_i^2}{3}\right) - zk_B T_e(1 - \exp(-\frac{eU_d}{k_B T_e}))\right]}, \tag{2.59a}$$

$$v_\pm = \sqrt{(v_s \pm u_i)^2 + \frac{2zeU_d}{m_h}}, \tag{2.59b}$$

$$v_s = \sqrt{\frac{k_B(T_w + zT_e)}{m_h}}, \tag{2.59c}$$

$$u_i = \sqrt{\frac{k_B T_w}{m_h}}. \tag{2.59d}$$

where n_{is} is the ion number density at sheath/presheath interface, U_d is the sheath voltage drop magnitude. J_{sem} in Eq.2.56 is the secondary electron emission current density. Mechanisms of electron emission from electrodes, related to surface bombardment by different particles, are called secondary electron emission. This current density dominates in the early stage of discharge when cathode surface is not heated up enough to provide thermionic emission, hence it should not be neglected. According to Lichtenberg et al. [59] the secondary emission current density is proportional to the ion current density J_i:

$$J_{sem} = \gamma_{se} J_i, \tag{2.60}$$

where γ_{se} is the secondary emission coefficient which is related to plasma and electrode properties. Although γ_{se} is low at lower ion energies, it is not negligible and remains almost constant at ion energies below the kilovolt range. An ion approaching the electrode surface will extract an electron from there because the net energy (E_i-ϕ_c) is usually large enough to enable the escape of more than one electron from the surface. An empirical formula is applied in this scope to estimate γ_{se} [60]:

$$\gamma_{se} \approx 0.016(E_i - 2\phi_c). \tag{2.61}$$

J_{bd} is back diffusion current density caused by electrons from ionization layer moving in the sheath towards cathode:

$$J_{bd} = 0.25e\sqrt{\frac{8k_BT_e}{\pi m_e}}\, n_{es}\exp(-\frac{eU_d}{k_BT_e}) . \quad (2.62)$$

With all the current density categories above attained, the ion current density J_i can be calculated from the conservation of total current density (see Eq.2.56).

The total heat flux q_c transported to the cathode surface is related to the current density categories mentioned above:

$$q_c = \frac{J_i}{e}(\overline{z_i}k_BT_e/2+\overline{z_i}eU_d+\overline{E_i}-\overline{z_i}\,(\phi_c-\nabla\phi)) - \frac{(J_{em}+J_{sem})}{e}(2k_BT_w+(\phi_c-\nabla\phi))$$
$$+ \frac{J_{bd}}{e}((\phi_c-\nabla\phi)+2k_BT_e)+ q_R, \quad (2.63)$$

where the term $-\frac{(J_{em}+J_{sem})}{e}(2k_BT_w+(\phi_c-\nabla\phi))$ is the energy flux of emitted thermionic and secondary electrons that cools down the cathode surface concerning the combination of kinetic energy and neutralization energy according. ϕ_{eff} is the effective work function with Schottky correction as in Eq.2.57 and 2.58. The emissivity considered for calculating q_R with thoriated tungsten is 0.3. Suppose the ion temperature at cathode surface is equal to cathode surface temperature, $\overline{E_i}$ is the averaged the ionization potential of multilevel ionized argon plasma:

$$\overline{E_i} = \frac{\sum_{i=1}^{3}E_in_i}{\sum_{i=1}^{3}n_i} . \quad (2.64)$$

2.3 Simulation model of plasma boundary layer

At the very first stage when plasma is ignited, there is a small number of electrons leaving the cathode surface which then bombard with neutral atoms and make them positive charged ions. These ions along with the produced electrons move toward cathode together but with different velocity magnitudes since the electrons are much lighter than ions. At this stage there's a net electron current towards the objects that confine the plasma (usually it is called a wall). Over time this leaves the plasma bulk with a net positive charge and the electric potential of it will be raised above the walls. As this potential difference between the wall and bulk plasma grows, the electrons coming towards the wall are rejected or decelerated while ions are accelerated. As the bulk plasma needs to keep its quasi-neutrality, an equilibrium potential drop is required within a very thin layer to equalize electron and ion losses from bulk plasma. The thickness of this layer is usually of the order of several Debye length. As a result, the electron and ion flux which finally reach the cathode surface are consistent with each other. This effect within this very thin plasma boundary is called space-charge effect and this thin layer is often called sheath layer.

2.3.1 Basic equations of a collisionless planar sheath

To simplify the sheath model which plays an important role in the arc-electrode interaction but mathematically rather complicated, a good starting point is to assume it as a collisionless planar sheath region. Namely, suppose the mean free path of the ions is greater than the sheath layer thickness. As in the sheath layer, the particle movement in normal direction changes much more quickly than the transverse direction, it is always considered as a one-dimensional problem.

In the one-dimensional situation suppose ions start at sheath-plasma interface at x=0 with velocity of u_0 and $\varphi(0)$ =0. Conservation of energy requires that:

$$\frac{1}{2}m_h u^2 = \frac{1}{2}m_h u_0^2 - e\varphi(x), \tag{2.65}$$

where $\varphi(x)$ is the electric potential at position x.

Suppose there is no ionization process in sheath, so the ion flux continuity must be conserved:

$$n_0 u_0 = n_i(x)u(x), \tag{2.66}$$

where $n_0 u_0$ is the ion flux at plasma-sheath interface.

Combining Eq. 2.65 and Eq.2.66, the ion distribution in a collisionless planar sheath is:

$$n_i(x) = n_0\left(1 - \frac{2e\varphi(x)}{m_h u_0^2}\right)^{-1/2}. \tag{2.67}$$

The fluid momentum equation of electrons in one-dimension gives:

$$m_e n_e\left(\frac{\partial v_x}{\partial t} + (\vec{v}\cdot\nabla)v_x\right) = en_e E_x - \frac{\partial p_e}{\partial x}. \tag{2.68}$$

On short timescales, the electrons can be viewed as massless ($m_e \approx 0$), E_x is electric field of x direction and $p_e = n_e k_B T_e$, Eq.2.68 can be further simplified as:

$$e\frac{d\varphi(x)}{dx} = \frac{k_B T_e}{n_e}\frac{\partial n_e}{\partial x}. \tag{2.69}$$

After integration of n_e according to the equation above, the Boltzman's relation for electron number density gives:

$$n_e(x) = n_0 \exp\left(\frac{e\varphi(x)}{k_B T_e}\right). \tag{2.70}$$

The meaning of the existence of such density gradient is to set up a balance electric field to prevent electrons from being accelerate to infinite large velocity.

By substituting the expression for $n_i(x)$ and $n_e(x)$ in Eq.2.67 and 2.70 into Poisson's equation:

$$\epsilon_0\frac{d^2\varphi(x)}{dx^2} = e[n_e(x) - n_i(x)] = en_0\left[\exp\left(\frac{e\varphi(x)}{k_B T_e}\right) - \left(1 - \frac{2e\varphi(x)}{m_h u_0^2}\right)^{-1/2}\right]. \tag{2.71}$$

Because of the rejection of electron in sheath layer, the number density of electron inside sheath is much smaller than that of ion's, so:

$$\exp\left(\frac{e\varphi(x)}{k_B T_e}\right) < \left(1 - \frac{2e\varphi(x)}{m_h u_0^2}\right)^{-1/2}. \tag{2.72}$$

By making the first-order Taylor series approximation of both sides in Eq.2.72 at x=0, namely at plasma-sheath interface:

$$1 + \frac{e\varphi(x)}{k_B T_e} < 1 + \frac{e\varphi(x)}{m_h u_0^2}. \tag{2.73}$$

Because $\varphi(0) = 0$, $\varphi(x)$ inside sheath is <0, after rearrangement:

$$u_0 > \sqrt{\frac{k_B T_e}{m_h}} = u_B, \tag{2.74}$$

which is the well-known Bohm Sheath criterion that regulates the minimum ion velocity magnitude at sheath-plasma interface.

To accelerate ions to the so-called Bohm velocity before reaching the sheath layer, the models describing the attachment to a thermionic cathode divide the region between the cathode surface and

the bulk plasma should be supplemented by a so-called presheath zone that is quasi-neutral but wider than sheath layer thickness. According to Bohm sheath criterion, the minimum presheath potential φ_{pre} should be equal to:

$$\varphi_{pre} \geq \frac{1}{2e} m_h u_B^2 = \frac{k_B T_e}{2e}. \tag{2.75}$$

According to Boltzmann's relation the ratio of ion number density at plasma-presheath interface n_p to that at presheath-sheath interface n_s is:

$$n_s = n_p \exp\left(\frac{e\varphi_{pre}}{k_B T_e}\right) \cong 0.61 n_p \tag{2.76}$$

Applying the above descriptions for an idealized sheath with Bohm's criterion, the distributions of number density and electrical potential in the cathode boundary layers could be summarized by Fig.2.5 and 2.6.

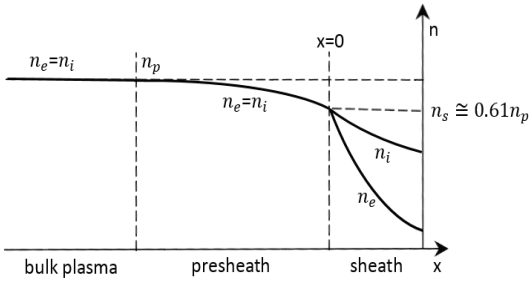

Fig.2.5. Particle number density distribution towards a collisionless planar sheath

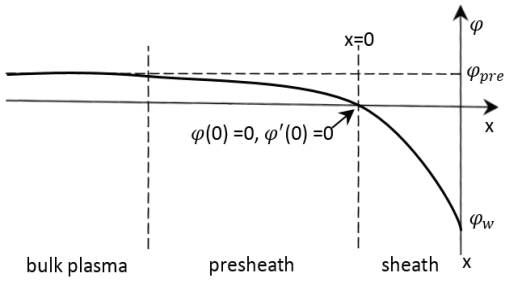

Fig.2.6. Electric potential distribution towards a collisionless planar sheath

Apart from the bulk-presheath-sheath regime described above, Shirvan et al. [27] and Baeva et al. [28] divided the presheath layer further into ionization and Knudsen layer. The difference between the two sublayers is that Knudsen layer mainly takes the responsibility for ions to be accelerated to Bohm velocity described above which allows then formation of sheath while the ionization layer mainly produces net electron production, some of which will have enough energy to go through sheath and form considerable J_{bd} to heat up cathode surface. In this scope, as the full consideration of plasma thermal and chemical nonequilibrium models is included, the extra division to allow for either the ionization or Knudsen layer may be no more necessary, leaving only the sheath layer left unable to be integrated into the numerical model.

2.3.2 Solution of the sheath potential drop

The solution of sheath potential drop is always a research focus for many to unlock the mysterious and complicated space-charge effect as it affects not only the plasma composition but also its energy transfer with electrodes (Eq.2.63). However, in order to solve this parameter, many related parameters should be solved together not only in plasma region but also in electrode region. There's therefore still no universal applicable expression for it which brings difficulty for the analysis of interaction process. A practical way is to make it simplified based on the ideal conditions.

Suppose in equilibrium the net current to a non-emitting floating wall is zero. This means the ion and electron balance each other at a floating wall or electrode surface. As no ionization process is assumed

due to the collisonless assumption inside the sheath layer, the ion flux is constant throughout the sheath so it equals to $n_0 u_B$. For electron flux at a floating wall, based on Boltzmann's relation it gives:

$$\Gamma_e = \frac{1}{4} n_0 \exp\left(\frac{e\varphi(x)}{k_B T_e}\right) \bar{v}_e, \tag{2.77}$$

where $\bar{v}_e = \sqrt{\frac{8k_B T_e}{\pi m_e}}$ is the thermal velocity of an electron according to the Maxwellian distribution discussed in section 1.1.3.

Substituting for the Bohm velocity u_B and equating the fluxes of Γ_i and Γ_e gives:

$$n_0 \sqrt{\frac{k_B T_e}{m_h}} = \frac{1}{4} n_0 \exp\left(\frac{e\varphi(x)}{k_B T_e}\right) \sqrt{\frac{8k_B T_e}{\pi m_e}}. \tag{2.78}$$

Solving the above equation for sheath potential drop at a floating wall $U_{df} = -\varphi(x)$ gives:

$$U_{df} = \frac{k_B T_e}{e} \ln \sqrt{\frac{m_h}{2\pi m_e}}. \tag{2.79}$$

This gives a classical sheath potential drop over a floating wall. The factor $\ln \sqrt{\frac{m_h}{2\pi m_e}}$ for argon plasma simulated here is about 4.68. However, as in arc or glow discharge operations, due to the influence of external electric field, the ions may be accelerated faster than the ideal Bohm velocity at presheath-sheath interface, and the net charged particles reaching electrode surface may not be zero, for example inside cathode spot. Nevertheless, this result serves as a good estimation for further quantified analysis of sheath which is important for the overall interaction model.

Except for the method based on Bohm's criterium discussed above, another way to solve sheath potential drop is to make use of energy conservation equations either at cathode surface or at sheath-presheath interface. According to [1], the energy conservation at both sides of sheath-presheath is given as follows:

$$\begin{aligned} &(J_{em}+J_{sem})(2k_B T_w + eU_d - e\nabla\phi) + J_i\,(2k_B(T_i - T_w) + \frac{\bar{z}_i k_B T_e}{2} + \bar{E}_i) \\ &= J_{bd}(2k_B T_e + eU_d - e\nabla\phi) + 3.2 J k_B T_e. \end{aligned} \tag{2.80}$$

At cathode surface it gives:

$$\begin{aligned} &-\lambda_e \nabla T_e - \lambda_h \nabla T_h + q_{RP} - (J_{em}+J_{sem})(2k_B T_w + (\phi_c - \nabla\phi)) + J_i(\bar{z}_i k_B T_e/2 + \bar{z}_i eU_d + \bar{E}_i - \bar{z}_i(\phi_c - \nabla\phi)) \\ &= -\lambda_s \nabla T_s + q_{RS}, \end{aligned} \tag{2.81}$$

where q_{RP}, q_{RS} are the radiation flux from plasma to cathode and from cathode to plasma respectively. Using the equations above to solve sheath potential drop can spare many unnecessary assumptions and simplifications. However, it is obvious from above that too many parameters are involved in the equations in order to get U_d. As U_d is also involved in the exponential term of J_{bd}, hence there's no direct expression for it. For Eq.2.81, as the difficulty in extracting thermal conduction term in metal electrode is concerned in OpenFOAM, a direct solution is unavailable either. A simple and useful expression to attain U_d is put forward by Wendelstorf [61], which is based on the expression of Eq.2.80 by preserving J_{em} and J_i as the only two current densities and recombination heating energy and thermionic cooling energy as the only two energy balance terms. For the inclusion of Knudsen layer acceleration, a factor 0.61 (see Eq.2.76) is applied into the following relation.:

$$U_d = \frac{\sum_{i=1}^{3} 0.61 z e n_i u_B E_i}{e J_{em}}. \tag{2.82}$$

Even when a simplified expression of cathode sheath voltage drop is available now, it cannot be implemented into the computation model by imposing it into the field calculation of φ. As sheath layer thickness is extremely small, imposing even a small amount of voltage drop into the potential will give rise to extreme large value of local current density which leads to unrealistic Joule heating and divergence of T_e equation. This bounded by the continuity property of Navier–Stokes equations which is very sensitive to abrupt local gradient, which also explains why only charge neutrality condition can be solved by this method. If the abrupt electron number density drop according to Boltzman's relation (Eq.2.70) were imposed inside this extremely thin layer, it would give rise to high electron temperature gradient which shares the same consequence with the first situation. This means a compromised method which avoid such abrupt local gradient but still yields, for example the large local electric potential change characterized by space-charge effect is needed here by common CFD method. When searching for the solution in Eq.2.37 and 2.52, apart from current density J, electric potential φ or magnetic vector potential $\vec{A}$, the only parameter that allows to be modified with little risk of numerical oscillation may be the electrical conductivity σ. A detailed discussion in section 2.5.4 is based on such advantages.

For a better conclusion of the model assumptions and simplifications discussed above for the calculation of U_d used in this scope, a simple schematic drawing of the cathode-plasma interaction regions is provided (Fig.2.8) with a comparison of Zhou's [18] full set of arc-cathode interaction model(Fig2.7):

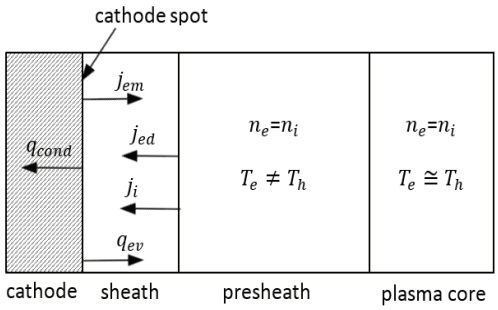

Fig.2.7. Schematic drawing of the near-cathode region by Zhou

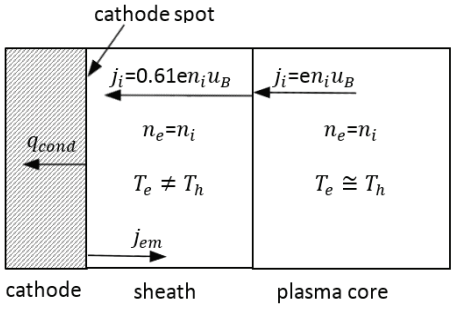

Fig.2.8. Schematic drawing of near-cathode model assumptions used in this scope

2.3.3 Child-Langmuir Law and electrical conductivity of collisionless sheath

For cathode sheath, the potential drop U_d of the whole layer is always so large that except the emission center the electron density n_e according to Boltzmann's law is negligible in comparison with ion number density n_i, so the Poisson's equation of a collisionless sheath layer described in Eq.2.71 can be simplified as:

$$\varepsilon_0 \frac{d^2\varphi(x)}{dx^2} = \mathrm{e}[-n_i(\mathrm{x})] = -\mathrm{e}n_0\left(1-\frac{2e\varphi(x)}{m_h u_0^2}\right)^{-1/2}. \tag{2.83}$$

As for large sheath potential drop, the increase of ion kinetic energy after being accelerated by sheath electric field is $|\mathrm{e}\varphi(\mathrm{x})|$ is dominant over the initial ion kinetic energy $\frac{1}{2}m_h u_0^2$, so by neglecting ion initial kinetic energy Eq.2.83 can be further simplified as:

$$\varepsilon_0 \frac{d^2\varphi(x)}{dx^2} = \mathrm{e}[-n_i(\mathrm{x})] = -\mathrm{e}n_0\left(-\frac{2e\varphi(x)}{m_h u_0^2}\right)^{-1/2}. \tag{2.84}$$

Multiplying the both sides of Eq.2.84 by $\frac{d\varphi}{dx}$ and then integrating from 0 to position x assuming the potential at presheath-sheath interface $\varphi(0)$ =0 and the electric field outside sheath is negligible $\frac{d\varphi(0)}{dx}$ ≈0 it gives:

$$\frac{1}{2}\left(\frac{d\varphi(x)}{dx}\right)^2=\frac{2J_0}{\varepsilon_0}\left(\frac{2e}{m_h}\right)^{-1/2}\sqrt{-\varphi(x)}. \tag{2.85}$$

Note that $\varphi(x)$ is always negative throughout the sheath. J_0 = en_i(x)u_i(x) is the sheath ion current density whose value is constant since no collision or ionization is assumed.

Taking the negative square root since $\frac{d\varphi(x)}{dx}$ is negative and rearrange Eq.2.85:

$$[-\varphi(x)]^{-1/4}\mathrm{d}\varphi(x)=2\sqrt{\frac{J_0}{\varepsilon_0}}\left(\frac{2e}{m_h}\right)^{-1/4}\mathrm{dx}. \tag{2.86}$$

Integrating Eq.2.86 for both sides gives:

$$-\varphi(x)^{3/4}=\frac{3}{2}\sqrt{\frac{J_0}{\varepsilon_0}}\left(\frac{2e}{m_h}\right)^{-1/4}\mathrm{x}. \tag{2.87}$$

Suppose the potential at sheath-electrode interface is $\varphi(s)$ and sheath layer thickness is s, Eq.2.87 is rearranged as:

$$J_0=\frac{4}{9}\varepsilon_0\sqrt{\frac{2e}{m_h}}\frac{(-\varphi(s))^{3/2}}{s^2}. \tag{2.88}$$

This is known as the Child-Langmuir law of space-charge-limited current. It gives the current density between two electrodes when potential drop in-between is known and electrode spacing is fixed. But when applied in the sheath model, this length scale simply represents the sheath layer thickness since no potential drop is assumed outside sheath layer. The sheath thickness s can be approximated by relating the ion current to Child law allowing for the pre-sheath ion number decrease by adding the factor 0.61 for argon plasma:

$$0.61\mathrm{e}n_0u_B=\frac{4}{9}\varepsilon_0\sqrt{\frac{2e}{m_h}}\frac{(-\varphi(s))^{3/2}}{s^2}, \tag{2.89}$$

where u_B=$\sqrt{\frac{k_BT_e}{m_h}}$. Thus the corrected Child law sheath thickness s for argon plasma gives:

$$\mathrm{s}=0.854\sqrt{\frac{\varepsilon_0}{n_0}}\left(\frac{2}{ek_BT_e}\right)^{1/4}(-\varphi(s))^{3/4}. \tag{2.90}$$

As the exact expression for sheath potential drop is still unknown, it is reasonable to use the simplified sheath potential drop U_d shown in Eq.2.82 as an estimation for sheath thickness. Substituting this expression as $\varphi(s)$ into Eq.2.90, and according to Ohm's law in one-dimension:

$$\mathrm{j}=\sigma\frac{d\varphi(x)}{dx}. \tag{2.91}$$

it is clear if replacing j in Eq.2.91 by 0.61en_0u_B, *dx* by s in Eq.2.90, a simple approximation of electrical conductivity inside the high voltage collisionless sheath layer σ_{sh} of an argon plasma without electron emission (thermionic, secondary etc.) can be attained by Eq.2.92, the attained values for it within electron temperature from 500K to 25000K are shown in Fig.2.9:

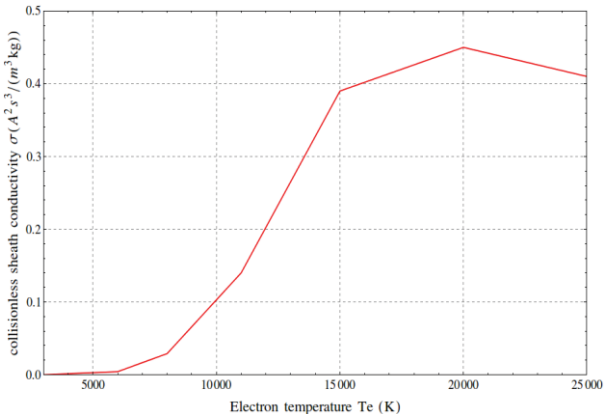

Fig.2.9. Calculated collisionless sheath conductivity of atmospheric argon plasma

$$\sigma_{sh}=\frac{0.61en_0u_Bs}{U_d}. \tag{2.92}$$

It is obvious from Fig.2.9 that even if at high electron temperatures, the sheath conductivities still remain at very low values. This is due to the assumption by Child's sheath that the voltage drop is so high that no electrons remain inside it. In comparison to it, the nonequilibrium electrical conductivity inside bulk plasma at high electron temperatures is always very high (for example, when Te= 15000K, θ=3, σ reaches the value of 7600 S/m), which suggests that there could be a complex description linking these two sets of conductivities, but not simply the above formula for sheath.

This complicated evolution in sheath layer may explain why during arc discharge, the cathode surface is only intensively heated within the cathode spot, while outside the spot where space-charge effect dominates, the thermionic emission is inactive or even cannot be observed. Different from the transition of sheath electrical conductivity assumed in this study, according to Shirvan et al. [27], the non-uniform electron emission at cathode surface is due to the diffusion or redistribution of rare earth activators inside cathode while local work function differs from place to place due to the non-uniform concentration of e.g. ThO_2. Some other researchers [62] attribute this phenomenon to the variation of local thickness of sheath layer. Because the general expression of Debye length in a plasma gives the following form:

$$\lambda_D=\sqrt{\frac{\varepsilon_0k_BT_e}{n_ee^2}}. \tag{2.93}$$

And it is clear that $\lambda_D \propto \sqrt{\frac{T_e}{n_e}}$. It means at the place where this factor is small or in other words the sheath thickness is small, the electric field strength will be higher. It will accelerate ions to a larger velocity that bombard cathode surface. Experiments by Puchkarev et al. [63] and simulation by Uimanov [64] have shown that ion bombardment heating is critical for the formation of the explosive emission on the cathode surface. It will further give rise to a larger increase of cathode surface temperature in these places and an intensive thermionic emission according to Eq. 2.63. Correspondingly, the current density from this place out of the cathode is much larger and will heat the plasma and make it produce more electrons that further shrink the sheath thickness. As a result, the sheath thickness within the emission center will be thinner and thinner driven by this process gradually. Compared with the colder sheath regions where there's little emission, this thickness is negligible, or we can assume that the sheath effect at these places can be neglected. According to [62], as the plasma conditions change rapidly, there are always some dynamic "sheath holes" that appear where emission centers locate. The "hole" means that a location may exist without sheath. This is a

useful concept for the interaction model, difficulty is, how can an emission center be captured by numerical method and how can this “hole” effect be described.

Based on this fact, for the sake of a reasonable sheath boundary condition to be applied in this study, there should be a smooth transition from the hot, sheath-free emission center to the cold, insulated and “thick” sheath (here a collisionless Child Sheath is assumed) reflecting the non-uniform distribution of cathode surface current density.

2.4 Plasma turbulence model

As is discussed in section 1.1.5, the stability of an arc inside a plasma torch will have a direct effect on the working efficiency of plasma spraying. As a matter of fact, there are a lot of factors that break such stability. Apart from the imbalance of magnetic body force and das dynamic drag force, and the potential theory of micro-discharging in anode region characterized by the reattachment regime, the plasma turbulence will play an important role on it. Although there will not be a fully developed turbulent flow throughout the whole region of a non-transferred plasma torch, the turbulent flow property will still appear at the region of interest. For example, downstream of the cathode jet the flow inside the anode nozzle can be considered as pipe flow, given the inner diameter of anode for a common commercial plasma torch is 8mm, taking numerical results from [65] for example, the argon plasma is heated to 32000K, which will have a LTE density of 5.37× $10^{-3} kg/m^3$, and LTE viscosity of 6× 10^{-6} $kg/(ms)$, the usual averaged maximal velocity is of 1000m/s, the Reynold number in this situation is over 7000, which is large enough to trigger turbulence. For a comprehensive description of arc jet instability inside the plasma torch, a suitable turbulence model needs to be included.

DNS and LES simulation methods are abandoned in this scope due to the requirement of large computation resource despite of their higher accuracy. As for the calculation of sheath layer presented later, the boundary mesh at cathode surface must be extremely thin that the centers of cathode boundary cells are within the viscous sub-layer. It is therefore necessary for this situation to use a low-Re RANS turbulence model.

A hybrid turbulence model SST k-ω developed and revised by Menter et al. [66] is adopted in this study. This model combines the widely-used k-ε [67]and k-ω[68] model together, since both of them have advantages and disadvantages. For example, k-ε model is not able to capture the proper behavior of turbulent boundary layers up to separation despite of its robustness in convergence, while k-ω model shows a strong sensitivity to the values of ω in the freestream outside the boundary layer. Despite its superior performance in the near wall region, the freestream sensitivity has largely restricted its application. The hybrid model SST k-ω makes good use of the advantages of both models, it transforms the k-ε model into k-ω model in the near -wall region and the standard k-ε model is applied in the fully turbulent region far from the wall while no damping functions are needed. The exact form of this two-equation eddy-viscosity model derived for the transient regime required here is as follows:

$$\frac{\partial \rho k\vec{u}}{\partial t} + \nabla \cdot (\rho k\vec{u}) = \nabla \cdot [(\mu + \mu_t \sigma_k)\nabla k] + P_k - \beta^* \rho k\omega, \tag{2.94}$$

where

$$P_k = \min\left(\mu_t \frac{\partial u_i}{\partial x_j}\left(\frac{\partial u_i}{\partial x_j} + \frac{\partial u_j}{\partial x_i}\right), 10\beta^* \rho k\omega\right) \tag{2.95}$$

is the limiter of turbulent kinetic energy production rate to prevent the build-up of turbulence in stagnation regions.

$$\frac{\partial \rho\omega\vec{u}}{\partial t} + \nabla \cdot (\rho\omega\vec{u}) = \nabla \cdot [(\mu + \mu_t \sigma_\omega)\nabla\omega] + 2(1-F_1)\rho\sigma_{\omega_2}\frac{1}{\omega}\frac{\partial k}{\partial x_i}\frac{\partial \omega}{\partial x_i} + \alpha\rho S^2 - \beta\rho\omega^2, \tag{2.96}$$

where S is the invariant measure of the strain rate, the first blending function F_1 gives:

$$F_1 = \tanh\left\{\left\{min\left[max\left(\frac{\sqrt{k}}{\beta^*\omega y}, \frac{500\nu}{y^2\omega}\right), \frac{400\rho\sigma_{\omega_2}k}{CD_{k\omega}y^2}\right]\right\}^4\right\}, \quad (2.97)$$

where $CD_{k\omega}$ =max ($2\rho\sigma_{\omega_2}\frac{1}{\omega}\frac{\partial k}{\partial x_i}\frac{\partial \omega}{\partial x_i}$,$10^{-10}$), y is the distance to the nearest wall.

The blending function F_1 is used to achieve a smooth transition between the two models. It modifies not only the cross-diffusion term, but also the model coefficients that are originally used separately:

$$C = F_1 C_1 + (1 - F_1)C_2, \quad (2.98)$$

where C_1 refers to the constants or parameters related to k-ω model and C_2 for k-ε model. F_1 equals to 0 when far from the boundary wall (turbulent core region) and equals 1 when inside the viscous sub-layer.

The eddy viscosity is limited to give improved performance in flows with adverse pressure gradients and wake regions:

$$\mu_t = \frac{a_1\rho k}{\max(a_1\omega, SF_2)}, \quad (2.99)$$

where the second blending function F_2 is defined by:

$$F_2 = \tanh\left[\left[max\left(\frac{2\sqrt{k}}{\beta^*\omega y}, \frac{500\nu}{y^2\omega}\right)\right]^2\right]. \quad (2.100)$$

The constants used in this model are given as follows:

Table.2.2. Coefficients used in the scale-adaptive k-omega-SST model

coeff. / model component	α	β	β^*	σ_k	σ_ω	a_1
k-ω model	5/9	3/40	0.09	0.85	0.5	0.31
k-ε model	0.44	0.0828		1	0.856	

Besides, in the near wall region, one usually needs to apply fine meshes to resolve the viscous sub-layer in low Re turbulence model, it increases computation costs. At the same time, the precise y^+ value cannot always be controlled well by users since the mesh spacing for complicated geometries seems hardly to be uniform. This will introduce further uncertainties to the model. As the distance y is contained in the blending functions in this model, the effective turbulent viscosity and transport equations used can adjust themselves to suit the real grid spacing which means it is compatible with both fine (fixed value) and coarse (wall functions) meshes. This feature is particularly useful in this scope as not all the boundary cells are necessarily fine as those in the cathode sheath layer (for example boundary cells which are neither in anode nor in cathode regions), these regions can be safely calculated with coarse meshes and wall functions, and the computation costs can be reduced to some extent. Menter [66] has demonstrated that the wall shear-stress results using this model for Couette flows simulations on three vastly different grids (y^+~0.2, y^+~9, y^+~100) vary only by less than 2% despite of different near wall treatments.

2.5 Boundary conditions

For a sound simulation without problems such as numerical stability, a set of realistic boundary conditions needs to be given. This proper set of boundary conditions is particularly important at interfaces since different regions need to be solved separately while each of them interacts with another in quite different ways. What's more, sheath layer at cathode needs to be handled along with them.

2.5.1 Temperature field

As the NLTE simulation model asks the total enthalpy to be spitted into h_h and h_e , therefore two sets of boundary conditions need to be set in fluid region. For simplicity, the inlet temperature for heavy species is fixed at 500K while for all the outlet boundaries is set *inletOutlet* which regulates temperature between Dirichlet and Neumann conditions according to local direction vector of velocity. Attention should be drawn to the interface boundaries. Since coupled simulation requires no presumed or predefined temperature distribution along the interfaces, it calculates the surface temperature self-consistently according to Fourier's law for plasma-cathode , plasma-anode and other interfaces respectively (Eq.2.101):

$$\lambda_h A \frac{T_{cp}-T_p}{\Delta x_p} + A q_e = \lambda_s A \frac{T_p - T_{cs}}{\Delta x_s}, \tag{2.101}$$

where Δx_p and Δx_s are the distances from cell center to patch of fluid and solid regions, the meanings of the suffix for the boundary values introduced in the equations above are shown in Fig.2.10. Because OpenFOAM identifies the interface temperatures of both regions with each other, the patch temperature T_p is used in both regions. A is the patch surface area. q_e equals q_a from Eq. 2.55a-b if at anode surface while it equals q_c from Eq. 2.63 if at cathode surface, with the exception that the radiation term q_R needs to be corrected by considering the incident radiation heat flux q_{Ri} from plasma ($q_{Rt} = q_R + q_{Ri}$). To get the boundary condition for the incident radiation flux from arc plasma, the incident radiation intensity G is calculated according to P1 model:

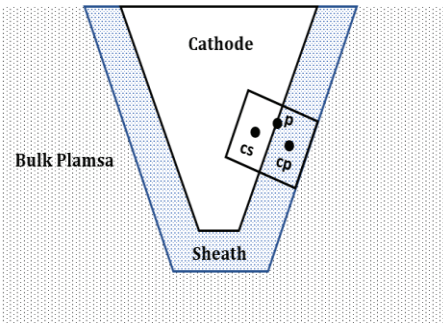

Table.2.10. Schematic description of boundary cell parameter configurations

$$\nabla \cdot (\Gamma \nabla G) - \alpha G + 4\alpha\sigma_{SB}T^4 = 0, \tag{2.102}$$

where α is the band-averaged absorption coefficient following section 2.1.3. By neglecting the scattering process and the linear-anisotropic phase function coefficient, the parameter Γ gives:

$$\Gamma = \frac{1}{3\alpha}. \tag{2.103}$$

Then the incident radiation flux at the electrode surface q_{Ri} is related to the normal gradient of G:

$$q_{Ri} = -\Gamma \frac{\partial G}{\partial n}. \tag{2.104}$$

The Marshak boundary condition is used here to eliminate the angular dependence, and suppose the electrode surfaces are opaque surfaces and then make balance between incident, reflected and emitted radiation energy it gives:

$$q_{Ri}= -\frac{\epsilon}{2(2-\epsilon)}(4\sigma_{SB}T^4-G_w), \tag{2.105}$$

where ϵ is set 1 at inlet and outlet to assume black body absorption, G_w is the incident radiation intensity at wall.

For electron temperature the inlet temperature is set 500K whereas the other boundary conditions are set zero gradient. The initial value of T_e is given at 5000K so that the instability of electron enthalpy due to a much too small value of σ could be avoided. As in solid regions no electron temperature needs to be considered, the solid region temperature is onefold and "connected" to heavy species temperature T_h in fluid region through Eq.2.101.

2.5.2 Velocity field

Arcs can be stabilized either by a cylindrical wall (wall stabilization) that forces the arc to remain on the axis of the cylinder or by a superimposed axial cold gas flow, this increases the efficiency of convective heat transfer on anode surface to avoid erosion and cools off the arcs moves off the axis (flow stabilization). This kind of stabilization is particularly effective when a swirl injection is applied at gas inlet. This is usually achieved by a flow swirler that produces inlet velocity with a tangential component. This strengthens the fluid rotational movement especially at anode nozzle, whose diameter is smaller than that of inlet. It reduces the residence time of anode attachment which is correlated with the swirl velocity. Less heat load and erosion can be expected with this strategy. In this study, a mass flow rate boundary condition of 60 slpm with $45°$ swirl is defined. In OpenFOAM, there's a boundary condition type named *swirlFlowRateInletVelocity* suitable for this condition. It describes the volumetric/mass flow normal vector boundary condition by its magnitude as an integral over its area with a swirl component determined by the RPM (revolutions per minute). As the swirl angle is defined as:

$$\vartheta=\text{atan}(\frac{\sqrt{\vec{v}^2+\vec{w}^2}}{\sqrt{\vec{u}^2}}), \tag{2.106}$$

where $\vec{u},\vec{v},\vec{w}$ is the velocity component of x, y, z direction and x direction is assumed to be the normal direction here. So for $45°$ swirl:

$$\sqrt{\vec{u}^2}=\sqrt{\vec{v}^2+\vec{w}^2}. \tag{2.107}$$

To get the value of RPM required for this boundary condition, it is necessary to estimate the normal velocity magnitude beforehand. It is assumed that there's a fully developed laminar flow at the inlet, the magnitude profile of normal velocity as a function of radial position r is given by [42]:

$$\sqrt{\vec{u}^2}=2\bar{u}\left[1+f^2-\frac{(1-f^2)}{\ln(\frac{1}{f})}\right]^{-1}\left[1-\left(\frac{r}{R_a}\right)^2+(1-f^2)\frac{\ln(\frac{r}{R_a})}{\ln(\frac{1}{f})}\right], \tag{2.108}$$

$$f=\frac{R_c}{R_a}, \tag{2.109}$$

$$\bar{u}=\frac{\dot{m}}{\rho\pi R_a^2(1-f^2)}, \tag{2.110}$$

$$\text{RPM}=9.55\frac{\sqrt{\vec{u}^2}}{r}, \tag{2.111}$$

where $\dot{m}$ is the inlet mass flow rate, ρ is the inlet gas density, R_c, R_a are the radius of cathode and internal radius of anode. RPM is approximated at the place of maximal normal velocity.

At all solid walls the non-slip boundary is defined, since the operation condition of the plasma torch discussed here is under atmospheric pressure, and the Knudsen number at the solid boundary is small enough. At outlet, a generic outflow condition zeroGradient is implemented. By setting the boundary patch value to the boundary internal value, the continuity equation is also fulfilled at outlet.

The two key parameters turbulent kinetic energy k and specific dissipation rate ω used in the turbulence model as a fixed value at inlet are calculated as follows:

$$k = 1.5(|u|I)^2, \tag{2.112}$$

$$\omega = 1.826\frac{\sqrt{k}}{l}, \tag{2.113}$$

where the turbulence intensity I is estimated as 1%, and the turbulence length scale l is attained by 0.038d while d is the anode inner diameter.

For near wall treatment, as the grid spacing at anode and cathode boundaries are made fine enough (y^+<1) to resolve sheath and heat transfer, the k boundary condition here is fixed as an infinite small value to avoid zero value at denominator. For other wall boundaries, due to the coarse meshes (y^+>30), the standard wall function is used.

2.5.3 Pressure field

The initial pressure value throughout the whole computation domain is set as 1.013×10^5 Pa. At all solid walls the boundary condition is zero gradient. As the geometry of plasma torch anode is concerned, the plasma flow in- and outside anode pipe is subsonic. Besides, the whole geometric domain is extended faraway enough from the arc jet, therefore no specific treatment for wave reflection at outlet is needed, a generic total pressure p_t boundary condition with a reference pressure p_0 1.013×10^5 Pa according to Bernoulli's principle is applied:

$$p_t = p_0 + \frac{1}{2}\rho u^2. \tag{2.114}$$

At inlet the boundary condition is set as zero gradient, thus the pressure value is determined according to ideal gas law with temperature and velocity field calculated at the same place.

2.5.4 Electric potential field

Choosing a suitable boundary condition for electric potential is a most important and challenging task for building a good plasma-electrode interaction model. Because the current density is calculated according to Poisson's equation, which is subject to the distribution of plasma electrical conductivity and electric potential. The current density is then used to calculate the joule heating, which is a decisive source term in electron enthalpy equation and in turn gives rise to heavy species temperature rise and the development of velocity and pressure field.

A reasonable boundary condition for electric potential should firstly ensure the charge conservation or the continuity of electric current density. As no cathode evaporation is assumed here, no extra current caused by particles of cathode materials will be produced, which means the current flow at both sides is identical in value. To achieve that, it is advisable to use a boundary condition similar to Eq.2.101:

$$\sigma_p A \frac{\varphi_{cp}-\varphi_p}{\Delta x_p} = \sigma_s A \frac{\varphi_p-\varphi_{cs}}{\Delta x_s}. \tag{2.115}$$

This ensures not only that the current density generated in the boundary cells of fluid region will be equal to what's generated in the neighboring boundary cells of electrodes, but also ensures that the potentials of both regions agree on the interface.

Besides, it will be more important to know what the electrical conductivities σ_p and σ_s in boundary cells of both regions could be. Apparently, the solid conductivity σ_s is merely a function of temperature while fluid conductivity σ_f is linked to the complicated sheath layer. As is discussed in 2.3.2, the electron number density in the sheath layer is assumed to be identical with ion number density, otherwise the abrupt drop of number density will cause unphysical or divergent simulation results. This phenomenon of electron rejection, however, is very important to a coupled simulation taking into account the sheath effect. In this scope, it is done in another way. If one takes a look at the classical expression of plasma electrical conductivity, it gives:

$$\sigma = \frac{n_e e^2}{m_e \sum_{i=0}^{3} \nu_{ei}}. \tag{2.116}$$

It obvious from above that $\sigma \propto n_e$, which means the electrical conductivity inside sheath should also be much smaller if no surface emission takes place. While changing the number density seems not reasonable, replacing σ meant for arc plasma core by a suitable value calculated for sheath is a good choice. Because by changing that parameter, only the joule heating term in electron enthalpy equation needs to be corrected, the transport equations have little risk overshooting or undershooting themselves.

Besides, as is discussed in section 2.3.3, sheath layer thickness is related to the local discharge condition. At the places where the Debye length is negligible, it can be considered as an absence of sheath effect or "sheath hole". This requires that the implemented sheath electrical conductivity should be able to reflect this situation.

There are usually two main difficulties in implementing a sound boundary condition for sheath. On one hand, it is not clear which mechanism regulates the accumulation of surface current density. One common assumption is that for a cathode with a conical shape, the emission concentrated at the tip of cathode, where the curvature is the largest. On the other hand, the real emission transition from arc to cold, inactive sheath is unknown.

It is common practice that most of the interaction researches assume that the current density decrease with a certain trend (functions that describe the distribution) beginning at the tip. These functions usually require an estimation of cathode spot radius. By setting a predefined arc spot region according to some empirical models of arc spot radius [15] may have its physical basis, but the final conducting region is thus restricted. It produces a much too arbitrary and symmetrical conducting region which fits the view of aesthetics but not reality.

According to Zhu et al. [23], a special form of Ohm's Law needs to be developed for a smooth transition of surface current density or, in other words, an effective electrical conductivity for sheath plays an important role for a self-consistency model. Since in the active spot region the plasma is always fully ionized while far away from the spot the cathode sheath remains cold and insulated, it is reasonable that the electrical conductivity of sheath plasma may also follow the trend of ionization degree. In this scope, a derived form of Ohm's Law for the calculation in boundary cells according to the local ionization degree I_g of plasma as a limiting factor between fully ionized plasma in arc spot and emission-free sheath layer is developed, which takes the form of effective value from [25]:

$$\sigma_{eff} = \frac{1}{\frac{1}{\sigma_{sh}}(1-I_g)+\frac{1}{\sigma}I_g}, \tag{2.117}$$

where σ is the electrical conductivity of bulk plasma, σ_{sh} is the collisionless sheath electrical conductivity without surface electron emission discussed previously (Eq.2.92), σ_{eff} is the total effective conductivity of sheath layer. The ionization degree I_g for multilevel ionized plasma is:

$$I_g = \frac{\sum_{i=1}^{3} n_i}{\sum_{i=0}^{3} n_i}, \tag{2.118}$$

It is obvious from this boundary condition that no extra factor relating to cathode geometry such as cathode spot radius is needed. At the place where $I_g \to 0$, the sheath electrical conductivity approaches σ_{sh} , while $I_g \to 1$, $\sigma_{eff} \to \sigma_{pl}$.That means the sheath effect disappears if local plasma is fully ionized. The ionization degree I_g is attained from the results of transport equations of plasma column, thus it yields a self-consistent solution of boundary conductivity that decides the non-uniformity of surface current density of cathode. As no anode sheath effect is considered in this scope, σ_{eff} remains σ inside it, as well as other non-conducting walls:

$$\sigma_{eff} A \frac{\varphi_{cps} - \varphi_p}{\Delta x_p} = \sigma_s A \frac{\varphi_p - \varphi_{cs}}{\Delta x_s}, \text{ (cathode sheath)} \tag{2.119}$$

$$\sigma_p A \frac{\varphi_{cps} - \varphi_p}{\Delta x_p} = \sigma_s A \frac{\varphi_p - \varphi_{cs}}{\Delta x_s}. \text{ (other interfaces)} \tag{2.120}$$

2.5.5 Magnetic field

The boundary condition for magnetic vector potential $\vec{A}$ is set zero gradient at gas inlet and the cold end of cathode and all the anode outer surfaces. To fix a reference value, vector potential is set (0,0,0) at gas outlet and anode outer boundary where it is far from the discharging region. A deduction process is needed to attain the relation between both sides of plasma-electrode interface.

Suppose a pillbox-like small volume (Fig.2.11) that crosses the interface with the height of h and the Coulomb gauge condition is:

$$\nabla \cdot \vec{A} = 0. \tag{2.121}$$

By setting h→0, the zero-divergence condition can be understood as the net flow entering the top surface (or bottom surface) of the small volume is equal to the flow leaving the bottom surface (or top surface) of the volume. So the normal component of vector potential A_n at both sides is consistent.

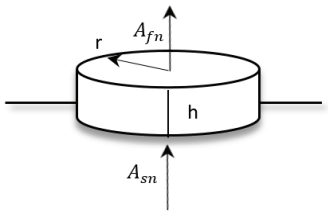

Fig.2.11. Schematic drawing of a divergence-free volume of vector potential across the cathode-plasma interface

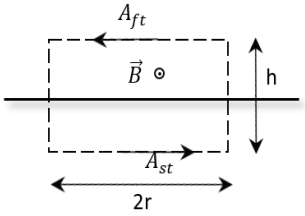

Fig.2.12. Schematic drawing of integration loop of vector potential tangential component across the cathode-plasma interface

The line integral of vector potential $\vec{A}$ around a curve C equals the magnetic flux through any surface S spanning the curve as :

$$\oint_C \vec{A} \cdot d\vec{l} = \int_S (\nabla \times \vec{A}) \cdot \vec{n}\, da = \int_S \vec{B} \cdot \vec{n}\, da = \Phi_B, \tag{2.122}$$

where Φ_B is the magnetic flux across surface S.

Suppose the integration path l to be a rectangle with the width 2r and height h (Fig.2.12). A_{ft} , $A_{fn}$and A_{st} , A_{sn}denote the tangential and normal components of vector potential in fluid and solid region. When h→0:

$$\oint_C \vec{A} \cdot d\vec{l} = A_{ft}\ 2r - A_{st}\ 2r = \Phi_B = \vec{B} \cdot \vec{n}\ 2r\ h \to 0. \tag{2.123}$$

It yields $A_{ft} = A_{st}$. So both the normal and tangential components of vector potential is identical to each other which yields the continuous boundary condition for magnetic vector potential $\vec{A}$ at plasma-electrode interfaces regardless of surface current densities:

$$\vec{A}_f = \vec{A}_s. \tag{2.124}$$

Because the magnetic flux density $\vec{B}$ is calculated explicitly according to $\vec{B} = \nabla \times \vec{A}$, it is not needed to impose any boundary condition for $\vec{B}$ in OpenFOAM.

2.6 Global coupling procedure

All the elementary descriptions of sub-models concerning different aspects of plasma-electrode interaction are presented in the previous sections in this chapter. *ChtMultiRegionFoam* loops from fluid regions to solid regions according to the region names defined in the case directory and solve them one by one sequentially. In this study, the fluid region is onefold, it consists only of plasma core and plasma sheath, which are connected to each other, while sold regions include anode, cathode and other neutral elements, which are separated from each other and has no sharing faces.

After the successful splitting of the meshes of ground level into corresponding sub-meshes and the initial and boundary conditions for all the involved parameter including T_h, T_e, p, $\vec{U}$,$\vec{A}$ etc. are set by *createFluidFields.H* and *createSolidFields.H*, respectively. The simulation starts within cells of the whole arc region from continuity equation *rhoEqn.H* through the momentum equation UEqn.H followed by T_e.*H* which contains all the necessary equations ranging from the calculation of number density by chemical nonequilibrium model till the calculation of electron enthalpy equation after all the transport and collisional parameters are attained. Then heavy species enthalpy equation is solved based on the result of Te to gain elastic collisional energy. In the next step, PISO algorithm comes to play to update pressure and density. It is important to note that if sheath region is included, the boundary cells attached to cathode surface are selected. The 2T electrical conductivity σ of boundary cells at cathode calculated previously is overwritten by the calculated results according to effective sheath conductivity of Eq.2.117 since the ionization degree is attained after the calculation of number densities. With all the necessary parameters are calculated (for example the T_w in Eq.2.57 is updated by the previous enthalpy equation, the heat fluxes q_a and q_c are attained by Eq. 2.55a-b and 2.63, which will serve as automatic input of Neumann boundary conditions for the electrode temperature calculation and at the same time, the temperature and electric potential results of plasma region attained will serve as Dirichlet boundary condition for electrodes as these values should be consistent at the interfaces), the solver begins to calculate the RANS turbulence fields by k and ω. After all the equations in electrode regions are solved based on the interface results from fluid region, the results of solid regions will also update all the important parameters at the interfaces to serve as Neumann or Dirichlet boundary conditions for fluid regions (this is why we call it “interaction”). Finally, the solver loops again from the very beginning following the above introduced sequence: arc→sheath→electrode until convergence is achieved.

Chapter 3

Numerical methods and solution procedure

As is in chapter 2 introduced, the whole interaction model is a complex of transport equations, supported by variables that change with space and time. However, due to the limit of computation resource and the need of computation stability, a lot of simplifications are made at the cost of global validity, e.g. the fluid method will not apply in low electron population area. Despite of that, the whole set of equation to be solved is still numerous and highly nonlinear. Choosing suitable numerical methods and solution procedures that suit not only the physical reality with an acceptable error margin but also the need of stable and economic computation will have a direct effect on the final applicability of the interaction model.

3.1 Overview of discretization

It is clear that in solving a complicated set of transport equations, there's seldom a possibility to get the analytical result. A good alternative is to "smash" the problem of specific into a finite number of units and then solve each of them. Each problem unit is not isolated, and one can use different predefined relations to connect each other and yield the final results if certain criterion of error is fulfilled. The finite volume method is one of the most famous computation methods that apply such procedure. It is a method for representing and evaluating partial differential equations in the form of algebraic equations. Similar to the finite difference method or finite element method, values attained by FVM are calculated at discrete places on a meshed geometry. Here the problem unit refers to the small volume surrounding each node point on a mesh, which justifies its name "finite volume". Different from the finite difference method, the computation spectrum includes not only the central node, but also the faces that surround it. All of them together is called a control volume. The method or process to "smash" the whole computation region is called discretization. Regardless of the differences among FVM, FEM and FDM, all discretize the problems by spatial discretization, temporal discretization and equation discretization.

3.1.1 Temporal discretization

The temporal discretization is done through integration over time on the general discretized equations. This method states that the time integral of a given variable is equal to a weighted average between current and future values. For example, the first time derivative $\frac{\partial}{\partial t}$ is integrated over a control volume as follows:

$$\frac{\partial}{\partial t}\int \rho\phi \mathrm{d}V. \tag{3.1}$$

The values that are involved in the temporal discretization are usually: the new time values ϕ^n=ϕ(t+Δt), namely the time step we are solving; old time values ϕ^o=ϕ(t), the values stored from the previous time step; ϕ^{oo}=ϕ(t-Δt), the values from the time step previous to the last. OpenFOAM provides the users with the possibility to define different time differencing schemes in the sub-dictionary *ddtSchemes* ranging from the steady-state to the second order implicit backward scheme. For example, when applying the most common first order Euler implicit scheme, the result of temporal integration of Eq. 3.1 can be discretized as:

$$\int_t^{t+\Delta t}\left[\frac{\partial}{\partial t}\int \rho\phi \mathrm{dV}\right]dt = \int_t^{t+\Delta t}\frac{(\rho\phi V)^n-(\rho\phi V)^o}{\Delta t}dt$$

$$= \frac{(\rho\phi V)^n-(\rho\phi V)^o}{\Delta t}\,\Delta t. \tag{3.2}$$

The spatial derivatives in a transient problem can be treated in a similar way if applying the explicit differencing scheme:

$$\int_t^{t+\Delta t}[A\phi dV]dt = \int_t^{t+\Delta t} A^*\phi dt$$

$$= A^*\phi^o \Delta \mathrm{t}, \tag{3.3}$$

where A^* represents the spatial discretization of operator A. Unlike the Euler implicit method, which applies the new time value to discretize and guarantees boundedness, the explicit method spares the process of solving the system of linear equations, its results can be attained directly. However, its applicability is restricted by the Courant number:

$$C_o = \frac{U_f d}{\Delta \mathrm{t}} < 1. \tag{3.4}$$

3.1.2 Spatial discretization

By spatial discretization the solution domain is defined by the location of points that are within the cell center and the faces that surround them, which are classified as internal faces and boundary faces. In general, the domain can be discretized by either a structured or an unstructured grid system. Structured meshes are identified by regular connectivity. The possible element choices are quadrilateral in 2D and hexahedra in 3D. This system is highly space-efficient since the neighborhood relationships are defined by storage arrangement. Some usual advantages of structured meshes over unstructured are better convergence and higher resolution. Additional flexibility of the structured meshes is that it can be used in multiple blocks, either joined together or treated independently, particularly when specific needs must be met, for example the multi-region feature of the plasma-electrode interaction simulation asks the total domain to be defined into different subdomains and calculated for different set of transport equations. Unstructured meshes are used when domains with complicated or changing geometry need to be discretized. Nowadays, as the simulation problem becomes larger and larger, and the manual mesh generation becomes very time-consuming, the ability of automatic generation of unstructured meshes or hybrid meshes that contain a mixture of structured portions and unstructured portions has been incorporated into all the commercial CFD software.

In OpenFOAM the computation results are stored in mesh with a wide variety of positions. Usually the scalar and vector fields such as temperature and velocity are stored in cell center, and quite often some parameters (convection mass flux) are stored at cell faces and on occasion some are defined on cell vertices. The specific choice of each storage form in OpenFOAM is given by the template class *geometricField<Type>.* By using *typedef* declarations, the corresponding storage forms can be manipulated with the following renamed classes [69]:

(1) volField<Type> : results calculated at control volume center.

(2) surfaceField<Type> : results calculated at faces surrounding a control volume.

(2) pointField<Type> : results calculated on the vertices of a control volume.

3.1.3 Equation discretization

Consider a classical steady-state convection-diffusion problem, the integral form of it gives:

$$\int_{CV} \nabla \cdot (\rho\phi\vec{u})\mathrm{dV} = \int_{CV} \nabla \cdot (\Gamma\nabla\phi)\mathrm{dV} + \int_{CV} S_\phi \mathrm{dV}, \tag{3.5}$$

where $\vec{n}$ is face normal vector, suppose that velocities and all the fluid properties are known, applying Gauss's divergence theorem:

$$\int_{CV} \nabla \cdot \phi \mathrm{dV} = \oint_A \vec{n} \cdot \phi \mathrm{dA}, \tag{3.6}$$

which can be further transfer to the sum of integrals over all faces (if the mesh is a hexahedron which has face A1 to face A6):

$$\oint_A \vec{n} \cdot \phi \mathrm{dA} = \sum_{A1}^{A6} \int_{A_i} \vec{n} \cdot \phi \mathrm{dA}. \tag{3.7}$$

Suppose the linear variation of the unknown ϕ:

$$\phi(\mathrm{x}) = \phi_P + (\mathrm{x} - x_P)(\nabla\phi)_P, \tag{3.8}$$

where x_P , ϕ_P, $(\nabla\phi)_P$ is the coordinate, value and gradient of control volume center. The term $\int_{A_i} \vec{n} \cdot \phi \mathrm{dA}$ can be splitted into:

$$\int_{A_i} \vec{n} \cdot \phi \mathrm{dA} = \phi_P \int_{A_i} \mathrm{dA} + (\nabla\phi)_P \int_{A_i} (\mathrm{x} - x_P)\mathrm{dA} = \mathrm{A}\phi_P. \tag{3.9}$$

Applying Eq.3.9 to Eq.3.7, the integration of transport terms in each control volume can be linearized with second order accuracy:

$$\int_{CV} \nabla \cdot \phi \mathrm{dV} = \sum_{A1}^{A6} \mathrm{A}\phi_P. \tag{3.10}$$

Based on the principle above, Eq.3.5 can be rewritten as:

$$\sum_{A1}^{A6} \mathrm{A}\rho\phi_P\vec{u} = \sum_{A1}^{A6} \mathrm{A}\Gamma\nabla\phi + \int_{CV} S_\phi \mathrm{dV}. \tag{3.11}$$

The source term above could also be generalized as:

$$\int_{CV} S_\phi \mathrm{dV} = S_u V_p + S_p V_p \phi_P. \tag{3.12}$$

For the convenience of description, the one-dimensional problem with velocity of positive x direction is assumed, reducing the neighborhood elements to only west and east components:

$$(\mathrm{A}\rho\phi\lceil\vec{u}\rceil)_e - (\mathrm{A}\rho\phi\lceil\vec{u}\rceil)_w = (\mathrm{A}\Gamma\nabla\phi)_e - (\mathrm{A}\Gamma\nabla\phi)_w + S_u V_p + S_p V_p \phi_P. \tag{3.13}$$

where the index e and w denote the corresponding east and west faces of control volume. To avoid storage overhead with additional addressing information, only the grid and face value of the CV itself and those of its neighbor cells take part in the linearization process.

However, all the CV faces are owned not only by the CV itself, but also by its neighbor cells except for the boundary faces. And to relate all the CV values together, there should be mechanisms that decide how can the face values be fixed concerning all the related CVs for the convection terms. Such mechanisms are called differencing schemes. The accuracy of each different differencing schemes depends on the choice of neighboring nodes, ranging from first-order up to several orders higher. However, there's till now no universally applicable differencing schemes that serve good accuracy, convergence and stability at all situations at one time. To increase the computation cell number can improve overall accuracy naturally, but also cost much more computation resource. In practice, if certain schemes fulfil the prescribed laws, the physically realistic results can also be expected. Such laws for choosing a suitable differencing scheme are called conservativeness, boundedness and transportiveness.

The conservativeness results from the need to secure the conservation of variables within the whole computation domain, that means the flux of ϕ leaving a CV across a certain face must be equal to the flux entering the adjacent control volume through the same face. If improper differencing is used, the gradient across certain face could be different due to the curvature, and the diffusion flux entering and leaving the same volume face could be inconsistent.

To ensure an iterative method is convergent, Scarborough [70] has shown that the coefficients matrix of ϕ in linearized equations should be diagonally dominant. Under such dominance and in the absence of source terms, the internal nodal values of ϕ could be bounded by its boundary values. Hence such criterium is often called boundedness. Besides, all these coefficients of linearized equations should have the same sign.

For fluid flow, transportiveness describes the influence on the upstream node on the downstream node. For zero Peclet number (pure diffusion), the iso-lines of ϕ around the node P are circular. The influence of ϕ at P spreads equally (for constant diffusivity) in all directions. For high Peclet numbers (assumed flow from the node P to E), ϕ at P strongly influences the value of ϕ at the downstream node E. But ϕ at P is weakly influenced by the downstream value. The isolines of ϕ at E are ellipses biased towards the upwind node P. The higher is the Peclet number the closer is the value of ϕ at E to the value of ϕ at P. This property requires that certain sound differencing scheme should be able to detect the flow direction.

(1). Upwind scheme:

The simplest upwind scheme possible is the first-order upwind scheme (assume the positive x direction):

$$\phi_w = \phi_W,\ \phi_e = \phi_P. \tag{3.14}$$

Eq.3.13 becomes:

$$(\mathrm{A}\rho[\vec{u}])_e\phi_P - (\mathrm{A}\rho[\vec{u}])_w\phi_W = (\mathrm{A}\Gamma)_e\frac{\phi_E-\phi_P}{\delta X_{EP}} - (\mathrm{A}\Gamma)_w\frac{\phi_P-\phi_W}{\delta X_{PW}} + S_uV_p + S_pV_p\phi_P. \tag{3.15}$$

It is clear from above that the first-order upwind scheme uses consistent method to calculate convection and diffusion fluxes, so it obeys conservativeness. The coefficients a_W, a_P and a_E for node W, P and E are always positive and if continuity rule is satisfied $a_P = a_E + a_W$ so coefficient matrix is diagonally dominant, so it satisfies the boundedness rule. As the face value is always identical with the grid value upwind, the transportiveness is embedded in it by nature.

From all the properties above it can be concluded that the upwind scheme is unconditional stable, however, it has only first order precision. When applied in the multi-dimensional problems, errors can occur when the flow is not aligned with the grid lines. The resulting error has a diffusion-like appearance and is called false diffusion.

(2). Central-differencing scheme:

Assuming the linear variation of ϕ between P and E or P and W, the face values are fixed as follows:

$$\phi_e = f_x\phi_P + (1-f_x)\,\phi_E, \tag{3.16}$$

$$\phi_w = f_x\phi_P + (1-f_x)\,\phi_W, \tag{3.17}$$

where the interpolation factor f_x is defined as the ration of distance between the corresponding grids. This differencing scheme is called central-differencing scheme. It uses consistent expressions for face flux calculation to ensure conservativeness. The coefficients satisfy the Scarborough criterion.

However, for Peclet number larger than 2 the coefficients are no longer the same sign, thus violates the boundedness requirement. This scheme cannot recognize the direction of flow or the strength of convection relative to diffusion as the face convective and diffusive fluxes are calculated by all directions. So at high Peclet number it will not possess transportiveness.

As this scheme is conditional stable in relation to Peclet number, it will have strict requirement of mesh quality. It is not suitable for general-purpose flow calculations. This shows the need to develop the above two most fundamental schemes to achieve good balance between accuracy and stability. Among them some famous differencing schemes are hybrid, power-law, QUICK and TVD schemes. The hybrid scheme switches between upwind and central-differencing scheme for different Pe values but only possess first-order precision, power-law scheme is similar but more accurate for one-dimensional problems. QUICK scheme is based on a quadratic function and has a third-order accuracy on a uniform mesh, however it cannot guarantee the uniform sign of its coefficients and is conditionally stable. In this scope, to suit the need for calculating complicated physical process described by a set of highly non-linear mathematical equations, the Total Variation Diminishing scheme (TVD) is applied due to the fact that it inherently satisfies all the necessary requirements of transportiveness, conservativeness and boundedness and also ensures good accuracy.

(3). TVD scheme

For a stable, higher-order precise and non-oscillatory scheme, the property of monotonicity preserving is necessary. It will not produce local extrema; the local minimum must not decrease and local maximum not increase. It is shown in Fig.3.1 to illustrate its meaning:

$$\mathrm{TV}(\phi) = |\phi_3 - \phi_1| + |\phi_5 - \phi_3|, \tag{3.18}$$

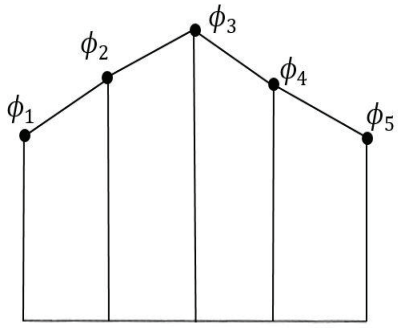

Fig.3.1. A discrete data set for the illustration of total variation

where $\mathrm{TV}(\phi)$ is called total variation of discretized solution, according to Lien et al. [71] this total variation should not increase.

All the monotonicity-preserving schemes have the property that the total variation should diminish with time, hence justify the name TVD. The interpolation method of this scheme generally takes the following form:

$$\phi_e = \phi_P + \frac{1}{2}\Psi(r_e)(\phi_E - \phi_P), \tag{3.19}$$

$$\phi_w = \phi_W + \frac{1}{2}\Psi(r_w)(\phi_P - \phi_W). \tag{3.20}$$

For a classical one-dimensional diffusion-convection problem discussed above, this scheme could be generally implemented as follows:

$$(\mathrm{A}\rho[\vec{u}])_e\left(\phi_P+\frac{1}{2}\Psi(r_e)(\phi_E-\phi_P)\right)-(\mathrm{A}\rho[\vec{u}])_w\left(\phi_W+\frac{1}{2}\Psi(r_w)(\phi_P-\phi_W)\right)$$

$$=(\mathrm{A}\Gamma)_e\frac{\phi_E-\phi_P}{\delta X_{EP}}-(\mathrm{A}\Gamma)_w\frac{\phi_P-\phi_W}{\delta X_{PW}}+S_uV_p+S_pV_p\phi_P, \tag{3.21}$$

where $\Psi(r)$ is called limiter function and r is calculated according to:

$$r_e=\left(\frac{\phi_P-\phi_W}{\phi_E-\phi_P}\right), \tag{3.22}$$

$$r_w=\left(\frac{\phi_W-\phi_{WW}}{\phi_P-\phi_W}\right). \tag{3.23}$$

For first-order upwind scheme this limiter function is simply 0, for central-differencing scheme is 1. However, not all the limiter function satisfies TVD condition. According to Sweby [72], the sufficient preconditions for a scheme to be TVD lie in the r-Ψ relationship:

$$\Psi(r)|x|\leq\begin{cases}2r, & 0<r<1\\ 2, & x\geq 1\end{cases} \tag{3.24}$$

It is clear that the first-order upwind is safely within this region without extra restrictions. According to Sweby, for a TVD scheme to have a second-order precision, there should be another criterium, that is, the flux limiter function should pass through the point (1,1) in the r-Ψ diagram and must be bounded by central-differencing and linear upwind schemes(Fig.3.2).

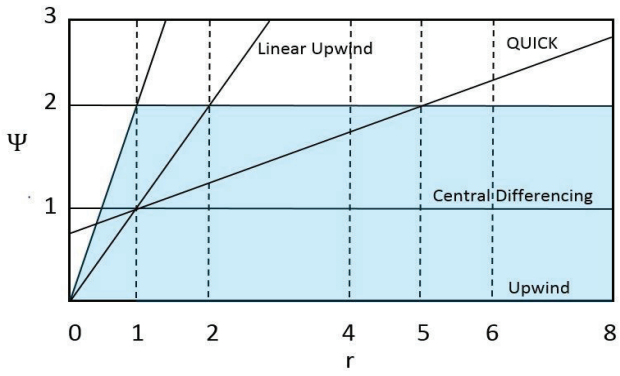

Fig.3.2. r-Ψ diagram

There're actually several limiter functions that satisfy the criterium for a strict TVD scheme, such as Van Leer [73], and Min-Mod [74], SUPERBEE [74]. The limiter function applied in this scope is Sweby's [72] limiter function:

$$\Psi(r)=\max[0,\min(\beta r,1),\min(r,\beta)],\ \beta=\lim_{r\to\infty}\Psi(r). \tag{3.25}$$

This expression is a generalization of Min-Mod and SUPERBEE limiters regulated by the parameter β. If β=1, the function becomes that of Min-Mod and β=2 becomes that of SUPERBEE.

If Eq.3.21 is rearranged into the following form:

$$a_P\phi_P=a_W\phi_W+a_E\phi_E+S_u^{DC}, \tag{3.26}$$

where a_P , a_W, a_E are coefficients that consist of convection and diffusion contents, which are the same with those of first-order upwind scheme. The source term S_u^{DC} is an extra contribution that ensure the final discretization obeys the TVD rule while avoiding the stability problems due to the negative coefficients and is called deferred correction:

$$S_u^{DC} = -(A\rho[\vec{u}])_e\left(\frac{1}{2}\Psi(r_e)(\phi_E-\phi_P)\right)+(A\rho[\vec{u}])_w\left(\frac{1}{2}\Psi(r_w)(\phi_P-\phi_W)\right). \quad (3.27)$$

The central coefficient a_P is (suppose the positive x direction):

$$a_P = a_w + a_E + [(A\rho[\vec{u}])_e - (A\rho[\vec{u}])_w)]. \quad (3.28)$$

The coefficients for neighboring grids give:

$$a_w = \frac{(A\Gamma)_w}{\delta X_{PW}} + \max[(A\rho[\vec{u}])_w, 0], \quad (3.29)$$

$$a_E = \frac{(A\Gamma)_e}{\delta X_{EP}} + \max[-(A\rho[\vec{u}])_e, 0]. \quad (3.30)$$

Although applying TVD schemes can sometimes cost 15% more CPU time than higher-order QUICK scheme according to [71] due to additional calculation overhead by deferred correction, it provides oscillation-free solutions. Besides, in situations such as to capture shock waves the usual strategy is to refine meshes, however it is not economic especially in large scale simulations. And when applying central-differencing, upwind or hybrid scheme on coarser meshes, they always give false shock predictions while TVD schemes are more precise on it, which means such schemes can be put in to general application as they archive good balance between numerical precision and stabilization while do not have high requirement on mesh resolution.

As for the boundary value implementation, for example, if the west neighboring grid ϕ_W doesn't exist, and the value for west face is fixed at ϕ_A, for r_e in the limiter function discussed previously (Eq.3.22) ϕ_W should be replaced by another value ϕ_o to calculate the deferred correction, the mirror node extrapolation by Leonard [75] gives:

$$\phi_o = 2\phi_A - \phi_P. \quad (3.31)$$

Hence:

$$r_e^* = \left(\frac{\phi_P-\phi_o}{\phi_E-\phi_P}\right) = \frac{2(\phi_P-\phi_A)}{\phi_E-\phi_P}. \quad (3.32)$$

3.2 Orthogonality correction

In the previous section, several basic aspects of discretization have been addressed. They are all analyzed based on a simplified one-dimensional, steady state and above all orthogonal problem. However, in practice due to the difficulty in mesh generation for complicated geometry, the cell distribution can hardly be orthogonal. According to the basic principle of Gauss's divergence theorem, the flux that take part in calculation should be normal to the cell faces, if nonorthogonality exists, it will produce conflict in the calculation of inter-cell gradients. Because in non-orthogonal condition, the calculated gradient from the two neighboring cell centers is not align with face normal direction (Fig.3.3). Taking the diffusion flux in a hexahedral cell for example:

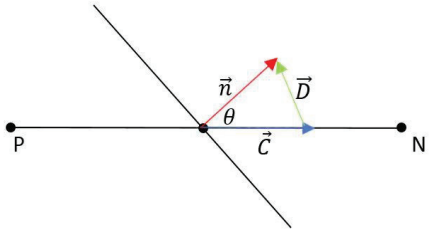

Fig.3.3. Illustration of a nonorthogonal mesh interface

$$\int_{CV}\nabla\cdot(\Gamma\nabla\phi)\mathrm{dV}=\sum_{A1}^{A6}\vec{n}\cdot\mathrm{A}\Gamma\nabla\phi. \tag{3.33}$$

While $\vec{n}$ denotes face normal, $\nabla\phi$ is calculated along P-N line(Fig.), suppose the angle in-between is θ, then:

$$|\vec{n}\cdot\mathrm{A}\Gamma\nabla\phi|=\mathrm{A}\Gamma\cos\theta\left|\frac{\phi_N-\phi_P}{\delta X_{PN}}\right|. \tag{3.34}$$

The usual strategy for it is to decompose $\vec{n}\cdot\mathrm{A}$ into P-N component $\vec{C}$ and non-P-N component $\vec{D}$:

$$\vec{n}\cdot\mathrm{A}=\vec{C}+\vec{D}. \tag{3.35}$$

There are many possible decomposition methods concerning the non-orthogonal treatment (Davidson [76], Mathur et al. [77], Haselbacher [78]). No matter in what way the face normal is decomposed, the correction process can be described as follows:

$$\vec{n}\cdot\mathrm{A}\Gamma(\nabla\phi)_f=\left|\vec{C}\right|\left|\frac{\phi_N-\phi_P}{\delta X_{PN}}\right|+\vec{D}\cdot(\nabla\phi)_f, \tag{3.36}$$

where the face interpolation of $\nabla\phi$ is calculated based on the weighted grid value of gradient according to the distance from the corresponding grid to face center:

$$(\nabla\phi)_f=f_x(\nabla\phi)_P+(1\text{-}f_x)\,(\nabla\phi)_N, \tag{3.37}$$

$$f_x=\frac{\delta X_{fN}}{\delta X_{PN}}. \tag{3.38}$$

Although adding the correction as a source term will secure second-order precision, this process is explicit, unbounded and unsigned, particularly if mesh non-orthogonality is very high (over $90°$), the corrected diffusion may be negative and simulation will be divergent, except for the re-adjustment of mesh quality or simply abandon non-orthogonal correction, OpenFOAM provides a compromising limiting factor α to control numerical stability while addressing meshes with poor quality:

$$\alpha\left|\vec{C}\right|\left|\frac{\phi_N-\phi_P}{\delta X_{PN}}\right|>\vec{D}\cdot(\nabla\phi)_f. \tag{3.39}$$

It is clear from above that the smaller α value is, the less role the non-orthogonal correction will play, hence it retains boundedness on the cost of introducing discretization errors. In OpenFOAM, the value for this factor has slightly different meaning and one should pay special attention to:

$$\alpha=\begin{cases}0, & (uncorrected)\\ 0.333, & (non-orthogonal\ correction\ \leq 0.5 orthogonal\ part)\\ 0.5, & (non-orthogonal\ correction\ \leq orthogonal\ part)\\ 1, & (fully\ corrected)\end{cases} \tag{3.40}$$

3.3 Solution algorithm for iteration

There are serval general issues in CFD that lead in sequence to the final numerical results: building a realistic mathematical equation system to describe physical phenomena, discretizing the space and equation system, implementing boundary conditions. Then it comes to solving the whole transport equation system under the corresponding geometric and interpolation conditions. There are generally two methods used to yield numerical results: direct methods and iterative methods. For a large scaled mesh system and numerous unknown parameters for Multiphysics research in this scope, the present capability of high performance computing cannot afford the calculation beforehand by the first method. As for Gaussian elimination method, N equations with N unknowns can require operations of the order of N^3 and the simultaneous storage of all N^2 coefficients in computer memory. Iterative methods such as Jacobi and Gauss-Seidel have become popular in modern CFD computations as they

are based on the repeated application of a relatively simple algorithm until the final preset convergence criterium is fulfilled. One of its most advantageous property over direct method is that only non-zero coefficients in the coefficient matrix need to be stored in computer memory, which usually take up only a small fraction of it (sparse matrix).

The simplest of the iterative methods for solving a linear system of equation is Jacobi method, considering a system of N equations and N unknowns in matrix form: A·x =b, in algebraic form it gives:

$$\sum_{j=1}^{N} a_{ij} x_j = b_i. \tag{3.41}$$

Within the first iteration the calculation loops from equation 1 to N using the above expression based on a set of guessed initial values. Iterations move forward in this way and they are all based on the results in the previous iteration:

$$x_i^{(k)} = \sum_{\substack{j=1 \\ j \neq i}}^{N} \left(\frac{-a_{ij}}{a_{ii}}\right) x_j^{(k-1)} + \frac{b_i}{a_{ii}} \text{ (i=1,2,3,...N).} \tag{3.42}$$

Once in the k-th iteration the residual of i-th equation $r_i^{(k)}$ reaches under a preset criterium r_{pre} it can be considered as convergent:

$$r_i^{(k)} = b_i - \sum_{j=1}^{N} a_{ij} x_j^{(k)} \leq r_{pre}. \tag{3.43}$$

A more popular iteration algorithm over Jacobi is the Gauss-Seidel method, it has better convergence performance and demands less computer memory as it doesn't require the storage of new estimates. Within one iteration the new unknowns are calculated based on the up-to-date results, in other words, not all the un-knowns need to be applied from the previous iteration:

$$x_i^{(k)} = \sum_{j=1}^{i-1} \left(\frac{-a_{ij}}{a_{ii}}\right) x_j^{(k)} + \sum_{j=i+1}^{N} \left(\frac{-a_{ij}}{a_{ii}}\right) x_j^{(k-1)} + \frac{b_i}{a_{ii}} \text{ ,(i=1,2,3,...N).} \tag{3.44}$$

Through the updated partial unknowns, the iteration converges faster than Jacobi method under the condition that the iteration matrix is diagonally dominant and diagonal coefficients are non-zero.

A similar algorithm but with improved iterative performance to the Gauss-Seidel method is called successive over-relaxation algorithm (SOR) by Yong [79], it has been found that the convergence rate could be improved by the introduction of a so-called relaxation factor ϖ:

$$x_i^{(k)} = \varpi\left[\sum_{j=1}^{i-1} \left(\frac{-a_{ij}}{a_{ii}}\right) x_j^{(k)} + \sum_{j=i+1}^{N} \left(\frac{-a_{ij}}{a_{ii}}\right) x_j^{(k-1)} + \frac{b_i}{a_{ii}}\right] + (1-\varpi)\, x_j^{(k-1)}, \text{ (i=1,2,3,...N)} \tag{3.45}$$

where ϖ>1. However, if the iteration process is less stable or even divergent, chances are that one needs to slow down the process by adjusting ϖ below 1 to establish convergence in a divergent case or speed up the convergence of an overshooting process.

Although the previously mentioned algorithms are advantageous over direct solution method, in some cases when grid spacing is small or mesh is fine, the convergence rates of all of them reduces substantially. For many iterative methods, the number of iterations required to reach a converged solution is linearly proportional to number of nodes in one direction. This is because the information travels only one grid size per iteration. It could be easily found that for a given propagation curve of iteration error vector $\vec{e}$:

$$\vec{e}^{(k)} = \vec{x} - \vec{y}^{(k)}, \tag{3.46}$$

where $\vec{x}$ is the real solution vector, $\vec{y}^{(k)}$ is the solution vector after k iterations.

By refining the grid spacing the frequency of error propagation slows down. While high-frequency errors are easily eliminated with standard linear solvers discussed above, they cannot be removed easily at low frequency. Multigrid methods are designed to exploit these inherent differences of error and use iterations on meshes of different sizes. The basic principle of it is by transforming the smoothed low-frequent errors on original fine meshes into higher frequency errors on meshes of coarser level.

The multigrid method can be generally divided into two categories. The direct manipulation of mesh topology (refining and coarsening) during iterations is called geometric multigrid procedure while another procedure does not re-computes matrix of coefficients for the manipulated mesh level but approximate them as linear combination of coefficients of fine grid equations, which is called algebraic multigrid (AMG). This approach doesn't need any geometric information regarding meshes and can be used to build highly efficient and robust linear solvers for highly anisotropic grids and problems with coefficients of iteration matrix that change rapidly. In OpenFOAM, by giving the keyword "faceAreaPair" or "algebraicPair", both procedures are available through the application of the GAMG solver, which stands for Generalized geometric-algebraic multigrid method. In the scope, the former procedure is applied.

In either of the approaches, a multigrid cycling procedure is based on back and forth iterations on the different mesh hierarchies. Hence, they share the same basic solution strategies:

(1). Fine grid iterations

Here the fine grid means original grid. Actually, apart from starting from the finest level, there are another two different methods that starts from the coarsest and the random level of meshes. These two methods have its own drawbacks. By starting from the coarsest level, although attractive in an adaptive mesh refinement setup, it generates uncertainties in the refinement level and is mesh-dependent. The second method yields extra memory overhead regarding transfer of information between grid levels and do not allow good resolution in complex domains. Hence in OpenFOAM it begins with searching interface information for the finest level. In this step, sufficient iterations are made to eliminate the high-frequency errors while no attempt is made to remove the low-frequency component. Based on the intermediate solution y^h, where h denotes grid spacing, the residual $r^h$is attained according to Eq.3.43, and the error vector $\vec{e}^h$ is attained by several iterations of the following:

$$A^h \cdot \vec{e}^h = r^h, \tag{3.47}$$

where A^h is the coefficient matrix of the finest level.

(2) Restriction

After the finest level calculation is complete, the solution is transferred from the finest level with spacing h into ch, where c>1. This process needs a special algorithm for mesh agglomeration. In OpenFOAM it is given by the class *Foam::pairGAMGAgglomeration::agglomerate*. Since all the information regarding finest-level interfaces are already attained in the previous step, the constant value *faceWeights* that collects *faceAreas* is attained (detailed process could be read from *pairGAMGAgglomeration.C*). Based on *faceWeights* and other inputs by users (such as *mergeLevels* which decides for how often the calculation should be done among agglomerations and *nCellsInCoarsestLevel* which prescribes an approximate mesh size at the coarsest level), the solver starts the agglomeration process, picking up all the necessary data and generating a cluster once a match between two cells are found.

Due to the larger mesh spacing after agglomeration, the low-frequency errors that cannot be eliminated by the previous step is transferred into high-frequency component and are reduced rapidly. In this step, the intermediate solution y^{ch} is not solved. Instead, similar equation like eq. is solved iteratively with an initial guess of e^{ch}=**0**. The coefficients of matrix A^{ch} is calculated according to some form of averaging or interpolation technique based on the fine grid results A^{h}. While another key variable residual r^{h} can also be calculated in the similar way. The cost per iteration is greatly reduced due to the number of cells that take part in calculation, which allows more number of iterations to get a converged solution of error vector e^{ch}.

(3) Prolongation

After the coarsest level is reached and restriction process is complete, the prolongation process is used to transfer the error correction from coarse level back to the original finest level. As GAMG solver applies V-cycle, which is a simple cycle that contains no more restriction process during prolongation. Linear interpolation or any other interpolation scheme could be used to construct the prolonged error values of fine grid e'^{ch} from coarse grid errors (for example e'^{2h} can be attained from e^{4h}). The prolonged error e'^{ch} can be now applied to correct the error attained at the same mesh level in the previous restriction process:

$$e^{ch}_{corrected} = e^{ch} + e'^{ch}. \tag{3.48}$$

To reduce the side-effect error brought by the linear interpolation during level-transfer, it is usually necessary to do the smoothing process to reduce high-frequency error before moving forward to the next level, OpenFOAM provide users with the following smoothers (detailed coding can be seen in the directory *OpenFOAM-2.3.x / src / OpenFOAM / matrices / lduMatrix/smoothers /*):

DIC: Simplified diagonal-based incomplete Cholesky smoother for symmetric matrices.

DICGaussSeidel: Combined DIC/GaussSeidel smoother for symmetric matrices in which DIC smoothing is followed by GaussSeidel to ensure that any "spikes" created by the DIC sweeps are smoothed-out.

DILU: Simplified diagonal-based incomplete LU smoother for asymmetric matrices.

DILUGaussSeidel: Combined DILU/GaussSeidel smoother for asymmetric matrices in which DILU smoothing is followed by GaussSeidel to ensure that any "spikes" created by the DILU sweeps are smoothed-out.

GaussSeidel: Discussed at the beginning of section 3.3.

nonBlockingGaussSeidel: Variant of gaussSeidelSmoother that expects processor boundary cells to be sorted last and so can block later. Only when the cells are actually visited does it need the results to be present. It is expected that there is little benefit to be gained from doing this on a patch by patch basis since the number of processor interfaces is quite small and the overhead of checking whether a processor interface is finished might be quite high (call into mpi). Also this would require a dynamic memory allocation to store the state of the outstanding requests.

symGaussSeidel: A lduMatrix::smoother for symmetric Gauss-Seidel.

(4) Correction and final iterations

After the prolong-corrected and smoothed error of the finest level $e^{h}_{smoothed}$ is attained, it will be used finally to yield the corrected solution after multigrid process based on the fine grid results:

$$y_{corrected} = y^{h} + e^{h}_{smoothed}. \tag{3.49}$$

Although the results attained from above cannot be the real analytical solution due to multiple interpolation processes, this multigrid approach has been proved to be fast and effective over Gauss-Seidel method. It is among the fastest solution techniques known today. In contrast to other methods, multigrid methods are general in that they can treat arbitrary regions and boundary conditions. They do not depend on the separability of the equations or other special properties of the equation. Its advantages in convergence rates could be more attractive when solving large scaled problems with complex physical descriptions as researched in this study.

Apart from the linear solvers discussed above, OpenFOAM also provides the users with the possibility to use a wide variety of solvers that could be potentially useful in finding a balance between the convergence rates and numerical stability of different discretized equations, such as smoothsolver(Iterative solver for symmetric and assymetric matrices which uses a run-time selected smoother e.g. GaussSeidel to converge the solution to the required tolerance.) and PCG solver (Preconditioned conjugate gradient solver for symmetric lduMatrices using a run-time selectable preconditioner.), while preconditioning is a feature that could be add to the iteration process to accelerate convergence rate as using a preconditioner contributes to a faster propagation of information through the computational mesh provided that the approximation of matrix of coefficient is easily invertible and all operations with that are computational cheap.

3.4 The compressible PISO Algorithm

In previous sections, it is assumed that velocity field is known beforehand, however it is impossible to predict velocity field without the coupled calculation with other variables. From Navier-Stokes equations it is clear that every velocity component appears in every momentum equation and continuity equation, making variables highly coupled with each other. Besides, the pressure gradient term is the main momentum source term, but there's no transport equation for pressure. Usually the equation system is closed by the perfect gas law to yield pressure field. Due to the complexity of non-linearities in the coupled equation system, it is necessary to apply an efficient pressure-velocity calculation procedure that saves computation resource and meets the need of precision and stability. In OpenFOAM, SIMPLE and PISO algorithms are coded as standard velocity-pressure coupling procedures for steady-state and transient solvers respectively. The former stands for Semi-Implicit Method for Pressure Linked Equations and is relatively straightforward due to only one momentum corrector step. This is, however, satisfactory for correcting velocities but not for pressures, whereas PISO (Pressure Implicit with Splitting of Operators) proposed by Issa [80] has a further corrector step in which no terms are omitted to derive the discretized pressure equation, which shows robust convergence behavior and required less computational effort. The algorithm per iteration/time step could be summarized as follows:

(1) Solve the intermediate velocity $\boldsymbol{u}^*$ with an initial guess of pressure $\boldsymbol{p}^*$

To simplify the description, here suppose a one-dimensional flow problem with positive x direction:

$$a_P u_p^* = \sum a_{nb} u_{nb}^* + (p_W^* - p_P^*) A_P + b_p, \tag{3.50}$$

where A_P is the cell face area of control volume "nb" denotes neighbor cell, b_p is the momentum source term.

(2) Establish the first pressure correction equation

Defining the first pressure correction p' as the difference between the intermediate pressure p^{**} and the guessed field p^*:

$$p^{**} = p^* + p'. \tag{3.51}$$

The corresponding relation for velocity can be defined similarly:

$$u^{**}=u^{*}+u'. \tag{3.52}$$

As for the values of u^{**} and p^{**}, they also satisfy the relation like Eq.3.50:

$$a_P u_p^{**}=\sum a_{nb} u_{nb}^{**}+(p_W^{**} - p_P^{**})A_P+b_p. \tag{3.53}$$

Subtracting Eq.3.50 from Eq. 3.53 gives the relation of velocity and pressure corrections:

$$a_P u_p'=\sum a_{nb} u_{nb}'+(p_W' - p_P')A_P. \tag{3.54}$$

In the first corrector step, the first term of R.H.S. in Eq.3.54 is dropped to simplify the velocity corrections, which is the same as SIMPLE algorithm. Hence:

$$u_p'=\frac{A_P}{a_P}(p_W' - p_P'). \tag{3.55}$$

The intermediate velocity u^{**} can be attained by combining Eq.3.52 and Eq.3.55:

$$u_P^{**} =u_P^{*}+\frac{A_P}{a_P}(p_W' - p_P'). \tag{3.56}$$

The velocity field is also subject to the constraint that it should satisfy the continuity equation, substituting the velocity expression above into the discretized continuity equation:

$$(\rho A)_e(u_e^{*}+\frac{A_e}{a_e}(p_P' - p_E'))- (\rho A)_w(u_w^{*}+\frac{A_w}{a_w}(p_W' - p_P'))=0. \tag{3.57}$$

After rearrangement of the equation above, it yields the pressure correction equation:

$$a_P p_P'=a_E p_E'+a_W p_W'+b', \tag{3.58}$$

where

$$a_P= a_E+ a_W, \tag{3.59}$$

$$a_E= (\rho A)_e \frac{A_e}{a_e}, \tag{3.60}$$

$$a_W= (\rho A)_w \frac{A_w}{a_w}, \tag{3.61}$$

$$b'= (\rho u^{*} A)_w-(\rho u^{*} A)_e. \tag{3.62}$$

Once the first pressure correction $p'$from the equation above is attained everywhere, it can be drawn back to correct pressure and velocity to yield $p^{**}$and u^{**}.

(3) Establish the second pressure correction equation

The omission of terms $\sum a_{nb} u_{nb}'$ in the first corrector step will not affect the final solution, but will sometimes cause over-correction of pressure which leads to divergence. Therefore, PISO performs a second corrector step. This will need the pressure and velocity results attained from the last step (p^{**}, u^{**}). The discretized momentum equations for the final correct velocity u^{***} gives:

$$a_P u_p^{***}=\sum a_{nb} u_{nb}^{**}+(p_W^{***} - p_P^{***})A_P+b_p. \tag{3.63}$$

Substracting Eq. 3.53 from the equation above with the exception that u_{nb}^{**} is replaced by u_{nb}^{*} yields:

$$u_p^{***}= u_p^{**}+\frac{\sum a_{nb}(u_{nb}^{**}-u_{nb}^{*})}{a_P}+\frac{A_P}{a_P}(p_W'' - p_P''), \tag{3.64}$$

where the second pressure correction p'' has the following relation:

$$p^{***}=p^{**}+p''. \tag{3.65}$$

Substitution of u^{***} into discretized continuity equation, the second pressure correction equation gives:

$$a_P p_P''=a_E p_E''+a_W p_W''+b'', \tag{3.66}$$

where $b'' = \left(\frac{\rho A}{a}\right)_e \sum a_{nb}(u_{nb}^{**} - u_{nb}^{*})- \left(\frac{\rho A}{a}\right)_w \sum a_{nb}(u_{nb}^{**} - u_{nb}^{*})$.

Eq.3.66 is solved to obtain p'', as a result the twice-corrected pressure p^{***} can be obtained:

$$p^{**}=p^{*}+p'+p''. \tag{3.67}$$

For transient version of PISO, it is generally the same as steady-state version, with minor corrections regarding time discretization (e.g. b' and b'' should be added by the term $(\rho_P^0 - \rho_P)\Delta V/\Delta t$). The transient version is different from stationary version due to its non-iterative property. Because the pressure and velocity results within a single PISO loop by a suitably small time step are accurate enough to proceed to the next time step, which will spare a lot of computation time. If the time step to maintain a stable simulation is sometimes too small to be economic, using under-relaxation factor may be a good choice to avoid divergence. Peric [81] suggested the under-relaxation factor for pressure and velocity to be 0.2 and 0.8 respectively based on the expected behavior of the second corrector step within the PISO algorithm.

3.5 Parallel computing

Using computationally efficient solution procedures discussed above will generally save a lot of computation resource while maintaining precision. However, it is still not realistic to perform the transient coupled plasma-electrode simulation on a common personal laptop or desktop especially when solving large-scaled 3D systems. The main reason is that, apart from the complexity of transport equations, approximation of transport properties, which usually relies on local particle composition and degree of thermal nonequilibrium, or the specific mesh size, the numerical simulation cannot have a stable start if the full value of electric current is implemented directly on the initial cold plasma (in this scope the initial temperature is set 5000K for electron temperature). This is due to the omission of all the essential discharge periods before arc discharge plays its role (see section 1.1.2), which is not within the research interest in this scope. A practical strategy to avoid enormous amount of joule heating at the beginning period which could lead to instant divergence is to apply a ramp input electric current that raises its value at an acceptable pace till the full value is reached. This is favorable of both numerical stability and physical reality as the emission current from cathode should obey Richardson law, which rises also gradually according to the surface temperature. The duration of whole ramp process is basically proportional to the magnitude of simulated current density. In this study, after the stability test, the whole ramp duration is set for the first 0.01s with a time step of less than 1×10^{-8}s. The convergence is only achievable within the simulation time after the full value of electric current is reached. As a result, to get the intended convergence results within a reasonable waiting time, parallel computing is the only possible choice. All the simulation results presented in this dissertation are granted by the supercomputing resource provided by HLRN (Der Norddeutshce Verbund für Hoch- und Höchstleistungsrechnen).

Parallel computing is defined as simultaneous use of more than one processor to execute a program. In OpenFOAM the total meshes and fields are decomposed into a selected number of parts, which are then assigned to different processors. The parallel running uses the public domain openMPI implementation of the standard message passing interface by default. The mesh and fields are decomposed using *decomposePar* utility. The total execution time could be remarkably reduced by

decomposing meshes into moderate number of parts. However, the exact reduction of computing time would not be in accordance with the linear growth of the number of participating processors, because data within each processor need to be exchanged with other processors now and then, which is not parallelizable. This data exchange takes place using different methods depending on the type of parallel computer used. Usually, there's an optimal dividing number n_{pm} for each problem to achieve the maximal speed-up. A classical method to evaluate parallel computing speedup η_s is given by the Amdahl's law:

$$\eta_s = \frac{T}{t_s + t_o + \frac{t_p}{n_p}}, \tag{3.68}$$

where n_p is the number of processors, t_s, t_p are the serial and parallel runtime component, t_o is the extra runtime caused by data communication and synchronization between processors, this component grows with the increase of applied number of processers, which occupies an important part of the whole run time if n_p is too large. It suggests that a further increase after n_{pm} is meaningless. For the different regimes of simulations to be presented later (with and without sheath model), n_{pm} is also chosen differently to achieve maximal speedup.

3.6 Analysis of errors and uncertainties

Compared to plasma physics especially the non-thermal plasma physics, which contains a series of strict mathematical descriptions of the related physical phenomena and a lot of aspects that still need deep digging and discoveries, CFD is something more like a circle of uncertainty that puts more weight on the simple fulfilment of some criterium on each computation unit that has been already set with experience and is then also validated by the analytical or experimental data which are also based on simplified assumptions or certain degree of measurement error. Besides, it is highly restricted by the available computing resource that forces the users to give up the precision of the problem and only get compromised results. Therefore, we cannot evaluate the application of CFD with the comment true or false but with the level of confidence in its results. To address the issue of trust and confidence in CFD one has to develop a systematic process that can review the factors influencing simulation results.

Basically, there are two main kinds of factors that decide if the attained numerical results have the desired level of confidence, namely error and uncertainty. According to its definition, error means a recognizable deficiency in a CFD model that is not caused by lack of knowledge. Except for some man-made errors which are due to the carelessness of software users and developers, such as coding errors. There are usually three kinds of numerical errors which are inherent inside the CFD technique that can only be dealt with prudence:

(1) Round-off error

The first kind of numerical error can be called round-off error. It is the difference between an approximation of a number used in computation and its exact (correct) value. In certain types of computation, roundoff error can be magnified as any initial errors are carried through one or more intermediate steps. A notorious example is the fate of the Ariane rocket launched on June 4, 1996 (European Space Agency 1996). In the 37th second of flight, the inertial reference system attempted to convert a 64-bit floating-point number to a 16-bit number, but instead triggered an overflow error which was interpreted by the guidance system as flight data, causing the rocket to veer off course and be destroyed. Since such kind of error is easy to accumulate, it needs to be controlled by careful arrangement of floating-point arithmetic operations to avoid subtraction of most equal sized large numbers or addition of numbers with very large difference in magnitude, for example, in CFD

computations it is common to use gauge pressure relative to a specified base pressure when the pressure values within the domain are the same order as the pressure difference between adjacent mesh cells. In this scope, a good example of dealing with round-off error is the storage of particle number density, since the values of them reach sometimes up to $10^{25}/m^3$, which is clearly outside the range of maximal significant figures that can be stored by the program. To reduce such error, all the species computed in this scope are scaled by the total number of particles to yield the specific concentration, or it can be scaled by Avogadro number done by Shirvan et al. [27].

(2) Discretization error

The second kind of numerical error comes from the discretization error, as is already discussed, the linearization of the integration of transport equations need the assumption of linear variation between face values (for example between the value of east face center and the west face center), thus the integration of divergence can be discretized onto each face according to Gauss' theorem with second order accuracy. Besides, the face values used to integrate within the cell are also results of neighboring cell center values with certain interpolation scheme, for example the second-order accurate TVD scheme used in this scope. So in order to linearize equations onto meshes for simulation, it is always necessary to truncate the endless Taylor series to some extent to suit the computation capacity in reality. This truncation operation leaves a tough task for users, because the order of discretization error lies on the hand of mesh resolution, the finer the mesh the better the results. However, by setting the mesh spacing small will increase the use of computation resource, therefore one needs always the procedure of mesh-dependency test before embarking on the subsequent parameter studies to decide the most economic mesh resolution.

(3) Iteration truncation error

The third kind is namely the iteration truncation error. As there's rarely the possibility to get the real solution, especially for the lots of non-linear transport equations to be calculated in this scope, the iterative solution procedure is applied here. One always needs to preset the convergence criterium to regulate the results into an acceptable order of precision before iteration procedure stops. The local and global residual should take the absolute form of Eq.3.46, as in this study, for the purpose of simulating plasma-electrode interaction, the coded solver is based on the implementation of transport equations onto the default solver *ChtMultiRegionFoam*, which is a typical pressure-based solver. This kind of solver doesn't solve the continuity equation directly, but yield the related value based on the perfect gas law and the subsequent pressure-velocity correction (PISO). So for this kind of solver the users often need to struggle with the convergence problems of continuity. It is highly possible that if one calculates the integration of density difference between the densities before and after pressure correction directly, sometimes it will feed back a perfect "0 error" result that makes us happy. However, it naturally doesn't mean the problem is converged but is actually the offset of positive and negative continuity errors. Defining the global residual $\left(R^{\phi}\right)^{(k)}$ as the sum of absolute values of local residuals over all M control volumes with the computational domain after k iterations:

$$\left(R^{\phi}\right)^{(k)} = \sum_{i=1}^{M} \left| \left(\sum_{nb} a_{nb}\phi_{nb}\right)^{(k)} + b_i^{(k)} - \left(a_P\phi_P\right)_i^{(k)} \right|. \tag{3.69}$$

However, this alone cannot offer a reasonable judgment as for an acceptable convergence especially when the variable ϕ itself is large. There's always the need to normalize this residual for us to consider if the residual is small enough:

$$\left(R_N^{\phi}\right)^{(k)} = \left(R^{\phi}\right)^{(k)} / F_R^{\phi}, \tag{3.70}$$

where $\left(R_N^{\phi}\right)^{(k)}$ is the normalized global residual for variable ϕ, F_R^{ϕ} is the normalization factor. There're several common methods to normalize the residual, for example, one can take its own size as a normalization factor or the total rate of convective flow $(\rho A\vec{u}\cdot\vec{n})\phi$. In OpenFOAM, for evaluating the truncation error of continuity, the total mass of the whole computation domain is used as the normalization factor according to coding in *continuityErrs.H*.

(4) Other possible errors and uncertainties

The discussions above are all about the possible error sources that due solely to the level of solution procedures relating to finite volume method, which is only a bridge built between the physical reality and numerical descriptions. The nearer one needs its results to the physical reality, the more sophisticated physical models used in the simulation should be available. This force every simulation engineer to have a deep insight into the degree of the physical model precision. But this doesn't mean that to model plasma discharge correctly, one needs the most detailed physical model of every aspect with every detailed parameter being exactly the same with what's confirmed by the experiments. Because there're still a lot of aspects that cannot be well understood or measured by researchers till now and the aspects are simply too numerous to be concluded within one research thesis. The model precision here means the correct use of physical common sense and simplification within an acceptable error range to suit the specific research topic granted by limited computation resource. For example, the main contribution of this study is to apply an effective value for sheath conductivity, which is based on a global quasi-neutrality assumption including the sheath to achieve a stable T_e calculation in this scope. Although Child's law takes part in the calculation, the real charge separation process cannot be described by our model. Nevertheless, the model will still hold acceptable validity as the dimension of sheath layer is ignorable compared with the main discharge region.

Other possible error sources may come from the neglection of electrode melting and evaporation, which are not within the functionality of *ChtMultiRegionFoam* as the mesh interfaces cannot be changed with time or iteration. The validity can still be guaranteed if metal erosion and evaporation is not dominant enough to play an important role in modifying the plasma electrical conductivity and local thermal radiation. Besides, for the simplification of number of species taking part in chemical nonequilibrium calculation, the excited heavy species are not treated separately, and only first excited argon is included in reaction rate model. There's thus more or less the possibility to deviate from reality if other excited states are prevailing in the discharge process, which leads to inaccurate electron number densities. In the next chapters, the level of confidence addressed to the interaction model in this scope with all these potential error sources will be checked with available analytical and experimental results.

While numerical and model errors can be evaluated, adjusted and minimized within an acceptable range, uncertainties such as input uncertainty is sometimes more difficulty to handle. The first kind of input uncertainty comes from the domain geometry which involves the specification of the shape and size of the region of interest. On one hand, it is impossible to manufacture the idealized discharging device perfectly to design specifications, manufacturing tolerance will lead to discrepancies between design intention and the actual manufactured devices. On the other hand, the construction of a CAD model which is converted from the design intention, is always based on the idealization of real operation. This kind of idealization will lead to further input uncertainty. For example, the geometric irregularities of cathode tip resulted from melting in the discharge process is simply represented by a standard cone in most CFD applications, as the real shape during and after operation and the roughness of electrode surface to be used in turbulence boundary conditions are always hard to predict.

The second kind of input uncertainty comes from the boundary conditions. Even if a lot of physical phenomena are included in the plasma-electrode interface, such as ion bombardment heating, thermionic emission cooling and secondary emission, it is still difficult to account for all the aspects at this place to a high degree of accuracy, some collective electron emission process at the interface such as ion-enhanced thermal-field emission or secondary emission induced by metastable atoms [60] also needs to be taken into account in some circumstances. What's more, the non-slip boundary condition for velocity at solid wall is for most situations acceptable, however, for the dilute plasma sheath, there will be discrepancy with this boundary condition if the sheath potential drop is high enough so that ions that reach cathode surface will be much fewer than those at the sheath outer edge.

The third kind of uncertainties in this scope originates from the predefinition of plasma transport property calculation. The temperature and θ-dependent values of electrical conductivities used in this scope or as in some literatures such as Boie [40] and Trelles [42] are based on the constant pressure assumption in favor of economic CFD computation. However, errors will be introduced if they are applied throughout the whole domain, especially at the high temperature plasma core, where pressure is elevated due to intensive joule heating and pinch effect. On the other hand, even if the pressure factor can be included into the transport properties regardless of its difficulty, the model using Chapman-Enskog theory can only provide approximated results if we only use equilibrium composition to calculate.

Chapter 4

Model validations

In chapter 2 and 3 the applied mathematical model and solution methods as well as the possible sources of errors and uncertainties have been discussed. To check the level of confidence, it is necessary to make the numerical results attained by the model to be compared to the available analytical or experimental results under different operation conditions. In this chapter, three simple simulations are performed with a step by step validity check aiming at magnetic field, flow velocity, solid/fluid temperatures, electrical potential and so on.

4.1 Magnetic field validation

Firstly, it is necessary to check out the validity of magnetic vector potential field at electrode interface. According to Eq.2.124, the field $\vec{A}$ should be continuous at this place. A special boundary condition is implemented in this scope based on a third-party software *GroovyBC*, it ensures the internal fields at interface boundary cells are consistent with the values on the other side. Wedge boundary condition is applied on both front and back surfaces for 2D axisymmetric case here(Fig.4.1). To check the numerical confidence, two sets of boundary conditions (Table.4.1 and 4.3) and initial values (Table.4.2 and 4.4) are applied for reference:

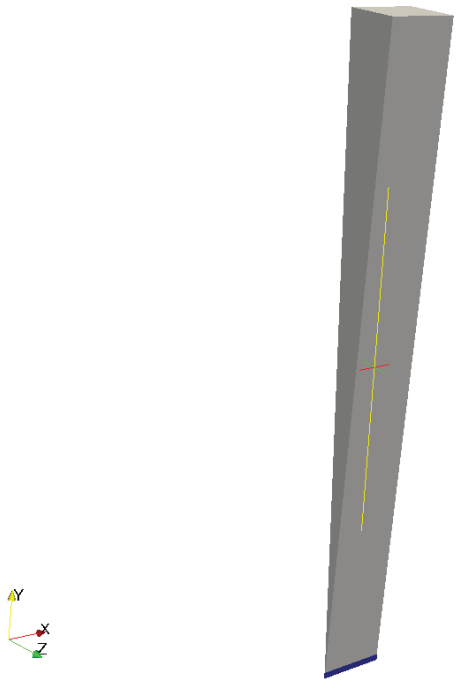

Fig.4.1. Illustration of 2D axisymmetric geometry intended for the simulation of coupled magnetic field (grey region represents fluid region, dark blue in the bottom is the sold region)

Table.4.1. Boundary conditions for case 1

Variables / Boundaries	$\vec{A}$(Vs/m)	φ(V)
GasFrontAndBack	Wedge	Wedge
GasLeft	zeroGradient	zeroGradient
GasRight	zeroGradient	zeroGradient
GasTop	(0,0,0)	0
Interface	Coupled(GroovyBC)	Coupled(OpenFOAM)
SolidLeft	zeroGradient	300
SolidRight	zeroGradient	0
SolidFrontAndBack	Wedge	Wedge

Table.4.2. Initial values for case 1

Variables / Regions	μ_m(H/m)	σ(S/m)
Gas	1.257×10^{-6}	1×10^{-5}
Solid	1.257×10^{-6}	10^{4}

Table.4.3. Boundary conditions for case 2

Variables / Boundaries	$\vec{A}$(Vs/m)	φ(V)
GasFrontAndBack	Wedge	Wedge
GasLeft	zeroGradient	zeroGradient
GasRight	zeroGradient	zeroGradient
GasTop	(0,0,0)	0
Interface	Coupled(GroovyBC)	Coupled(OpenFOAM)
SolidLeft	zeroGradient	200
SolidRight	zeroGradient	0
SolidFrontAndBack	Wedge	Wedge

Table.4.4. Initial values for case 2

Variables / Regions	μ_m(H/m)	σ(S/m)
Gas	1.257×10^{-6}	1×10^{-5}
Solid	1.257×10^{-6}	10^{3}

To get the analytical results, it is important to look through the Ampère's circuital law (Eq.2.32), in this case only points to z direction:

$$2\pi y B_z=\mu_m I_{enc}. \tag{4.1}$$

$$B_z=\begin{cases}\frac{\mu_m J y}{2}, & y<R\\ \frac{\mu_m J R^2}{2y}, & y\geq R\end{cases} \tag{4.2}$$

where I_{enc} is the current intensity enclosed by Ampère's circle, J is the magnitude of current density, R is the radius of solid wire.

According to Eq.2.35 and the definition of rotation of a vector field, as well as the fact that B has only z component in this case:

$$B_z = -\frac{\partial A_x}{\partial y}. \tag{4.3}$$

Hence:

$$A_x = \begin{cases} A_x(0) - \frac{\mu_m J y^2}{4}, & y < R \\ A_x(0) - \frac{\mu_m J R^2}{2}\left[0.5 + \ln\left(\frac{y}{R}\right)\right], & y \geq R \end{cases}, \tag{4.4}$$

where the constant $A_x(0)$ is the value of A_x at y=0, this value may vary from case to case. However, due to the limited computation resource, the height of computation domain cannot be infinitely high. The constraint of top face value by (0,0,0) will introduce some error but will not affect the final results if the height of domain is proper. In this case, the height is set 0.1m. So $A_x(0)$ gives:

$$A_x(0) = \frac{\mu_m J R^2}{2}\left[0.5 + \ln\left(\frac{0.1}{R}\right)\right]. \tag{4.5}$$

For case 1 and 2 the values are 9.625×10^{-4} and 6.417×10^{-5} respectively.

The simulated results of A_x and B_z of both cases are shown from Fig.4.2 to Fig.4.7. In general, a very good agreement between numerical and analytical results has been achieved. The B_z results at the center of electric wire cannot reach 0 exactly and has minor numerical deviation. On one hand, it is due to the constraint of top face value by (0,0,0) discussed above. On the other hand, it is due to the fact that the center of boundary cell is not located right on the axis. When using this coupled boundary condition provided by *GroovyBC,* it is important to note that it is very grid-sensitive, if the height of boundary cells from both sides cannot be the same, it will give unrealistic results.

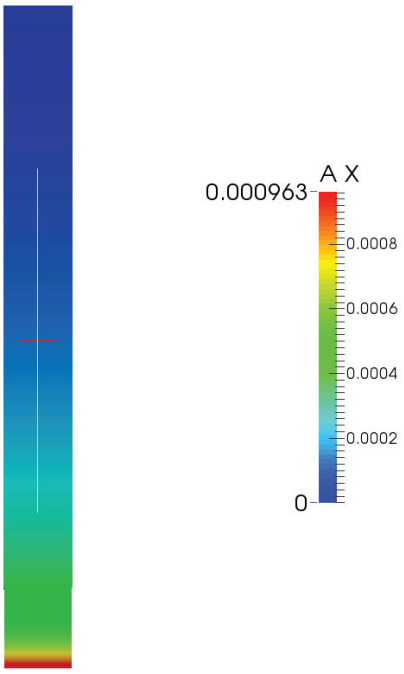

Fig.4.2. Simulated results of A_x from case 1

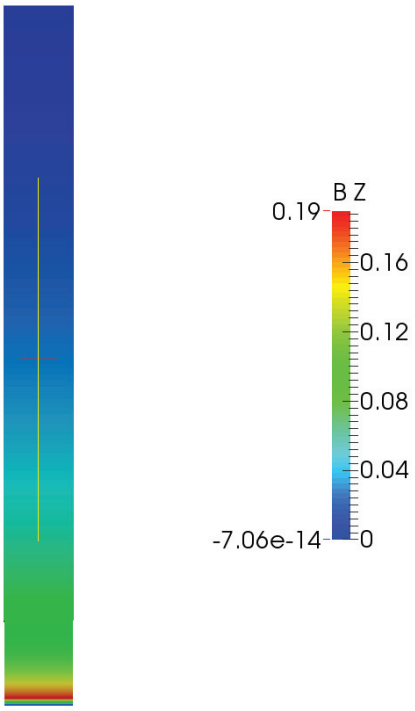

Fig.4.3. Simulated results of B_z from case 1

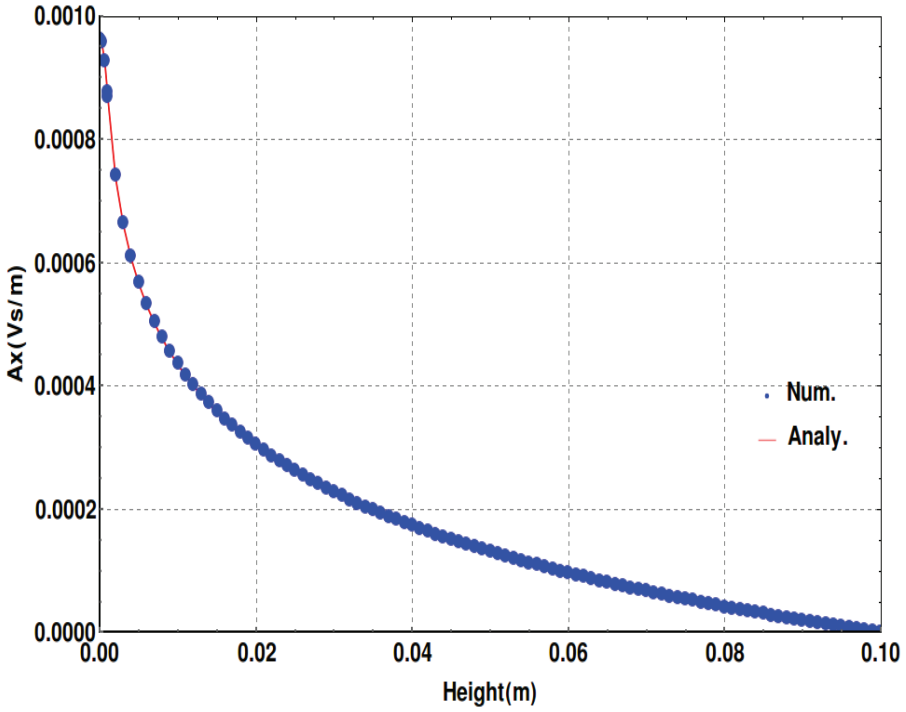

Fig.4.4. Simulated results of A_x from case 1 in comparison with analytical solutions along the vertical cross section

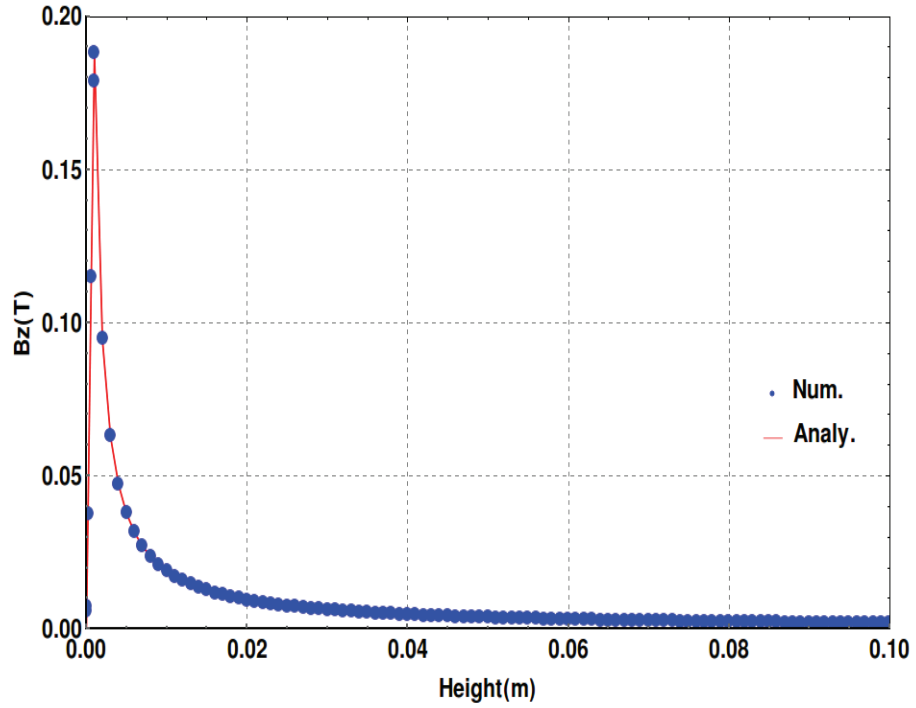

Fig.4.5. Simulated results of B_z from case 1 in comparison with analytical solutions along the vertical cross section

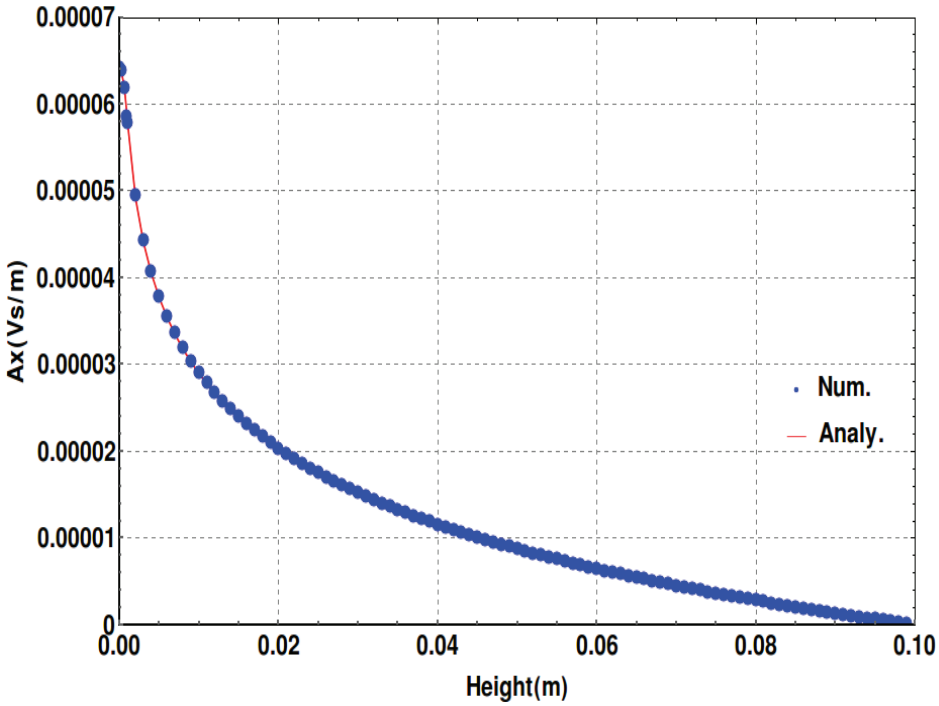

Fig.4.6. Simulated results of A_x from case 2 in comparison with analytical solutions along the vertical cross section

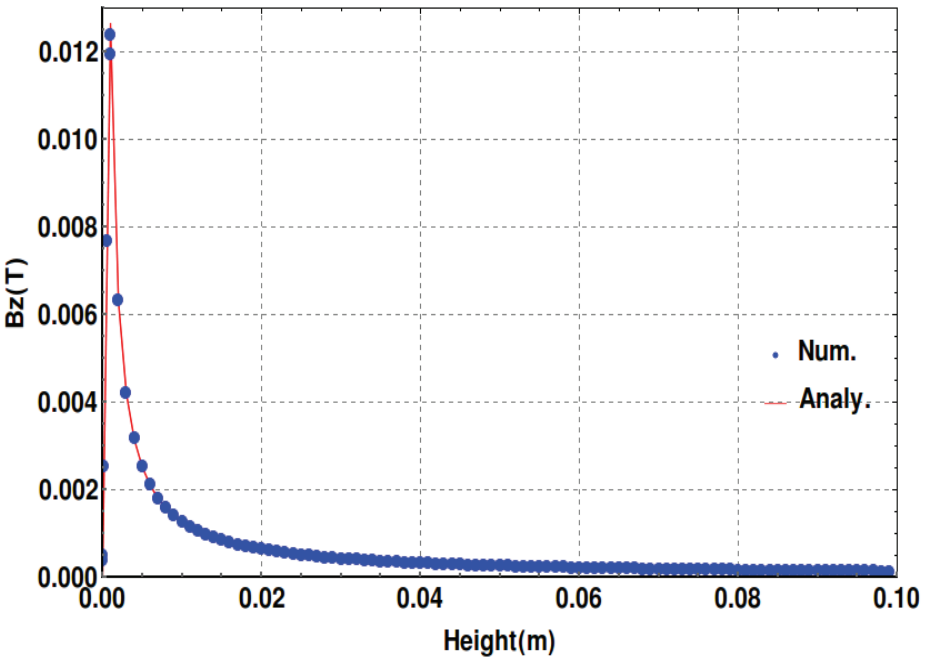

Fig.4.7. Simulated results of B_z from case 2 in comparison with analytical solutions along the vertical cross section

4.2 Flow field validation

In the previous section, the magnetic field of a fluid-solid coupled system under the frozen flow regime is validated. There's also the necessity in this scope to check our numerical confidence in the flowing regime of electrically conducting and viscous fluid. Hartmann flow provides the simulation model with the good opportunity to be checked by its benchmark results due to its simple configuration. Basically, Hartmann flow is characterized by 3 dimensionless parameters: (1) the Hartmann number H_a, which is the ratio of electromagnetic force to the viscous force first introduced by Hartmann [82]:

$$H_a = \mathrm{BL}\sqrt{\frac{\sigma}{\mu}}. \tag{4.6}$$

where B is the magnetic field perpendicular to flow direction, L is the characteristic length scale, σ is the fluid electrical conductivity, μ is the dynamic viscosity. (2) The Reynolds number, which is the ratio of inertial forces to viscous forces within a fluid. (3) The magnetic Reynolds number, which gives an estimate of the relative effects of advection of a magnetic field by the motion of a conducting medium, often a fluid, to magnetic diffusion.

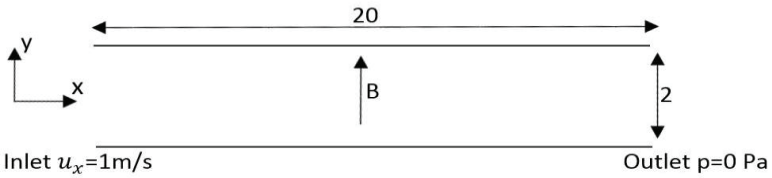

Fig.4.8. Illustration of geometry and boundary conditions for the Hartmann flow simulation

For simplicity, Hartmann problem in this scope is restricted into a steady-state,2D and incompressible channel flow (Fig.4.8). The half of channel width L is set 1m, the length along the flow direction 20m. ρ,μ and σ all have the value of 1. The initiated velocity and pressure inside the channel is 0m/s and 100 Pa. The temperature value of heavy species and electrons is of little significance, so they are both set at T_0= 500K. The magnetic field has the only component along the perpendicular direction (in this scope the positive y direction), and for validation three different values B_y=1,5,50T is predefined. According to Shercliff [83], the transverse flow velocity has the following analytical solution:

$$u_x = u_0 \frac{coshH_a - \cosh(H_a * y/L)}{coshH_a - (sinhH_a)/H_a}, \tag{4.7}$$

where u_0 is the averaged flow velocity of cross section. The detailed boundary conditions defined for the simulation are shown in Table.4.5. As for the 2D assumption, the front and back boundaries are given by the entry *empty* in OpenFOAM. The simulated velocity results along the channel length u_x and at the middle cross section are presented in Fig.4.9 to Fig.4.14 along with comparison with analytical results obtained from Eq. 4.7. It yields very good agreements in all the three test cases with different perpendicular magnetic fields.

Table.4.5. Boundary conditions of the Hartmann flow simulation

Variables / Boundaries	P	$\vec{u}$	T_h	T_e	φ	$\vec{A}$
Inlet	$\frac{\partial p}{\partial n}$=0	(1,0,0)	T_0	T_0	0	A_x=A_z=0, $\frac{\partial A_y}{\partial n}$=-$B_y$
Outlet	0	$\frac{\partial \vec{u}}{\partial n}$=**0**	T_0	T_0	0	A_x=A_z=0, $\frac{\partial A_y}{\partial n}$=-$B_y$
Top	$\frac{\partial p}{\partial n}$=0	(0,0,0)	T_0	T_0	$\frac{\partial \varphi}{\partial n}$=0	A_x=A_z=0, $\frac{\partial A_y}{\partial n}$=0
Bottom	$\frac{\partial p}{\partial n}$=0	(0,0,0)	T_0	T_0	$\frac{\partial \varphi}{\partial n}$=0	A_x=A_z=0, $\frac{\partial A_y}{\partial n}$=0

Fig.4.9. Flow velocity results with B_y =1T

Fig.4.10. Flow velocity results with B_y =5T

Fig.4.11. Flow velocity results with B_y =50T

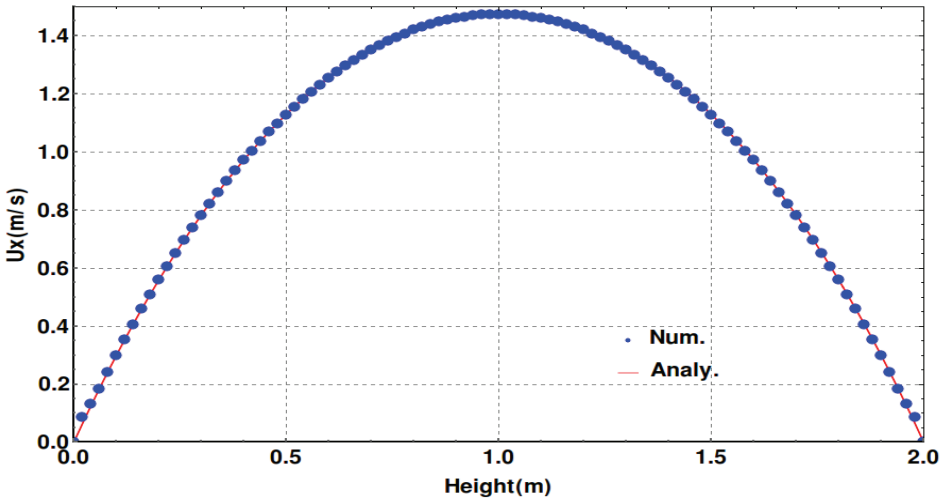

Fig.4.12. Flow velocity results in comparison with analytical solutions with B_y =1T

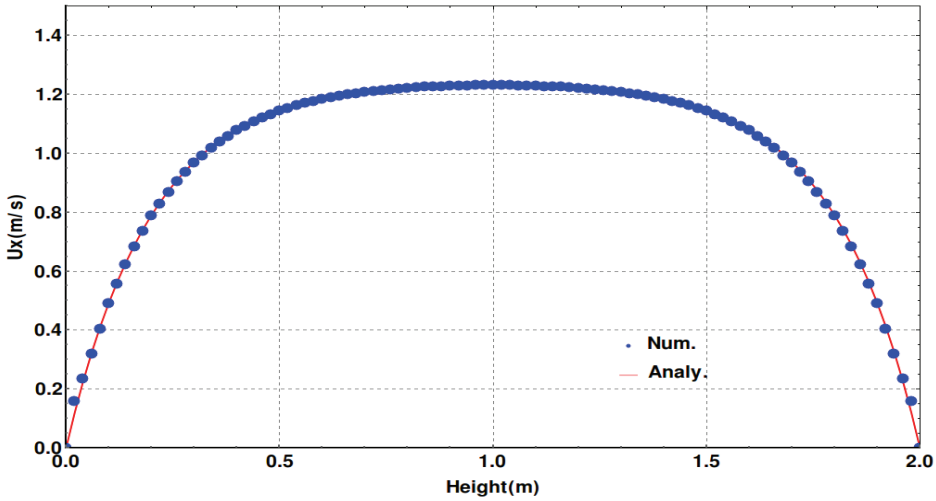

Fig.4.13. Flow velocity results in comparison with analytical solutions with B_y =5T

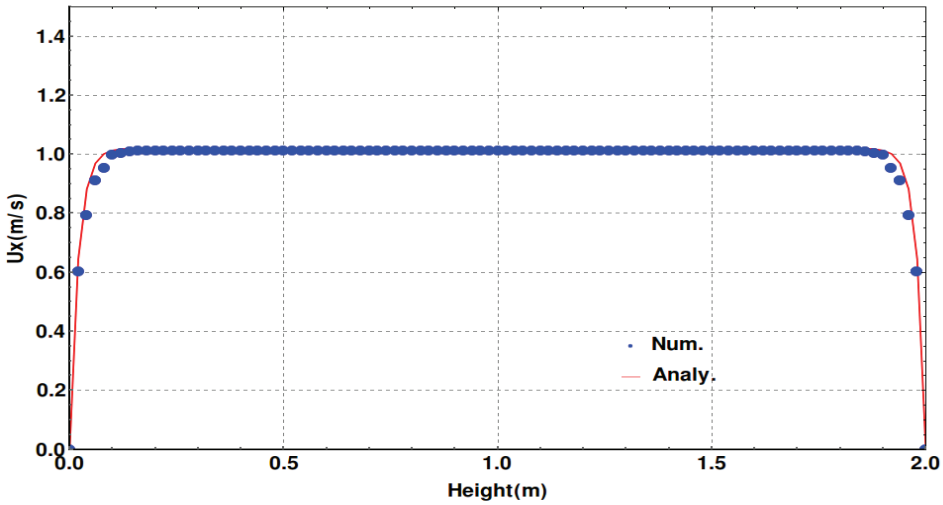

Fig.4.14. Flow velocity results in comparison with analytical solutions with B_y =50T

4.3 Temperature validation

From the detailed model description in chapter 2 it is clear that to obtain the final temperature distribution of plasma, a series of calculation regarding plasma composition, transport properties, Maxwell equation and sheath treatment need to be performed in advance, which means the temperature results play the most important role in the verification and validation of the interaction model put forward here.

As is introduced in section 2.2, cathodes working at different conditions could contribute to different applications. As our solver *chtMultiRegionFoam* is concerned, the variation of interface due to melting could not be solved in this scope. Hence our emphasis of numerical research mainly falls on GTAW. This process has been experimentally researched for many years, and many available experimental measurements such as [84] and [85] from them have provided good opportunities for researchers to

check the model validities. In this section, a steady-state two-dimensional simulation of arc welding with thoriated tungsten cathode and atmospheric argon plasma is performed with the interaction model. As for the geometry and operating condition to be simulated in this scope, it contains three typical elements (Fig.4.15): (1) a thoriated tungsten cathode, which has an angle of 60° at cathode tip and a radius of 1.6mm. The real tip in computation mesh is truncated by 0.3mm to match the shape from experiments [23]. (2) Pure argon acts as working gas which has a flow rate of 10slpm. (3) Copper anode is water-cooled to avoid metal vapor contamination and is placed 5mm away from the cathode tip.

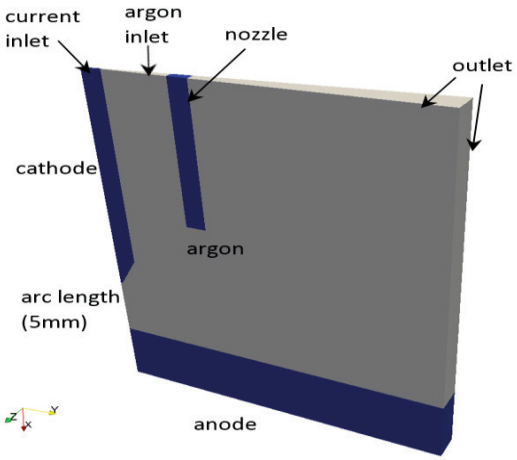

Fig.4.15. Computation geometry in this section

The mesh in adjacent to cathode is specifically refined to mimic the real dimension of plasma sheath (Fig.4.16). The structured mesh in this scope improves the accuracy especially when calculating the gradient of electric potential at plasma-cathode interface [27]. For the steady-state regime, all the transport equations neglecting the time derivative term are coded into the stationary version of our standard solver *chtMultiRegionSimpleFoam*. The simulations are performed in this scope under current intensities of 100A and 200A. Detailed information about the boundary conditions used here are shown in Table.4.6. Other important boundary conditions at interfaces are consistent with the descriptions of section 2.5. It is important to note that, to make cathode boundary condition at current inlet more realistic (here it is fixed at 500K), the geometry of cathode is ensured as long as enough (in this scope 20mm).

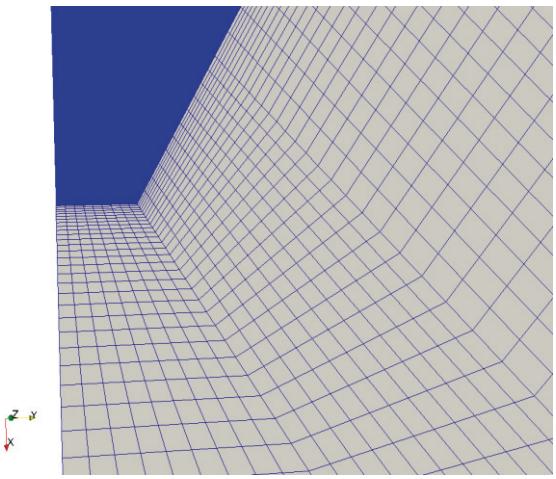

Fig.4.16. Non-uniform mesh of near-cathode region

Table.4.6. Boundary conditions for GTAW simulation

Boundaries / Variables	Argon inlet	Current inlet	Outlet	Anode bottom
$\vec{u}$	10slpm		$\frac{\partial u}{\partial n}$=0	
P	$\frac{\partial p}{\partial n}$=0		1atm	
T_h/T_s	500K	500K	500K	500K
T_e	500K		500K	
φ	$\frac{\partial \varphi}{\partial n}$=0	$\frac{\partial \varphi}{\partial n}$=-$\frac{\vec{\lvert j \rvert}}{\sigma_s}$	$\frac{\partial \varphi}{\partial n}$=0	φ=0
$\vec{A}$	$\frac{\partial \vec{A}}{\partial n}$=0	$\frac{\partial \vec{A}}{\partial n}$=0	$\vec{A}$=(0,0,0)	$\frac{\partial \vec{A}}{\partial n}$=0

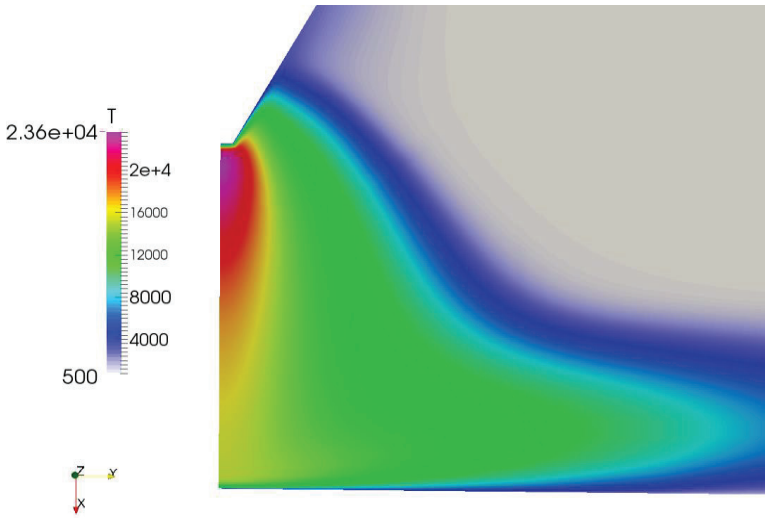

Fig.4.17. Heavy species temperature of 200A with sheath model

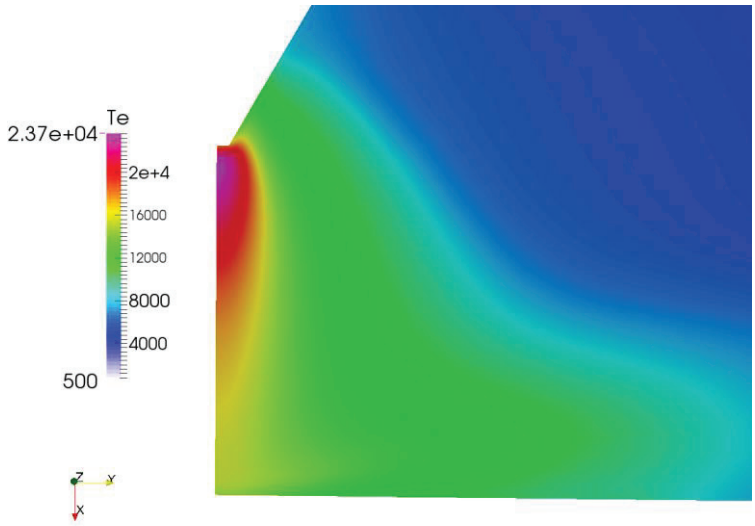

Fig.4.18. Electron temperature of 200A with sheath model

Fig.4.17 and 4.18 show the simulated results of heavy species and electron temperature at the main arc column of 200A. The maximal temperature of both shows almost no difference (23576K for Th,

23604K for T_e) at plasma center due to the efficient energy exchange at high temperature (Eq.2.21). Significant difference between the two temperatures takes place from plasma fringes where Th drops quickly down to the ambient temperature whereas T_e remains relatively high at several thousand kelvins. Such difference can be viewed in detail when the simulated 2T results of different planes away from cathode tip are compared to each other by Fig.4.19 and 4.20. On both planes, the LTE condition is strictly obeyed within several millimeters around the axis due to the careful split of total enthalpy into Eq.2.20 and 2.26, while other combinations (detailed split refer to [43]) according to our tests have more or less led to unphysical results in some regions (T_e<T_h). The nearer the plane to cathode tip, the narrower the LTE region will hold, this is due to the cooling effect of gas inflow. Away from LTE region, thermal nonequilibrium becomes more and more evident due to the rapid decrease of electron number density and collision frequencies that lead to small energy exchange between them. Besides, it is obvious from Fig. 4.21 that at near-cathode region, the value of T_e/T_h is over 3. This is due to the frequent energy exchange between heavy species and the cathode surface through complicated processes such as ion bombardment heating that makes cathode surface temperature (usually under 4000K) and temperature of atoms and ions in the sheath equilibrate with each other, while electrons from plasma are assumed to be adiabatic to the electrode walls.

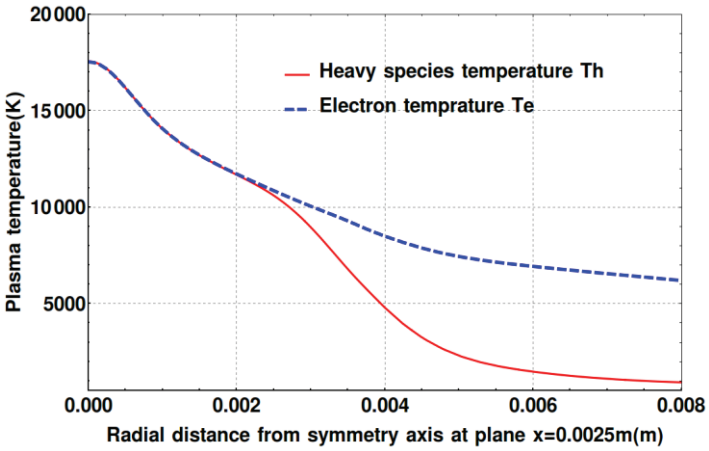

Fig.4.19. Two-temperature distribution of 200A at plane x=0.0025m

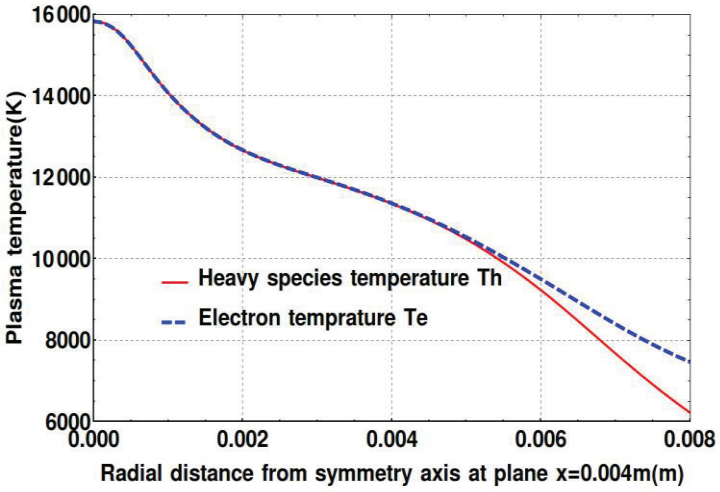

Fig.4.20. Two-temperature distribution of 200A at plane x=0.004m

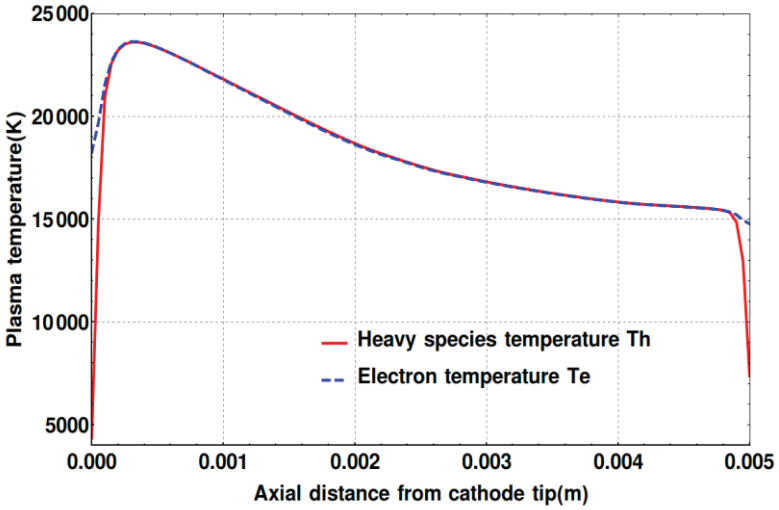

Fig.4.21. Two-temperature distribution along the symmetry axis of 200A

The simulated results of heavy species temperature along the axis attained from 100A and 200A discharge current shown in Fig. 4.22 and 4.23 are compared with experimental measurements provided by Haddad et.al [84] under same operating condition. It is obvious that after sheath treatment by applying the effective electrical conductivity (Eq.2.117), the temperature distributions of both current intensities are in much better agreement with experimental data. The maximal temperature deviation from experimental measurement without sheath treatment of both current densities is over 7000K. This manifests the role that space-charge effect plays in constricting the cathode emission current. Because at the cathode tip, due to the intensive joule heating, the plasma is near to fully ionized, hence our effective value tends to exhibit the conductivity of bulk plasma. Away from cathode tip, the ionization degree decreases gradually, leading to a correspondingly decreasing sheath electrical conductivity which damps local electron emission. As a result, almost all the current inside bulk cathode concentrates at cathode tip, leading to much higher temperature. Another feature of sheath treatment in this scope is that, as sheath conductivity only applies to the boundary cells, which is specifically restricted to a very small dimension, it will exert little numerical influence on bulk plasma and ensures numerical stability.

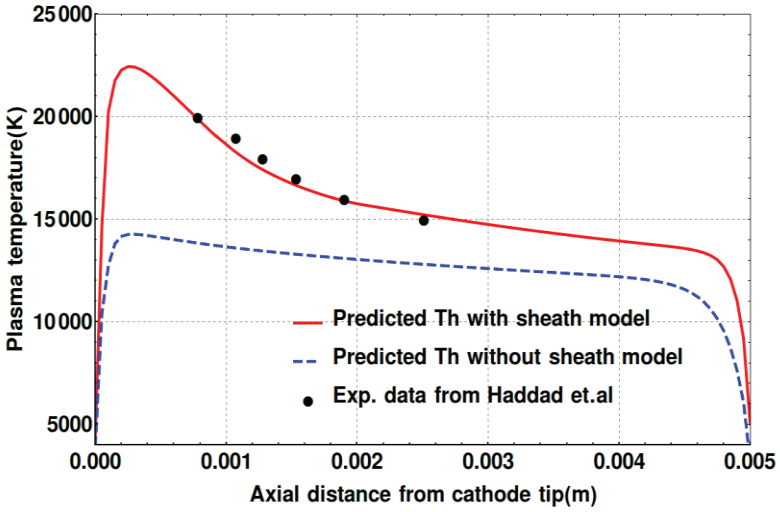

Fig.4.22. Heavy species temperature results of 100A in comparison with exp. data

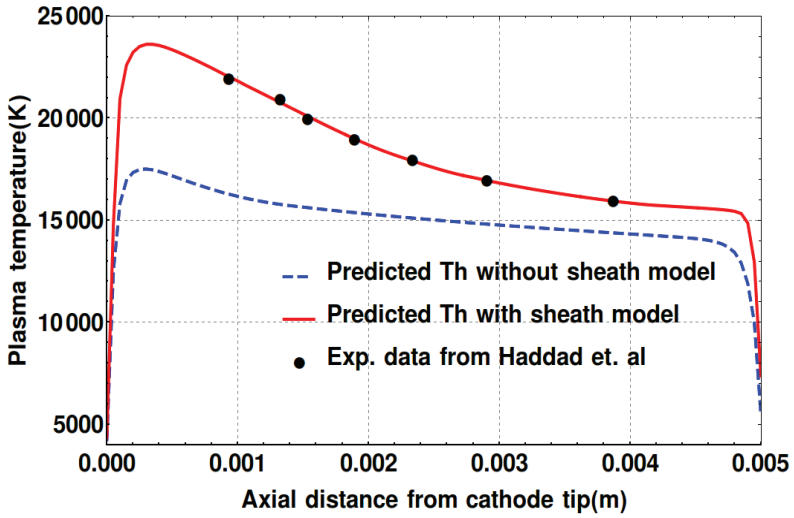

Fig.4.23. Heavy species temperature results of 200A in comparison with exp. data

Different from many zero-dimensional sheath treatment ([27], [28] and [37]), the reservation for the one-dimensional sheath treatment by the boundary layer allows to describe not only a non-uniform cathode emission current through local value of σ_{eff} but also an evident sheath voltage drop within the boundary cells away from cathode spot that rejects further electron inflow (Fig.4.24). On the contrary, the results without sheath treatment (Fig.4.25) cannot reflect this phenomenon. Although charge separation within the sheath cannot be solved by our equations due to stability issues, the voltage drop caused by it could be obtained from these two sets of electrical conductivities on each side of sheath-presheath interface.

In accordance to the temperature results, the total voltage predicted for 200A current with and without sheath is 11.8 V and 9.8V respectively. There's still a deviation of 1.5 V compared with experimental measurement (13.3V) after sheath treatment. This may result from the absence of anode sheath model and charge separation neglected in this study. For 100A current the results are 9.8V and 6.9V, which has a similar relation.

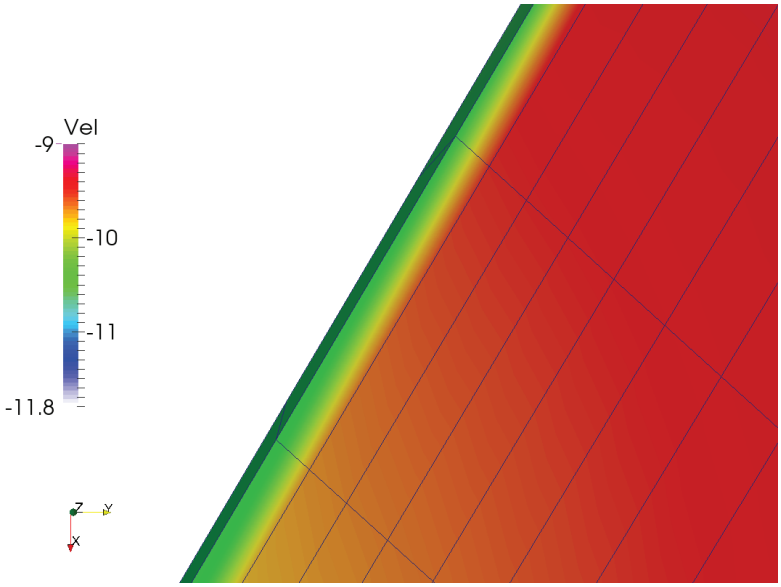

Fig.4.24. Electric potential results of 200A near cathode surface with sheath model

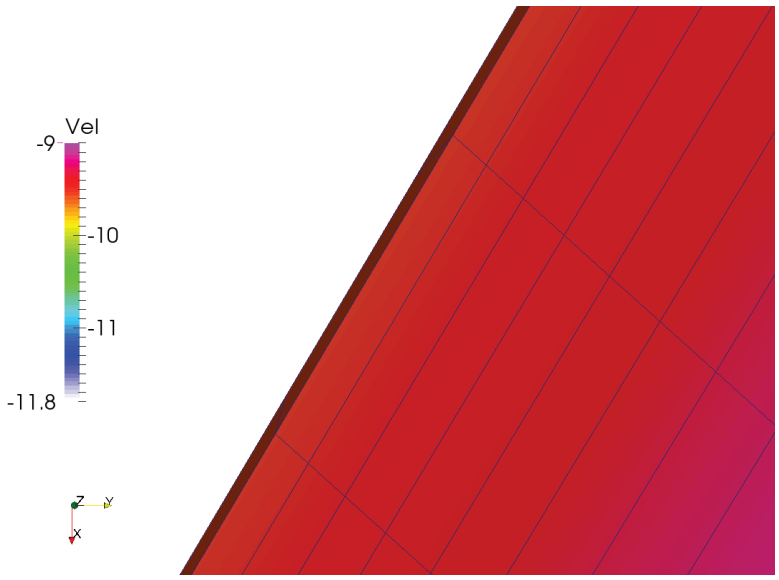

Fig.4.25. Electric potential results of 200A near cathode surface without sheath model

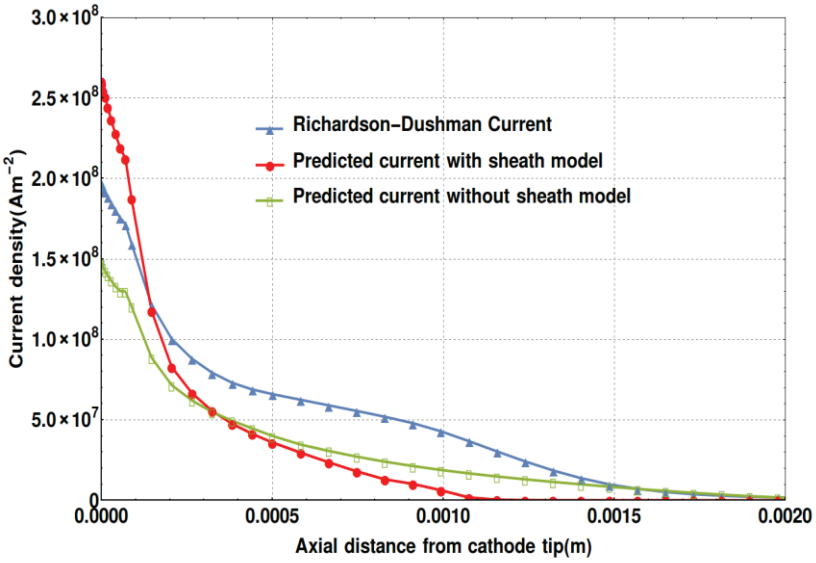

Fig.4.26. A comparison of cathode surface current density

Fig.4.26 shows the predicted cathode surface current for 200A along with Richardson-Dushman current attained according to Eq.2.57 with sheath results. The maximal current density magnitude that appears at cathode tip has a value of 2.6× 10^8 A/m^2 with sheath and 1.48× 10^8 A/m^2 without sheath. The result of current density with sheath treatment is higher than that of without sheath within the cathode spot, whereas lower outside it. The more diffusive property of the latter is required by the conservation of total current integrated over the whole cathode surface. The predicted maximal value by Zhu et.al [23] under same condition is 2.8× 10^8 A/m^2, this slight difference may result from the extra inclusion of back diffusion current by electron considered in this study, which offsets part of the thermionic emission current. When compared with Richardson-Dushman current, the predicted current density with sheath is larger only within cathode spot and decays more quickly away from it. This is explained by the fact that within cathode spot, there are plenty of ions due to the high ionization degree and the emitted electrons from cathode surface cannot fully recombine them, hence the ion current flow still exists, making total current density higher than J_{em}. Away from cathode spot, due to

the intensive space-charge effect, electrons are rejected from cathode layers, which makes total current density smaller than J_{em}.

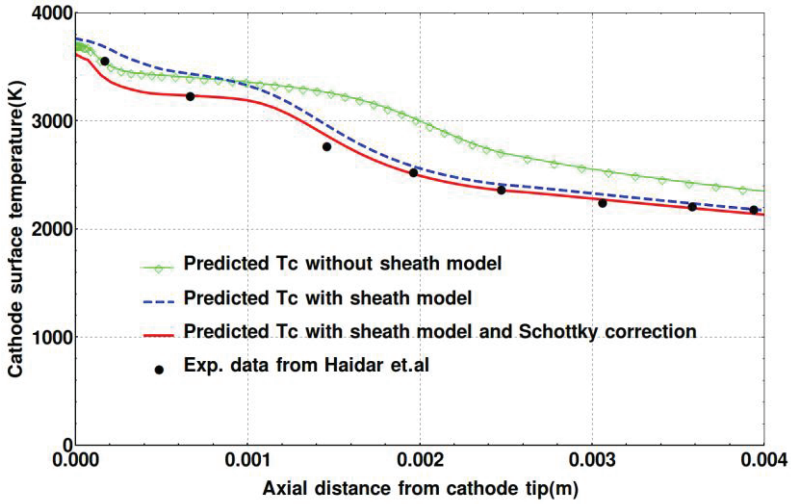

Fig.4.27. A comparison of cathode surface temperature

The predicted cathode surface temperature results for 200A are shown in Fig.4.27. For the case without sheath treatment, the surface temperature is generally higher than experimental values taken from Haidar et. al [85]. After sheath restriction (blue dashed line), the temperature results are improved especially outside cathode spot. The surface temperature decreases further after extra consideration of field enhanced thermionic emission described by Schottky's formula represented by Eq.2.58 and 2.59 a-d (red line). The decrease of the cathode work function gives rise to larger thermionic emission which further cools down the cathode surface. In [86], a series of experimental researches were conducted and the relations of work function of cathode to cathode surface temperature and discharge current were evaluated, which confirms such influence. This cooling effect is more obvious within the cathode spot and yields the most realistic results compared with other two situations. However, we still attain an underestimation of cathode tip temperature of about 150K. This suggests that our simplified description of sheath processes requires further improvements and more sophisticated processes such as effects of plasma contamination by metal vapor from cathode should be considered in the future.

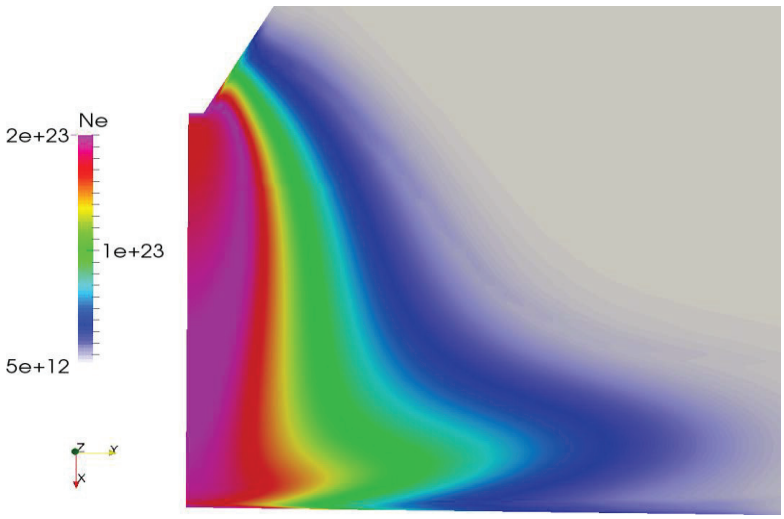

Fig.4.28. Number density of electron of 200A with sheath model

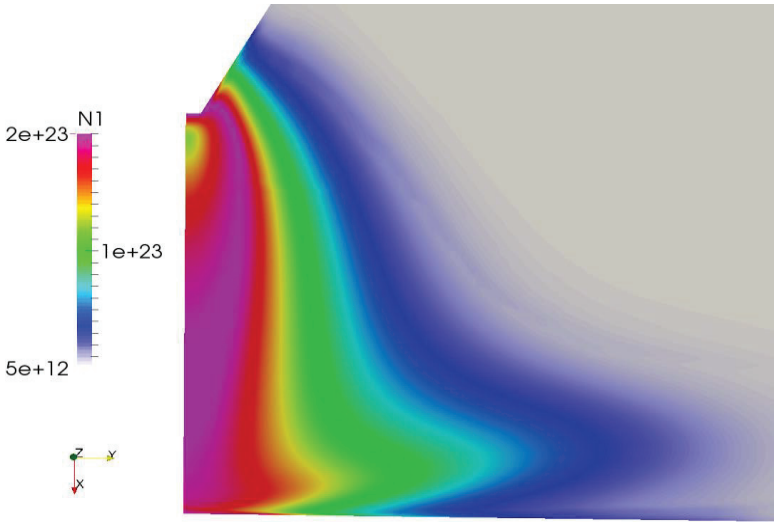

Fig.4.29. Number density of singly charged argon ion of 200A with sheath model

The number density results attained for 200A case are shown in Fig.4.28 and 4.29. It is clear that a small circle region appears at the center of n_1 distribution in comparison with n_e distribution, which manifests the deviation of n_e from n_i due to a rising existence of doubly ionized argon ions. As the maximal temperature in the arc center after sheath constriction effect is over 23000K, the maximal relative discrepancy between them is as high as 60%, hence the assumption of single ionization $n_e = n_1$ in this region no more applies.

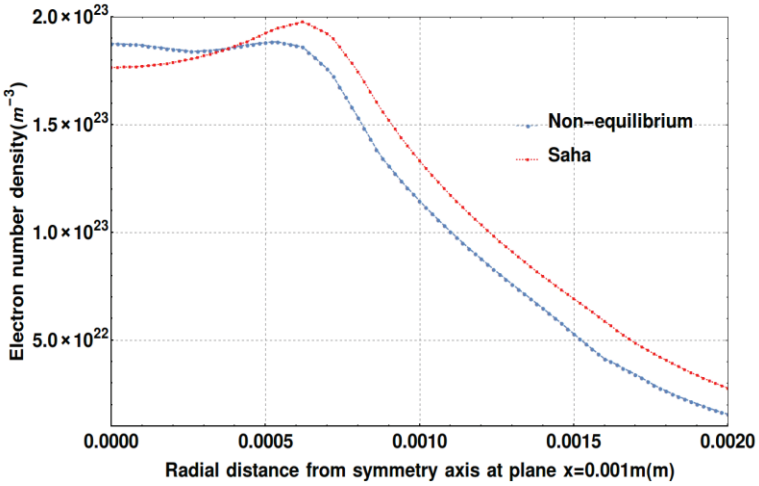

Fig.4.30. Number density results from equilibrium and nonequilibrium methods at plane x=0.001m

Not only the thermal nonequilibrium but also chemical nonequilibrium is prevailing in arc plasma. The latter is manifested by a deviation of number densities from Saha equilibrium. The distribution of nonequilibrium composition is directly linked to convection, diffusion and source term described by Eq.2.3-2.5. Fig.4.30 shows the nonequilibrium electron number density predicted by models of Lotz [36] and Lien [38], while the equilibrium one by Saha equation. All the figures show a similar trend: around the axis, plasma has a net ionization as our results are higher than Saha's values. Away from arc center, the relation is just the opposite, this is due to the net recombination around the arc fringes. The ionization/recombination trend predicted in this study is consistent with the report of Baeva et al. [37]. The nearer the plane to the cathode tip is, the narrower the net ionization region will be. This follows the similar trend of the local dimension of the LTE region discussed earlier in this section.

However, plasma starts to recombine when it is still within the LTE region as the width of net ionization region is smaller than that of LTE region. Besides, although the maximal temperatures shown in Fig.4.19 and 4.20 locate at the axis exactly and decay quickly away from it, the number density results attained don't follow this trend, regardless of equilibrium or nonequilibrium situation. The region of local maximum extends from axis and in some places even slightly larger than the axis values. It is because the strong convective transport of electrons here dominates over all the other factors as the plasma velocity magnitude around the axis is much larger than that of its surroundings. When approaching both electrodes, as velocity magnitude decreases quickly, the effect of electron convection diminishes correspondingly. If it is within the ionization length, diffusion process becomes the dominant factor in determining the distribution of electron densities.

Chapter 5

3D Simulation of Non-transferred DC Plasma Torch

The intended simulation task to realize the coupled simulation of plasma-electrode interaction in a D.C. plasma torch is based on the Praxair SG-100 plasma-spray torch with a thoriated tungsten cathode, a coaxial tubular copper anode and a steel substrate. The diameters of anode and cathode at inlet are 18mm and 10.4mm respectively. At the nozzle part the diameter is kept at 8mm until outlet, while the distance between outlet and cathode tip is 30.3mm. To reduce the overall cell number for economic computation and achieve a stable 1D sheath calculation as well, the structured meshes are generated in all the four regions (the region for cathode, anode, plasma and substrate shown in Fig.5.1 and 5.2). As is mentioned in section 4.1, using coupled boundary condition at interfaces for magnetic vector potential requires an exact same cell thickness of both sides, the boundary cells inside cathode are therefore also refined to match those inside the sheath. While using the software *Gmsh* it may be more convenient to use rotation function to extend 2D meshes to 3D, the generated Triangular prism cells will thus have a very small spacing which will lead to extremely small time steps even if courant number is set large enough. The butterfly meshes are applied in the center of the geometry to avoid such problem (Fig.5.3 and 5.4). In combination with the field initiation and interface relations introduced in section 2.5, the simulation results performed under such conditions are shown in the following sections with external boundary conditions shown in Table.5.1.

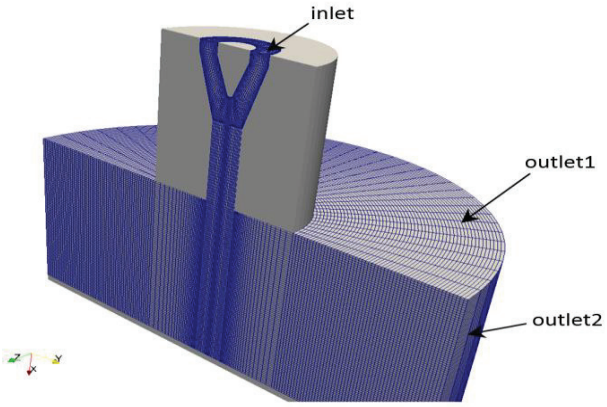

Fig.5.1. Structured mesh in plasma region

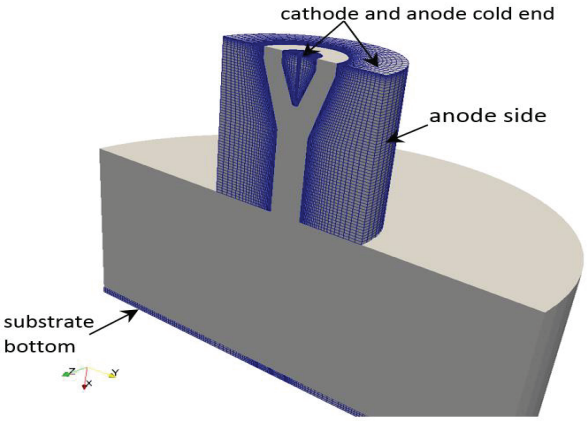

Fig.5.2. Structured mesh in electrodes and substrate regions

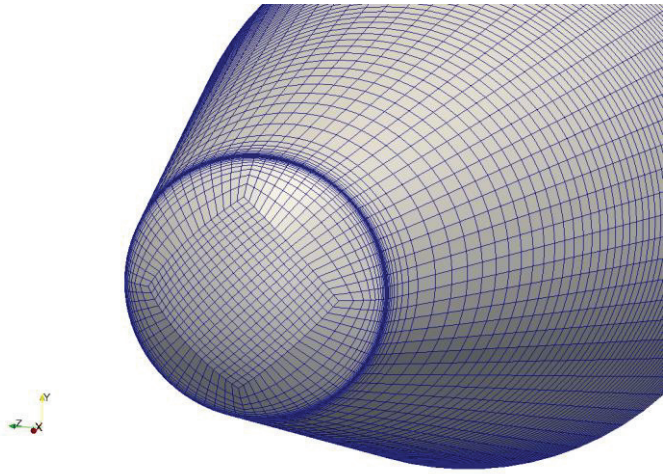

Fig.5.3. Structured “Butterfly” mesh on cathode tip surface

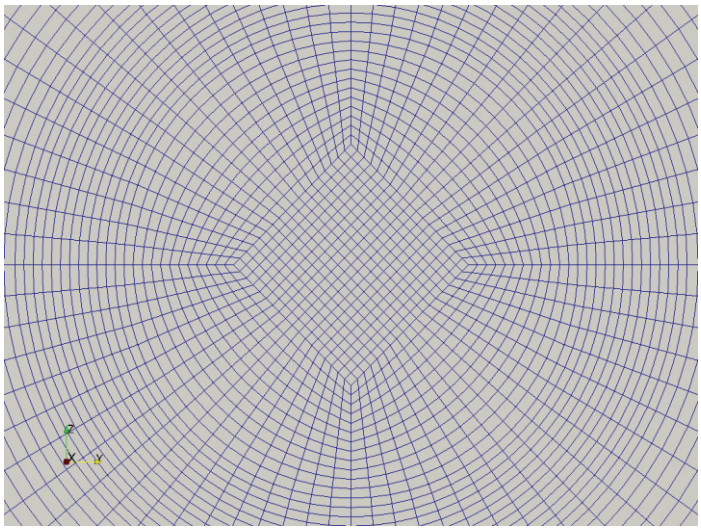

Fig.5.4. Structured “Butterfly” mesh on substrate plate center

Table.5.1. Boundary conditions for the non-transferred plasma torch simulation

boundaries / variables	inlet	outlet1	outlet2	cathode cold end	anode cold end	anode side	substrate bottom
$\vec{u}$	60slm	$\frac{\partial u}{\partial n}$=0	$\frac{\partial u}{\partial n}$=0	–	–	–	–
p	$\frac{\partial p}{\partial n}$=0	1 atm	1atm	–	–	–	–
T_h/T_s	500K	500K	500K	500K	$\frac{\partial T}{\partial n}$=0	500K	500K
T_e	$\frac{\partial T_e}{\partial n}$=0	$\frac{\partial T_e}{\partial n}$=0	$\frac{\partial T_e}{\partial n}$=0	–	–	–	–
φ	$\frac{\partial \varphi}{\partial n}$=0	$\frac{\partial \varphi}{\partial n}$=0	$\frac{\partial \varphi}{\partial n}$=0	$\frac{\partial \varphi}{\partial n}$=-$\frac{\lvert\vec{J}\rvert}{\sigma_s}$	$\frac{\partial \varphi}{\partial n}$=0	φ=0	$\frac{\partial \varphi}{\partial n}$=0
$\vec{A}$	$\frac{\partial \vec{A}}{\partial n}$=0	$\frac{\partial \vec{A}}{\partial n}$=0	$\vec{A}$=(0,0,0)	$\frac{\partial \vec{A}}{\partial n}$=0	$\frac{\partial \vec{A}}{\partial n}$=0	$\vec{A}$=(0,0,0)	$\frac{\partial \vec{A}}{\partial n}$=0

5.1 Arc jet fluctuation and flow field results

In section 4.3 it is mentioned that sheath region may have a constricting effect on arc jet. This is very important in obtaining the realistic results regarding temperature, voltage, number density, etc. Obviously, this model should also be applied on the plasma torch discharge simulation as the principles

are the same. Different from the arc welding system, which is a stable discharge system and can be described by the steady-state regime, the non-transferred plasma torch is dominated by instabilities which is time-dependent. This is due to fact that the current path from anode to cathode is constantly changing affected by flow condition from inlet, the movement of current path in turn gives rise to local gas expansion caused by joule heating. This local expansion will then break the balance between gas dynamic force and Lorentz force. As swirl injection is applied in the simulation, this will further enhance such instability.

Consistent with the presentation of results shown in section 4.3, a series of comparisons between the simulated results such as temperature, electric potential and current densities etc. with and without the previously introduced cathode sheath model are pursued. With sheath model, we manipulate the electrical conductivity inside cathode boundary cells according to the introduced effective value while for the situation without sheath model we simply use 2T nonequilibrium values from look-up table for electrical conductivity everywhere, which are originally meant for bulk plasma only. For convenience, we will call it 2T model in the following discussions.

It is clear from Fig.5.5 that the electric potential distribution from 2T model is almost symmetric and uniform, no discontinuity in the near-cathode region is observed. It is understandable since without sheath constriction in this case, the emission current is more diffusive, leading to an arc column with larger radius. It will generate a larger expansion region within the gas flow whereas the gradient of energy distribution is much smaller. In this case, the arc jet is prone to stay in a steady state or fluctuate in a milder way. As sheath layer is represented by the thin boundary cells which are directly attached to cathode surface, it can be observed clearly only when it is enlarged in detail (Fig.5.7 and 5.8). The infinite small negative value attained in our potential results may stem from the zero-gradient boundary condition at plasma outlet instead of a fixed value condition as is defined in anode outer surface. In the boundary cells of sheath situation (Fig.5.8), drastic potential drop (in green) is simulated, which is due to the large difference of electrical conductivity in- and outside boundary cells. A more detailed comparison of electric potential attained between these two conditions at line 1 from Fig.5.5 and 5.6 is shown in Fig.5.9. Fig.5.10 shows the potential distributions along different lines of Fig.5.6 starting from cathode surface. Line 1 to line 4 represents cross sections of x= 0.001m, 0.005m, 0.01m and 0.012m. The potential drop inside sheath layer at line1 occupies over 85% of the whole region, which approaches the condition for a Child sheath which assumes no potential drop outside sheath, while at line 4, which locates inside cathode spot, little potential drop can be observed. This can be interpreted in the following way: because line 1 situated faraway from emission center, the cathode surface is non-emitting, hence large potential barrier is necessary here to preserve charge neutrality in bulk plasma.

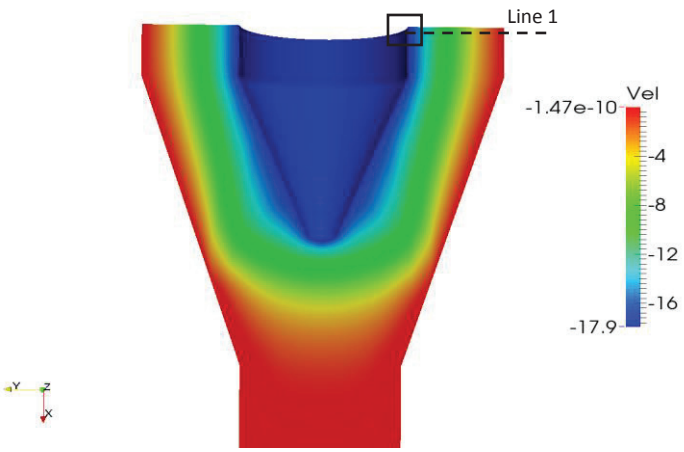

Fig.5.5. Distribution of electric potential from 2T model

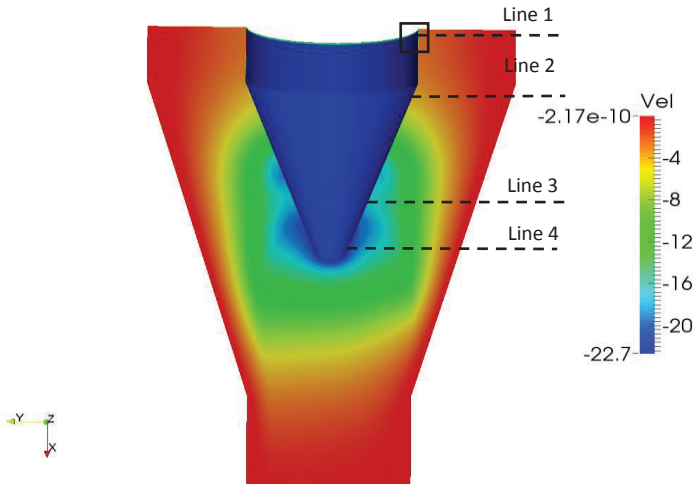

Fig.5.6. Distribution of electric potential from sheath model

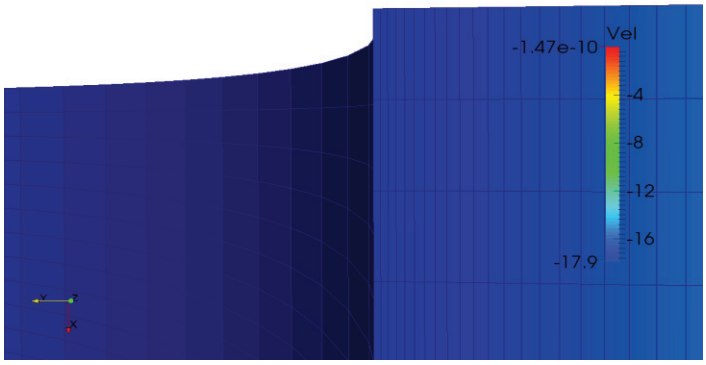

Fig.5.7. Local magnification of box in Fig.5.5 without sheath layer

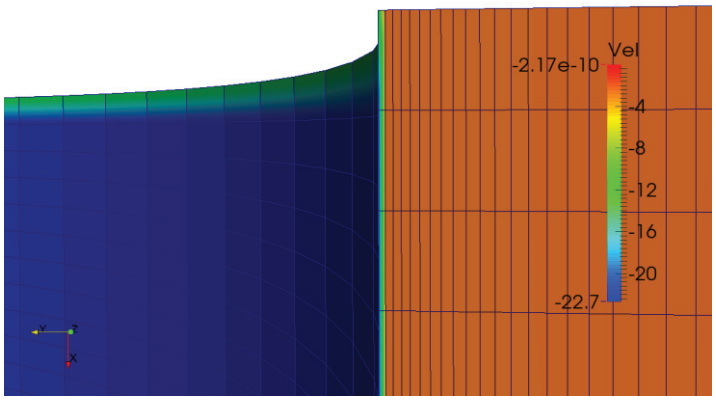

Fig.5.8. Local magnification of box in Fig.5.6 with sheath layer

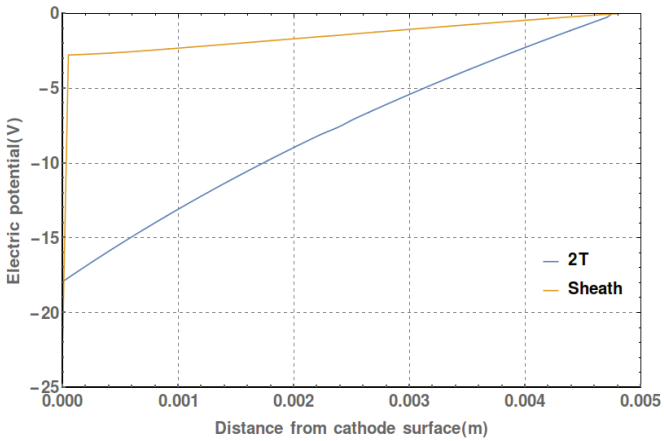

Fig.5.9. Comparison of potential distributions from two different situations along line 1

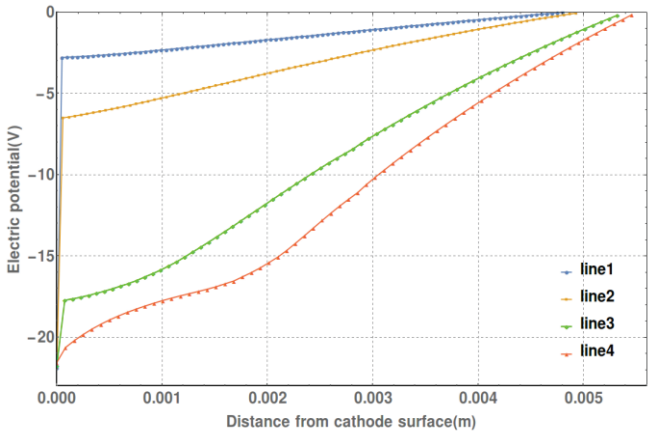

Fig.5.10. Potential distributions from sheath model along line 1~4

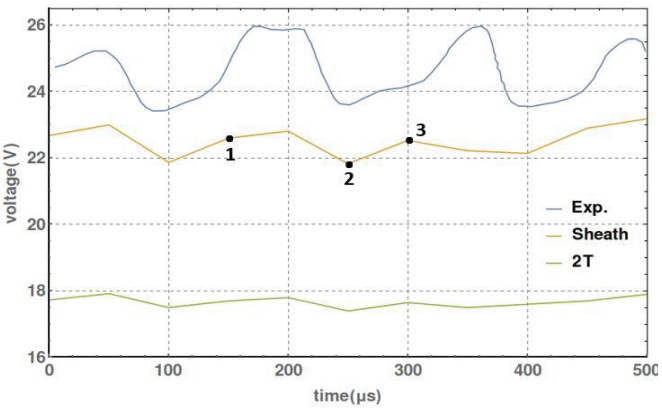

Fig.5.11. Predicted results of both situations in comparison with experimental results

On the contrary, line 4 situated directly in the spot center, and large amount of emission electrons from cathode moving towards plasma bulk, making it rich in electrons, hence there's no need here for a charge barrier to exist in order to prevent electron loss that will violate charge neutrality. This self-cancelling result was also attained in [25].

In Fig.5.11, the time-resolved numerical results for voltage attained in this study are compared with the experimental measurements under same operating condition reported in [42]. The numerical results are recorded every 50 μs.It is obvious that in 2T situation, the simulated potential drop is far below the experimental results, which is due to the overestimation of arc attachment that lead to a lower emission current density than reality. With sheath model, the predicted potential drop is much closer to reality despite that there's still a small amount of difference of 1 to 2 V compared with experiment measurements, which may result from the omission of anode sheath in this study. Besides, it is clear from this figure that voltage fluctuation is also captured. This is due to the arc jet instability caused by a complex of many factors: Firstly, a swirl injection boundary condition is imposed at gas inlet (section 2.5.2). This technique is used to achieve a vortex stabilization that reduce heat load onto anode by forcing arc attachment move with certain frequency around anode surface. Despite this practicality, this technique contributes to pressure oscillations inside the cathode cavity, this compressibility effect was found by [87] to result in the arc instability, whose main oscillation frequency $f_H$follows the Helmholtz resonator law:

$$f_H = \frac{1}{2\pi}\sqrt{\gamma_g \frac{P_g S}{\rho L V_g}}, \tag{5.1}$$

where γ_g , P_g are the isentropic coefficient of cold gas and the pressure in the cathode cavity, respectively. S, L and V_g are the cross section area of anode nozzle, the volume of cathode cavity and the length of nozzle channel, respectively. Secondly, when the cold surrounding gas meets the hot, fully ionized plasma jet, great gradient of adverse velocity, temperature and density will develop, causing strong shear instability. Thirdly, the interaction of arc current with the magnetic field induced by both the emission current itself and metal cathode will generate the so-called Kink and Sausage instability [88]. The former is a kind of magnetic instability which is caused by the curvature of the arc jet. The curvature will make considerable difference of magnetic field between the concave and the convex sides. The generated magnetic pressure will further distort the arc jet to form a new anode attachment. The latter usually appears when the cross section area of arc jet is not uniform, the reduction of cross section area will produce an enhanced self-induced magnetic field which forms net magnetic pressure that further constricts arc jet, this will usually have a direct effect on cathode emission area. Although the self-induced magnetic field is usually weak, it adds a considerable rotation velocity due to Lorentz force where the arc current density is large. The numerical results concerning the electrical and magnetic instabilities at the corresponding observation points 1~3 from Fig.5.11 are shown in Fig.5.12 and 5.13, where the effect of both instabilities can be clearly seen. Finally, due to the restriction effect of sheath model, the arc core radius is smaller than that of 2T model, making arc more unstable. That's why from our results the voltage fluctuation with sheath model is stronger than 2T model.

The corresponding heavy species and electron temperature fluctuations for point 1~3 with sheath model are presented in Fig. 5.14 and 5.15 respectively. They are all scaled to the same temperature range between 500K and 25000K. Consistent with the electromagnetic results in Fig.5.12 and 5.13, the temperature distributions of both T_e and T_h also shows an unsymmetrical feature and the arc jet always attaches to a preferable region. The calculated maximal heavy species temperatures of 2T and sheath situation are 25000K and 31500K respectively. The large temperature difference between the two situations is due to fact that in the sheath situation the current is further constricted by σ_{eff}, making Joule effect more intensive to heat plasma. While heavy species temperature reflects the development of shear flow instabilities clearly, the electron temperatures of both situations exhibit a diffusive property. This could be attributed to the higher thermal conductivity of electrons than that of heavy species. The most obvious thermal nonequilibrium between electron and heavy species temperature occurs at the gas inlet region, where the heavy species temperature approaches 500K but the electron temperature is still over several thousand kelvins. This may be attributed to the same

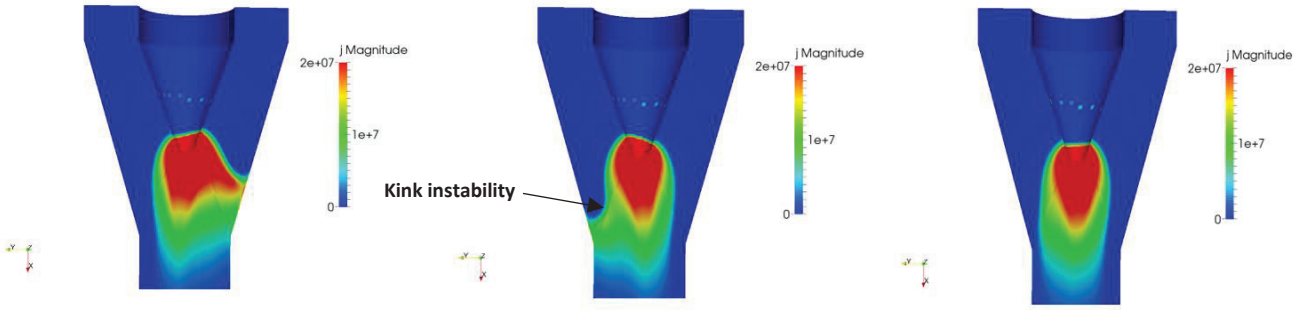

Fig.5.12. Transient current density profile scaled under $2\times 10^7 \mathrm{A}/m^2$ at different observation points: point1(left), point2(middle), point3 (right)

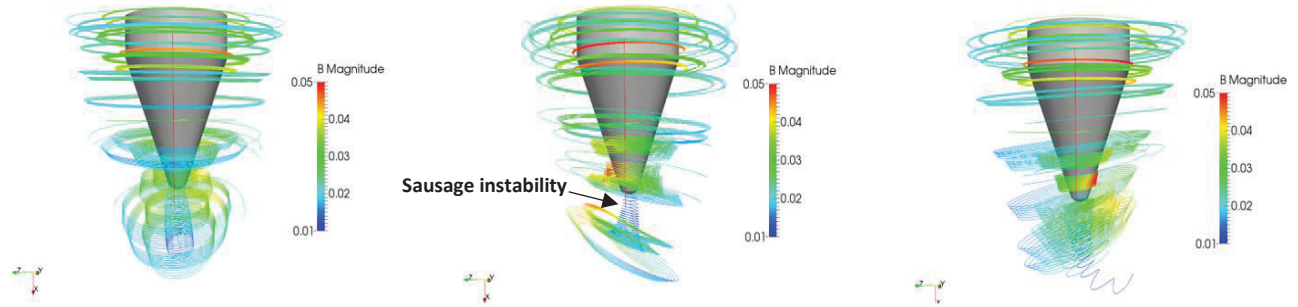

Fig.5.13. Transient streamline profile of magnetic flux density scaled under 0.05T at different observation points: point1(left), point2(middle), point3 (right)

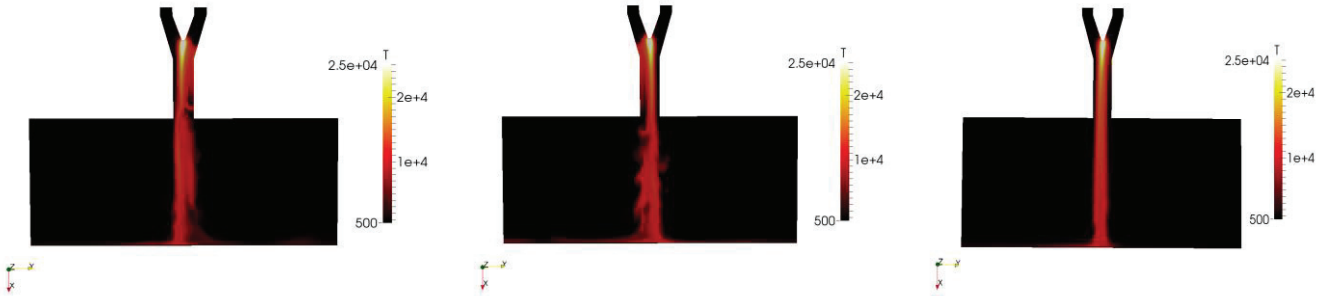

Fig.5.14. Transient heavy species temperature profiles at different observation points: point1(left), point2(middle), point3 (right)

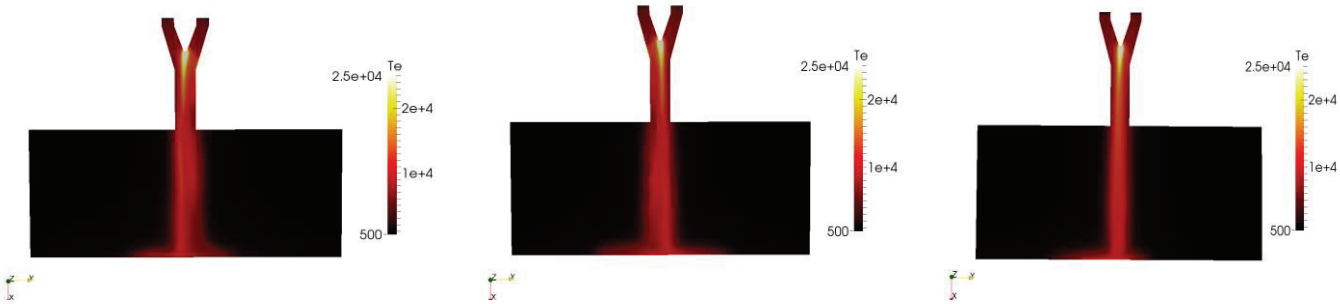

Fig.5.15. Transient electron temperature profiles at different observation points: point1(left), point2(middle), point3 (right)

reasons which have been already discussed in section 4.3. Besides, the calculated the maximal Mach number in the nozzle with our sheath model is 0.7, which is consistent with the simulation results reported in [42], who imposed a boundary condition for current density at cathode surface, which is based on the experimental measurement.

From Fig.5.16 it is interesting to find out that a small scaled discharge path downstream from the original attachment. It seems like the so-called reattachment phenomenon found in many non-transferred plasma torch experiments. However, as the results following it are concerned, it didn't trigger a typical reattachment process as expected, the small current path died away quickly instead of forming a new attachment. According to [13], the prerequisites of reattachment process are the presence of diatomic gases and high gas flow rate. For the pure argon condition simulated here, it is understandable that no reattachment process could be obtained. But when comparing the temperature and velocity results (Fig.5.16 and 5.17), it is clear that temperature and velocity are strongly correlated with each other, the local small current path near nozzle outlet not only gives rise to higher temperature but also higher velocity. This phenomenon has been experimentally confirmed by [9]. The extra current path appeared in our simulation results may be attributed to not only the turbulence development at outlet, but also the fact that arc jet movement happens both in radial and axial directions, while both of them have their own attachment frequencies, which are independent from each other. This could be verified by a comparison between the axial results shown above and the radial results shown in Fig.5.18. Due to a relatively small cross section area along the tube, it tends to form more than one attachment in the radial direction, while it could hardly exert any effect on the temporal voltage development since the total arc length is determined only by axial attachment.

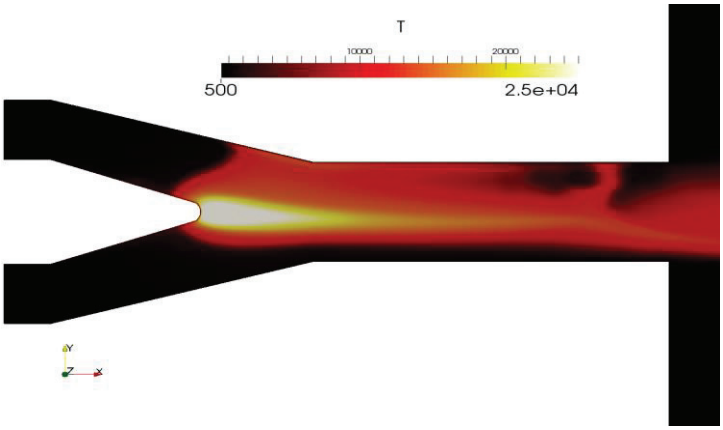

Fig.5.16. Heavy species temperature captured inside nozzle with an extra current path

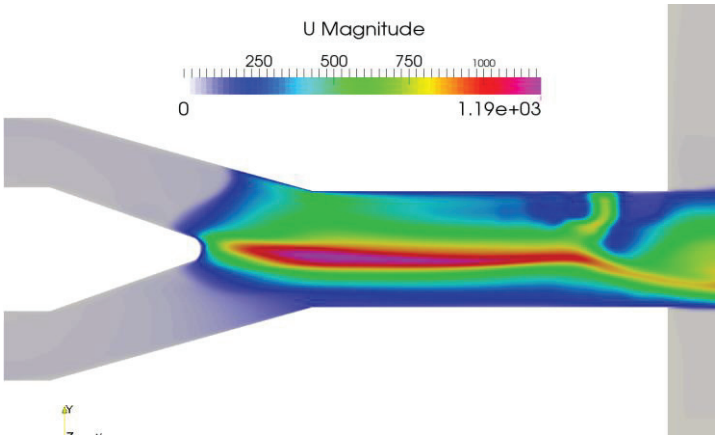

Fig.5.17. Velocity profile captured inside nozzle with an extra current path

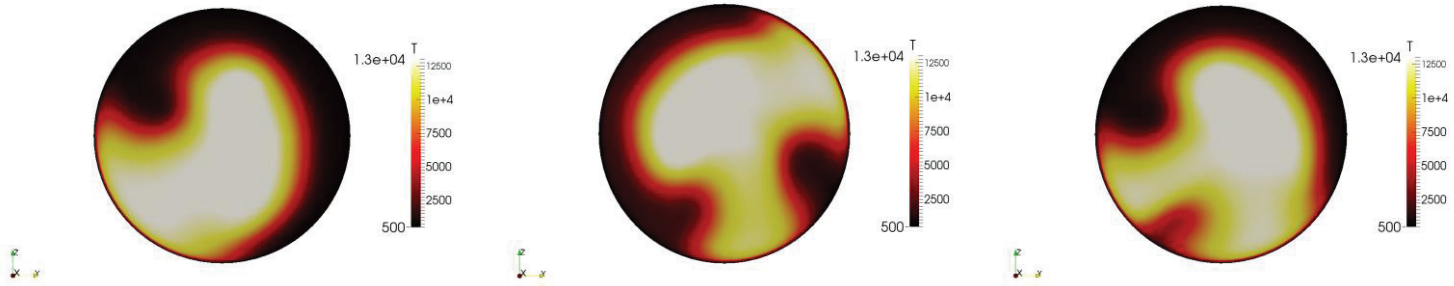

Fig.5.18. Transient radial temperature development of heavy species triggered by arc jet fluctuation

Similar to the number density simulation reported in section 4.3, the electron population inside plasma core deviates a lot from that of singly charged ions (Fig.5.19). While n_e remains over $10^{23}/m^3$ in the arc core, n_{Ar^+} drops under $10^{22}/m^3$ due to the local high temperature of over 30000K. On the contrary, the proportion of $n_{Ar^{2+}}$ and $n_{Ar^{3+}}$ increase significantly, leading $n_{Ar^{2+}}$ to the main kind of charged ions in this region. Besides, due to the fluctuate property of arcs in plasma torch, the distributions of number densities vary with time correspondingly (Fig.5.20).

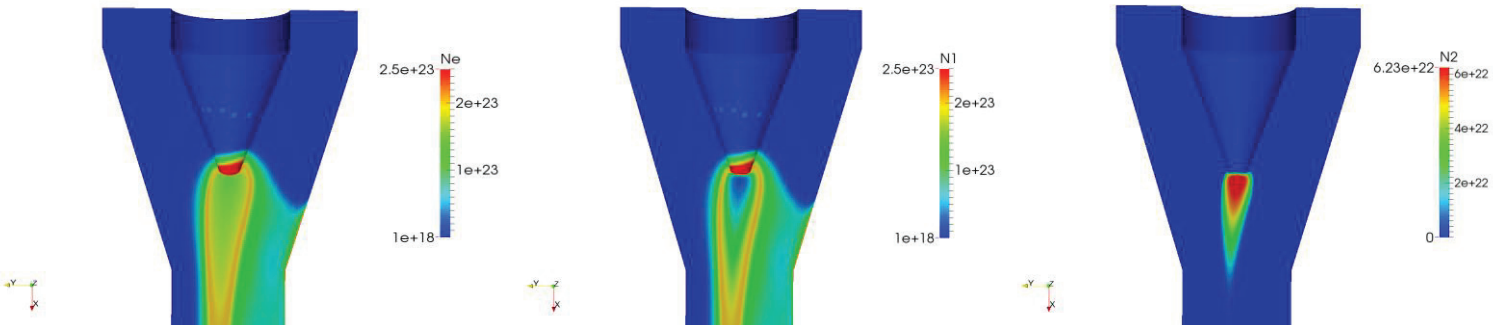

Fig.5.19. Results of plasma composition: electron (left), singly charged argon ion(middle), doubly charge argon ion (right)

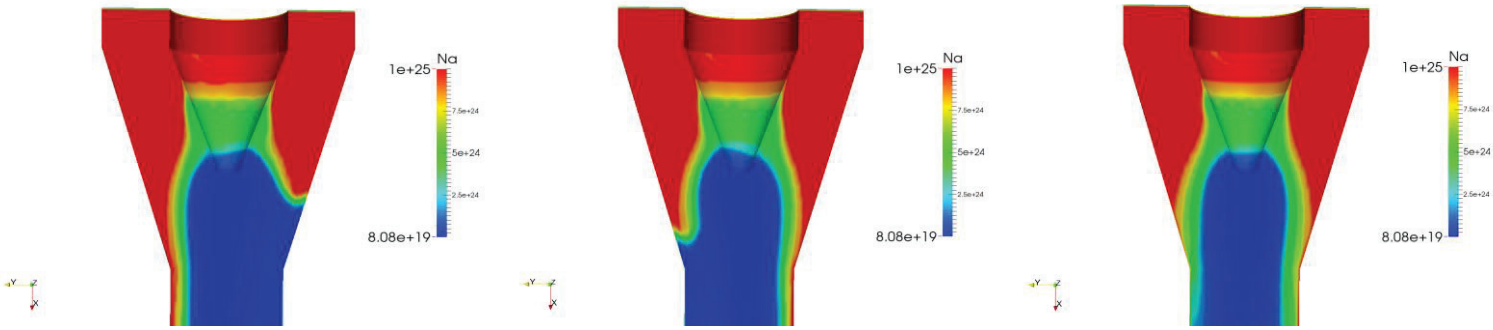

Fig.5.20. Calculated number density fluctuation of neutral atom

5.2 Electrode region results

The electrode regions are coupled with the plasma with procedures introduced previously. The maximal cathode surface temperature of 2T and sheath situation is 3600 and 3800 K respectively as melting and evaporation are ignored. Fig.5.21 shows the cathode surface temperature fluctuation at different observation points from Fig.5.11. It is clear from the figure that the fluctuating feature of

cathode surface temperature distribution is consistent with what has been observed in plasma region. This is because cathode surface temperature is directedly affected by ion bombardment heating that comes from plasma, since we assume that all the neutralization energy of ions is delivered as thermal energy onto cathode surface. It is noteworthy that the maximal surface temperatures at all the points locate not just right at exactly the tip center of cathode. Such temperature deviation from cathode tip has been experimentally observed by [85]. On one hand, this is due to the large amount of thermionic emission cooling by J_{em} at the interface. On the other hand, as the arc is always attached to a preferred side in our simulated results, the real arc spot center on the cathode surface is prone to deviate from cathode tip to form the shortest arc length to anode.

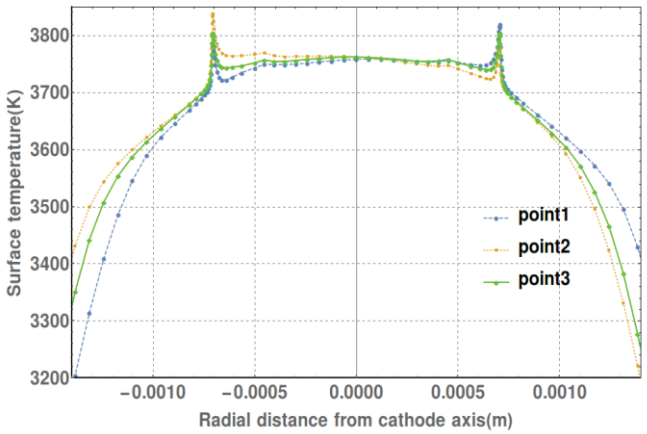

Fig.5.21. Cathode surface temperature fluctuation at different observation points

The comparison between the predicted current density of cathode surface and the theoretical value attained from Eq.2.57 is shown in Fig.5.22, which also shows the asymmetric and time-dependent feature. Similar to the comparison made in section 4.3, the calculated results achieve good agreement with the theoretical value within the attachment region. The deviation in some part from the theoretical value determined by Richardson's formula could be attributed to the same reasons discussed in section 4.3.

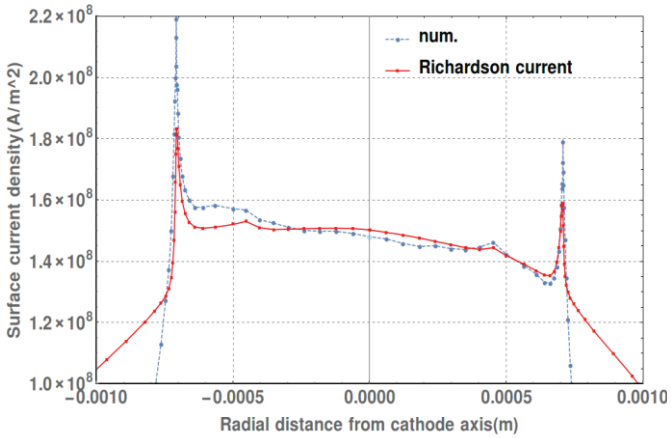

Fig.5.22. Cathode surface current density comparison between predicted and theoretical values

The rotating feature of anodic arc root manifested by the time-resolved anode surface temperature distributions is shown in Fig.5.23. As we don't apply any anode sheath model in the present research, the real anode attachment may deviate. As in the 2T situation, due to larger arc attachment area at cathode and thus a more stable arc, less voltage fluctuation is predicted in plasma region compared

with sheath situation, the corresponding anode attachment shown in the figure is also relatively uniform and simply a reflection of swirl injection. On the contrary, the anode surface temperature of sheath situation is much higher, and the attachment point is much more asymmetric and random in accordance with the results of radial plasma movement inside nozzle shown in Fig.5.18, which is dependent on the relation between Lorentz and gas dynamic drag force in the anode boundary layer. It could be concluded that anode attachment is closely tied to the development of flow fields in plasma region in both radial and axial directions as well as the emission situation in the near-cathode regions.

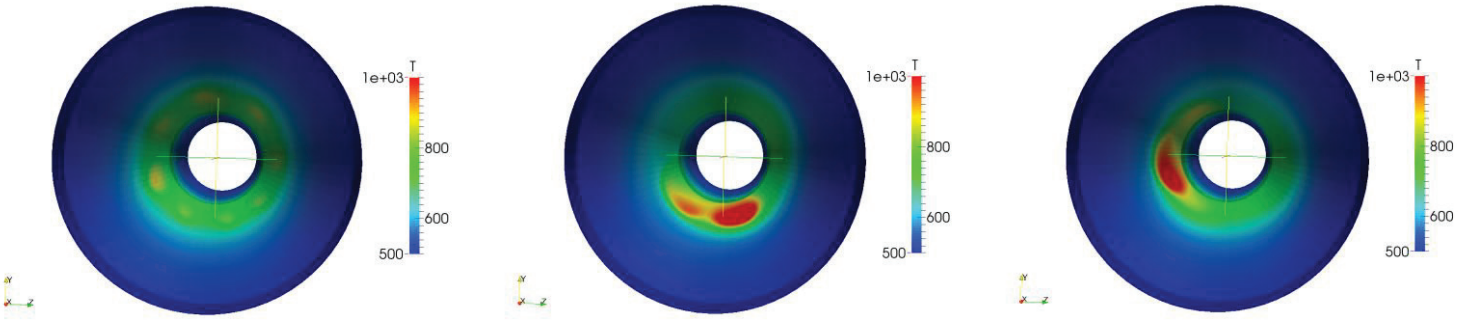

Fig.5.23. Transient temperature profiles at plasma-anode interface of: 2T situation(left), and sheath situation in point 1(middle), point2(right)

5.3 Design optimization and performance analysis

As is mentioned in section 1.1.5, plasma treatments of liquids or nano-sized particles are subject to the flow conditions inside nozzle. Strong arc jet instability inside torch may sometimes result in uncontrolled coating architectures [89]. Coatings of high quality always require a uniform treatment of particles injected into arc jet. However, concerning the simulated flow field and electrode results in the previous sections and the corresponding measurements reported, such kind of flow stability is often hard to achieve due to the complexity of interacting forces. As anode attachment moves both in axial and radial directions, this will further add uncertainties into the arc jet control. A common strategy is to use molecular gases to avoid fluctuation, but this will make arc column more constricted which will in turn cause smaller attachment area and shorter lifetime of electrodes [90].

Future developments and optimizations of plasma torch need to take such issues into consideration to achieve better industrial application. According to the report in [90], multi-electrode plasma torch system has becoming more and more popular due to their advantages over the conventional single cathode-anode system in controlling the arc instability. Applying multi-electrode system could improve deposition efficiency by over 20% with certain kind of spray particles [91].

Multi-electrode plasma torch system could be further categorized by multi-cathode/one-anode and multi-anode/one-cathode systems. The former is usually characterized by three individual cathodes positioned around a particle-feeding tube [92] on the symmetry axis (Fig.5.24), or three cathodes with feeding tube placed perpendicular to plasma flow direction at nozzle outlet to avoid clogging [93]. The latter (Fig.5.25) has an advantage over the former as anode in this configuration is placed faraway from cathodes with several isolated neutral elements in-between. It will force the arc to be reasonably long to reduce fluctuation. However, there are still a lot of restrictions in it. Firstly, the three cathodes should be isolated from each other and keep a reasonable distance to maintain three separate arc

columns. This could be spoiled by the fact that three eccentric arcs could be attracted to each other according to Ampere's force law since they have the same current direction. Secondly, applying different current intensities will generate different magnitudes of Ampere's force every time, therefore anode nozzle diameters should always be adjusted according to operating conditions to avoid unification of arcs. This will cause further operating cost and higher mechanical effort. Finally, it is noteworthy that such kind of configuration could cause a nonuniform distribution of plasma viscosity with three peak zones. This favors a perpendicular particle injection at outlet as a so-called "cage effect" will take place. If a proper angle of injector is chosen, the particle flow will follow the path of low viscosity region between the two peak zones into the center of nozzle, which will then be stuck by the third peak zone in front of it. This is a clear advantage since there will be no more need to use center injection of particles. However, it will still cause problems or even impair deposition efficiency since the three arc jets could still move in radial direction. Any displacement of peak zones caused by such movement could prevent particles from entering the center of nozzle channel since all the three injectors are fixed.

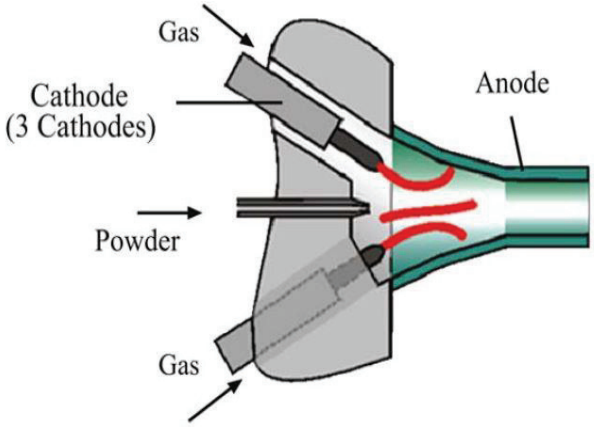

Fig.5.24. Three-cathode/one-anode system with feeding tube located on the axis (Schematic drawing from [90])

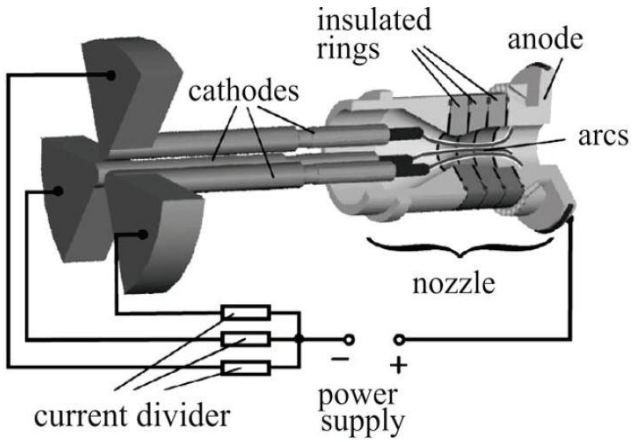

Fig.5.25. Three-cathode/one-anode system with neutral elements between the two electrodes (Schematic drawing of Triplex from [90])

The one-cathode/three-anode configuration provides a good remedy for the disadvantages above. A typical example of it is called *DeltaGun* in [91]. This system (Fig.5.26) consists of a single cathode and three segmented anodes isolated from each other, each has the identical angle of 120°. The neutral element placed in-between are divided into several pieces to make it convenient to adjust voltage. The

main arc column is divided into three sub-arcs when it comes to near-anode regions. The arc stability is further enhanced since the three anode arc roots are fixed, limiting further radial movement. Thus the side-effect of “cage effect” caused by radial movement could be avoided. It makes the operation much more controllable and improves thermal efficiency significantly, since much higher voltage than that of conventional type could be achieved.

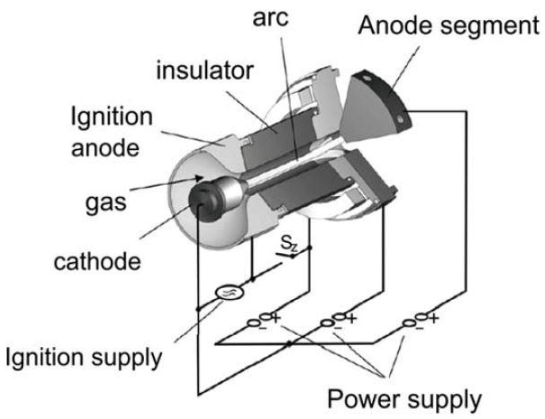

Fig.5.26. One-cathode/three-anode system *DeltaGun* (Schematic drawing from [90])

In this study, a small numerical test is performed based on the same geometry of the previous plasma torch. With all the other boundary conditions consistent with the previous case, the input current is reduced to 400A. The aim of it is to check the performance of the optimized configuration *DeltaGun.* Due to the segmented arrangement of anode, the internal surface of anode ring is newly defined (Fig.5.27) to represent the conducting anode and nonconducting neutral elements in-between. The nonconducting part is shown with blue grid lines where zero gradient condition is applied for the electric potential. All the rest parts namely the three pieces of rotational symmetrical anode surfaces are assigned with the boundary conditions according to Eq. 2.120 as usual.

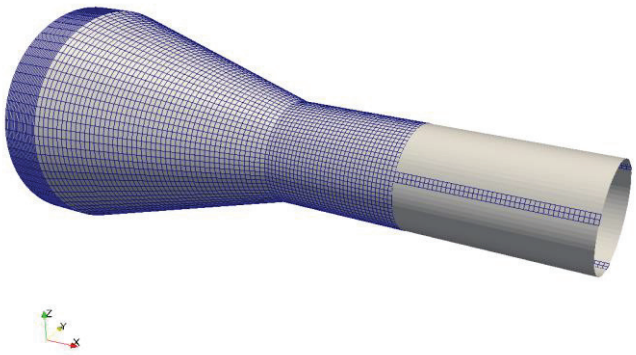

Fig.5.27. Newly defined anode inner surface for *DeltaGun* simulation: grey regions represent conducting surfaces, regions with grid lines represent nonconducting surfaces

From Fig.5.28 and 5.29 it is clear that the arc jet is fixed by three anode “legs” stretching from the main column, in addition to the long and unified arc column by neutral surfaces, such structure helps the main arc jet to be stabilized at the center of nozzle. From theoretical calculation of argon plasma viscosity reported in [42], the value of viscosity under LTE condition experienced its maximum at

T_e=10000K, where the largest hindrance will be provided to prevent the entrance of spray particles into the arc jet center. It is clear from this figure that between all these “legs”, three separated zones are formed, with the temperature of each at the fringes approaching 10000K. Therefore, particles are restricted in these three “cages”. According to our simulated results of temperature, the exact locations of anode attachments do not vary with time, hence three cages remain still, promoting the uniform treatment of spray particles.

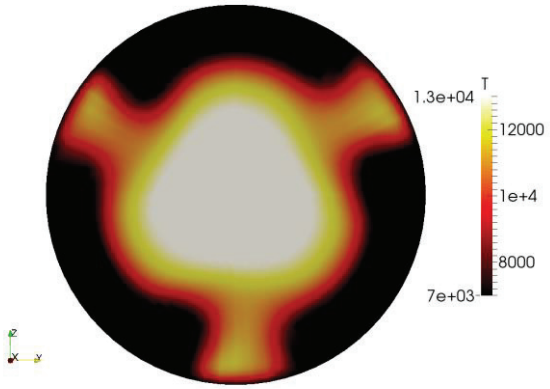

Fig.5.28. Simulated cross section profile of heavy species temperature inside DeltaGun

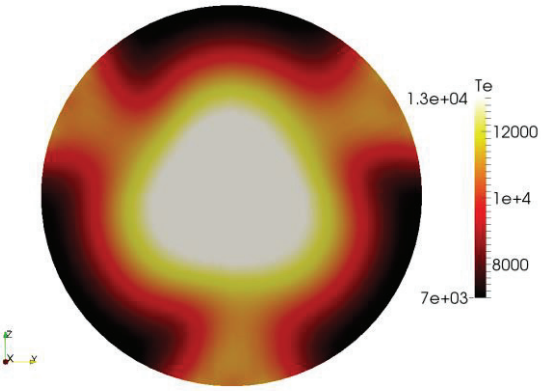

Fig.5.29. Simulated cross section profile of electron temperature inside DeltaGun

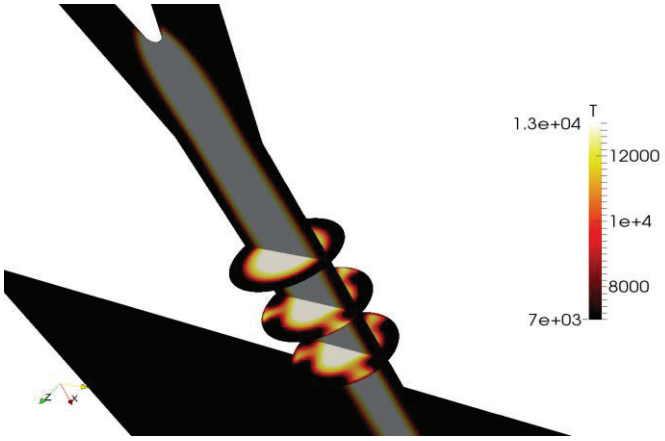

Fig.5.30. Axial and radial heavy species temperature profiles inside DeltaGun

Besides, even though only 400A current is set in this case, the resulting voltage reaches as high as 51V, which is more than the double of the previous 700A case result. This is due to the long arc length shown in Fig.5.30. As a result, the maximal temperature in this case is around 29000K, which shows that it makes better use of total input energy to heat itself than the 700A case with conventional configuration.

Despite its advantages in controlling arc jet stability and improving thermal efficiency, a high anode maximal attachment temperature of over 1100K is obtained in our results (Fig.5.31). This could be contributed to the small area of the three attachment roots and a stable property which promote a large specific heat flux with long residence time. In cases where larger current intensities are applied, this could result in damaging of operating elements or reduction of lifetime.

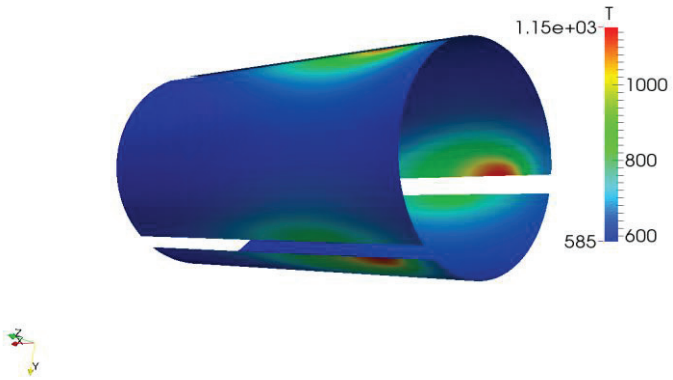

Fig.5.31. Temperature profile of anode inner surface inside DeltaGun

There are several ways to solve the anode over-heating problem. Apart from the conventional cooling strategies such as water-cooled anode and swirl injection, in case arc jet stability condition is not strictly required, for example, plasma cutting and welding, applying an external magnetic field is among the potential options. In this case, the external magnetic field is mainly applied along the axial direction. It is generally induced by permanent magnets or solenoids [94] placed around anode. According to its principle, the axial movement of plasma jet will not be affected by it since velocity and magnetic field are parallel. On the contrary, the radial velocity of arc jet will generate a large Lorentz force with magnetic field, which pulls arc roots around anode surface. In this way, the radial movements of arc will be enhanced, which will reduce the residence time of arc root in a certain place and contribute to less erosion.

In this study, to mimic the induction of magnetic field by a solenoid and analyze its performance in reducing the anode heat load, an external current density J_{ex} is set, which has only components on *y*-*z* plane since the main flow direction is along *x* axis:

$$J_{ex} = J_m(0, \frac{|z|}{\sqrt{y^2+z^2}}, \frac{-|y|}{\sqrt{y^2+z^2}}), \tag{5.2}$$

Where J_m is magnitude of current. In the test cases discussed bellow it is set by 4×10^6, $6\times 10^7 \mathrm{A}/m^2$ respectively. With the utility *funkySetField* provided by *GroovyBC* it is easy to distinguish between the region with and without J_{ex} (Fig.5.32). After the external current density is defined, the calculation of magnetic field inducted with coil around the axis could be obtained by adding an extra term into Eq. 2.51:

$$\frac{\partial \vec{A}}{\partial t} + \nabla\varphi + \frac{1}{\mu_m \sigma_s} J_{ex} - \frac{1}{\mu_m \sigma_s} \Delta \vec{A} = 0. \quad (5.3)$$

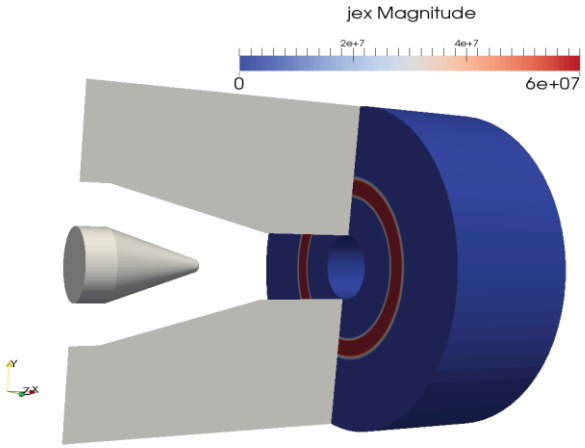

Fig.5.32. Initiation of external coil current density for the simulation with applied magnetic field

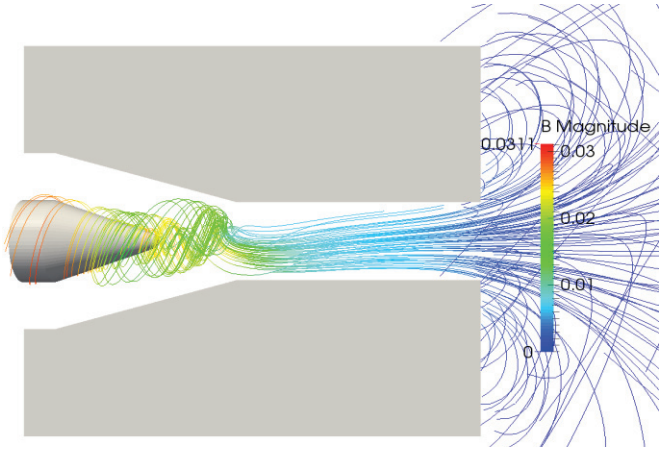

Fig.5.33. Calculated profile of magnetic flux density with J_{ex}=4× 10^6 A/m^2

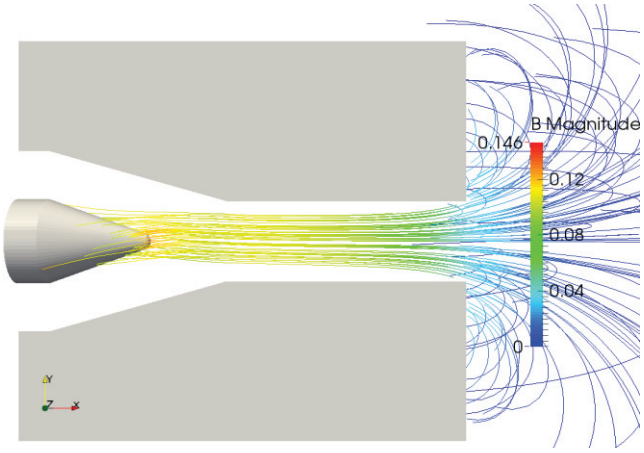

Fig.5.34. Calculated profile of magnetic flux density with J_{ex}=6× 10^7 A/m^2

From Fig.5.33 and 5.34, it is clear that using different intensities of external currents, the magnitudes of induced magnetic field show significant difference. With J_{ex} of 4× 10^6 A/m^2, the maximal magnetic

field including the self-induced component from cathode is 0.03T. When J_{ex} is equal to 6× 10^7 A/m^2, this value reaches 0.146T. In both cases, the maximum value locates around the cathode tip since both fields from cathode and anode intersect here. The results of 4× 10^6 A/m^2 in regions near cathode still present a rotational property since magnetic field magnitudes from both sources are comparable, whereas results of 6× 10^7 A/m^2 show a globally horizontal property of stream lines within the whole nozzle, which indicates that external magnetic field in this case is dominant.

According to the definition of Lorentz force, the horizontal property of magnetic field will contribute to more induced force, which will lead to a larger rotational velocity of arc root on anode. Fig.5.35 and 5.36 show the simulated results of anode attachment temperature with J_{ex} = 4× 10^6 A/m^2 and 6× 10^7 A/m^2 respectively. While the former case doesn't show obvious temperature decrease in comparison with the previously presented attachment temperature of section 5.2 due to the limited influence of J_{ex} on the original magnetic field, the latter shows a significant temperature drop of about 300K compared to the previous maximal value. Besides, the temperature distribution in latter case becomes much more uniform, this is because a larger rotational velocity will reduce the averaged local residence time of arc root which in turn provides more time for cooling. This manifests that using external magnetic field will make rotational movement of arc root controllable when current density J_{ex} can be adjusted. In this respect, this technique is advantageous over swirl injection. However, applying such cooling strategy will add cost and system complexity. Besides, the numerical model for such system is more complicated and should address more sophisticated physical phenomena such as Hall effect and Anomalous transport [95], which are not considered in this scope.

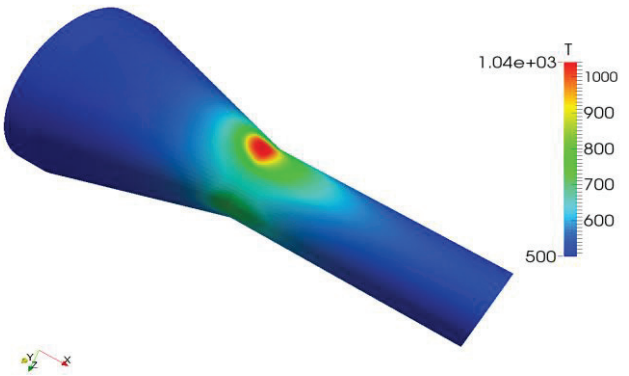

Fig.5.35. Calculated profile of anode inner surface temperature with J_{ex}=4× 10^6 A/m^2

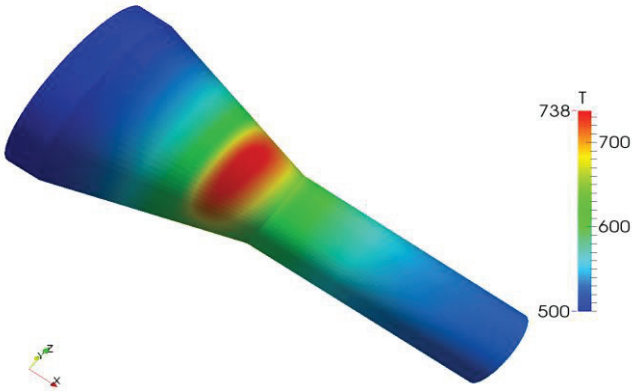

Fig.5.36. Calculated profile of anode inner surface temperature with J_{ex}=6× 10^7 A/m^2

Chapter 6

Conclusions and Future Recommendations

In this dissertation, a self-consistent description of plasma-electrode interaction during arc discharge using finite volume method is presented in detail. The thermal and chemical nonequilibrium arc plasma flow is simulated using one-fluid two-temperature enthalpy equation along with sophisticated reaction rate and ambipolar diffusion model, which is then coupled with the cathode by the sheath layer represented by boundary cells. Due to the complexity of physical process in this extremely small region, it is often treated as a "black box" in many literatures. To achieve a globally self-consistent model including this region, in this scope, the sheath local electrical conductivity is not simply calculated by 2T nonequilibrium regime meant for bulk plasma. An effective value is applied based on local ionization degree to make a smooth transition from emitting to non-emitting area of cathode surface with the help of the Child Law of collisionless sheath. This will spare us from using a presumed current boundary condition or crude cut-off parameter in order to restrict an arc attachment.

To ensure a second-order precision and reduce both numerical instability and false diffusion, Sweby's TVD schemes are applied for the discretization of main parameters. As the interface boundary conditions of each region is indispensable, a detailed survey of electrode surface heat flux for anode and cathode is conducted, along with the interface relation for electric potential, which secures a conservation of total input current throughout the whole surface of electrode.

To validate the interaction model put forward in this study, a series of numerical tests are performed addressing magnetic field results compared by those of Ampère's circuital law, velocity results by analytical solution of Hartmann's flow, the temperature results by experimental measurements of GTAW under atmospheric pressure. All of these three tests obtained quite good agreements with benchmark results. Besides, from the 2D GTAW simulation results it is interesting to find out that the local dimension of plasma net ionization region may be related to that of the LTE region, where both net ionization and recombination can take place.

Based on the precision of this interaction model tested above, 3D full simulation of non-transferred plasma torch is performed. The numerical results of both situations (2T and sheath) are presented, the predicted time-resolved voltage magnitude and fluctuation attained by sheath model is much more realistic when compared with experimental results, which manifests that sheath model may play a decisive role in predicting arc jet fluctuation in a plasma torch by the interaction model. Besides, we have found out that the arc instability in plasma region could lead to the fluctuation of cathode surface temperature and emission current simultaneously, as well as a rotating feature of anode attachment.

However, since arc jet fluctuation is always hard to be controlled in a single cathode/anode system of plasma torch, it leads to difficulties in controlling deposition efficiency during thermal spray. To address this issue, recent developments of design optimization of plasma torch are surveyed, which mainly focused on the multi cathode/one anode and multi anode/one cathode configurations. As the latter has its advantage over the former in fixing arc root and a better utilization of cage effect, the so-called three anode/one cathode system *DeltaGun* is simulated based on the previous geometry. The results show that the predicted voltage in this case is almost fixed and the anode attachments do not change with time. However, although fixed anode root contributes to uniform treatment of spray particle, it leads to a higher possibility of anode erosion, which means auxiliary cooling strategy is indispensable.

In the last part of this dissertation, the issue of controlling the anode attachment temperature is specifically addressed by the method of magnetic stabilization. This technique basically relies on the magnitude of current density applied in the coil around anode to generate a horizontal magnetic field. This magnetic field will then produce Lorentz force along the cross section of nozzle if radial movement of arc is present. Plasma torch with different magnitudes of external circuit current densities is simulated, leading to different magnitudes of applied horizontal magnetic field. The results show that, the larger the external current density is, the lower the maximal anode attachment temperature with a more uniform distribution will turn out to be. Despite of such advantage, additional operating and manufacturing cost needs to be taken into account.

At present our numerical research considers only the basic aspect of plasma-electrode interaction. In real operating conditions, especially when cooling strategy is not sufficient, due to the intensive heating of electrodes by arc jet, metal vapor always appear from electrode surface which modifies plasma properties. This is because the ionization potentials of metal atoms evaporated from electrodes are usually much lower than that of shielding gas atoms, making metal atoms more easily to be ionized. This will make local electron number density of plasma-metal mixtures significantly larger than that of pure gaseous plasmas, where radiative emission coefficient and electrical conductivities can experience the most considerable change. From the experimental measurements of Taishiro et al. [96] it is reported that when helium is mixed with certain portion of iron atoms, the arc will become more constricted and energy efficiency could drop significantly. For a better control and prediction of welding or thermal spray process, transport properties, emission coefficients and diffusion processes with the effect of metal particles should be included.

Besides, in comparison with cathode layers, the physical processes inside anode layers remain poorly understood till now. A unified coupled simulation of plasma-electrode system should not only include cathode sheath, but anode sheath model as well. This will not only help to yield more precise anode attachment results, but also provide theoretical basis for more sophisticated processes such as anode re-attachment in diatomic gaseous plasmas, for which only ambiguous numerical models [12] are developed at present.

Finally, for a better control of an arc jet inside plasma torch, more efforts are needed in plasma torch design and optimization. As is discussed in section 5.3, a fixed arc root can contribute to a more uniform particle treatment and higher deposition efficiency. However, it heats the anode more intensively. A novel plasma torch configuration should achieve a skillful balance among all the important factors including lifetime of elements, system efficiency and operating cost. It will be surely a promising research area since our knowledge of plasma science and its numerical descriptions are constantly growing.

References

[1] A. J. Shirvan, *Modelling of cathode-plasma interaction in short high-intensity electric arc.* Thesis (Ph.D.)—Chalmers University of Technology, 2016.

[2] *Paschen's Law*. Merriam-Webster Online Dictionary. Merriam-Webster, Inc.2013. Retrieved April 10,20113.

[3] K. T. A. L. Burm*, Calculation of the Townsend Discharge Coefficients and the Paschen Curve Coefficients*. Contributions to Plasma Phyiscs.2007;47:177-182.

[4] M. F. Zhukov, I.M. Zasypkin, *Thermal Plasma Torches: Design, Characteristics, Application*. Cambridge Int. Science Publishing, 2007.

[5] K. Kubota, *Numerical Study on Plasma Flowfield and Performance of Magnetoplasmadynamic Thrusters*. Thesis (Ph.D.)—Tokyo Institute of Technology,2009.

[6] N. K. Shi, *Theory of Low-Temperature Plasma*. Springer Series on Atomic, Optical, and Plasma Physics, Volume 95, 2017.

[7] J. L. Marques, G. Forster and J. Schein. *Multi-Electrode Plasma Torches: Motivation for Development and Current State-of-the-Art*. The Open Plasma Physics Journal,2009,2,89-98.

[8] S. A. Wutzke, E. Pfender, and E.R.G. Eckert, *Study of Electric-Arc Behavior with Superimposed Flow*. AIAA J. 1967; 5:707-714.

[9] P. Fauchais, *Understanding plasma spraying*. J.Phys.D: Appl.Phys.2004;37:86-108.

[10] Z. Duan and J. Heberlein*, Arc instabilities in a plasma spray torch*. Journal of Thermal Spray Technology.2002;11:44-51.

[11] S. A. Wutzke, *Conditions Governing the Symptomatic Behavior of an Electric Arcin Superimposed Flow Field*. Thesis (Ph.D.)— University of Minnesota, 1967.

[12] E. Moreau, C. Chazelas, G. Mariaux, and A.Vardelle, *Modeling the Restrike Mode Operation of a DC Plasma Spray Torch*. Journal of Thermal Spray Technology.2006;15:524-530.

[13] M. Alalya, C. Chazelas and G. Mariaux, *Arc-Cathode Coupling in the Modeling of a Conventional DC Plasma Spray Torch*. Journal of Thermal Spray Technology.2015;24:3-10.

[14] J. P. Trelles, J. V. R. Heberlein and E. Pfender, *Modelling of the arc reattachment process in plasma torches*. J.Phys D: Appl. Phys.2007;40:5937.

[15] V.I. Kristya, *Analytical Calculation of Cathode Spot Parameters on the Electrode Surface in Arc Discharge*. Journal of Surface Investigation. X-ray, Synchrotron and Neutron Techniques.2009;3:289-291.

[16] R. Morrow and J. J. Lowke, *A one-dimensional theory for the electrode sheaths of electric arcs*. J.Phys. D: Appl.Phys. 1993;26:634-642.

[17] K. C. Hsu and E. Pfender, *Analysis of the cathode region of a free-burning high intensity argon arc.* J.Appl. Phys.1983; 54:3818-3824.

[18] X. Zhou and J. Heberlein, *Analysis of the arc-cathode interaction of free burning arcs*. Plasma Sources Sci. Technol.1994; 3:564-574.

[19] M.S. Benilov and G.V. Naidis, *What is the mathematical meaning of Steenbeck's principle of minimum power in gas discharge physics?* J.Phys.D: Appl.Phys.2010;43: 175204.

[20] F. Cayla, P. Freton, and J. J. Gonzalez, *Arc/cathode interaction model.* IEEE Trans. Plasma Sci. 2008; 36:1944-1954.

[21] J. J. Gonzalez, F. Cayla, P. Freton and P. Teulet, *Two-dimensional self-consistent modelling of the arc/cathode interaction*. J. Phys.D: Appl.Phys. 2009;42:145204.

[22] J. Haidar and A.J.D. Farmer, *Large effect of cathode shape on plasma temperature in high-current free-burning arcs.* J. Phys. D: Appl. Phys. 1994; 27:555-560.

[23] P.Y. Zhu, J.J. Lowke and R. Morrow, *A unified theory of free burning arcs, cathode sheaths and cathodes*. J. Phys.D: Appl. Phys. 1992;25:1221-1230.

[24] J. J. Lowke, *A Unified Theory of Arcs and their Electrodes*. J. Phys IV FRANCE. 1997; 7:283-294.

[25] J. J. Lowke, R. Morrow and J. Haidar, *A simplified unified theory of arcs and their electrodes*. J. Phys.D: Appl. Phys.1997;30:2033-2042.

[26] P. Maruzewski, A. Martin, M. Reggio and J. Y. Trepanier, *Simulation of arc-electrode interaction using sheath modelling in SF6 circuit-breakers*. J. Phys.D: Appl.Phys.2002;35:891-899.

[27] A. J. Shirvan, I. Choquet, H. Nilsson and H. Jasak, *Coupling boundary condition for high-intensity electric arc attached on a non-homogeneous refractory cathode*. Computer Physics Communications. 2017(In Press, Corrected Proof).

[28] M. Baeva, M.S. Benilov, N.A. Almeida and D. Uhrlandt, *Novel non-equilibrium modelling of a DC electric arc in argon*. J.Phys.D: Appl.Phys.2016;49:245205.

[29] V. A. Nemchinsky and L. N. Peretts, *Anode sheath in a high-pressure, high-current arc*. Soviet Physics- Technical Physics. 1977;22: 1083-1087.

[30] P. Y. Zhu, J. J. Lowke, R. Morrow and J. Haidar, *Prediction of anode temperatures of free burning arcs*, J. Phys.D: Appl.Phys.1995;28:1369-1376.

[31] G. Heller, *Dynamical Similarity Laws of the Mercury High Pressure Discharge*. Physics 1935; 6:389.

[32] C. H. Kruger, *Nonequilibrium in confined-arc plasmas*. Phys Fluids. 1970; 13:1737-1746.

[33] R. J. Giannaris, F. P. Incropera, *Nonequilibrium effects in atmospheric argon plasma*. J. Quant. Spectrosc. Radiat. Transf. 1971; 11:291-307.

[34] K. S. Drellishak, C. F. Knopp and A. B. Cambel. *Partition functions and thermodynamic properties of argon plasma*. Technical documentary report No. AEDC-TDR-63-146.1963.

[35] J. Heiermann, *Ein Finite-Volumen-Verfahren zur Lösung magnetoplasmadynamischer Erhaltungsgleichung*. Thesis (Ph.D.) —University of Stuttgart, 2002.

[36] W.Lotz. An Empirical Formula for the Electron-Impact Ionization Cross-Section. Zeitschrift für Physik 206, 205--211 (1967).

[37] M. Baeva, R. Kozakov, S. Gorchakov and D. Uhrlandt. *Two-temperature chemically non-equilibrium modelling of transferred arcs*. Plasma Sources Sci. Technol.2012;12: 055027.

[38] M. I. Hoffert and H. Lien, *Quasi-One-Dimensional, Nonequilibrium Gas Dynamics of Partially Ionized Two-Temperature Argon*. The Physics of Fluids.1967;10:1769.

[39] V. Rat, P. Andre, J. Aubreton, M.F. Elchinger, P. Fauchais and A. Lefort , *Transport properties in two-temperature plasma :Theory and Application*. Phys. Rev. E.2001; 64:026409.

[40] C. Boie, *Numerische Simulation magnetoplasmadynamischer Eigenfeldtriebwerke mit hoch-auflösenden adaptiven Verfahren*. Shaker Verlag GmbH, 2000.

[41] M. I. Boulos, P. Fauchais and E. Pfender. *Thermal Plasmas: Fundamentals and Applications*. Vol.1, Springer Science+Businness Media,1994.

[42] J. P. Trelles, *Finite element modeling of flow instabilities in arc plasma torches*, Thesis (Ph.D.) — University of Minnesota, 2007.

[43] P. Freton, J. J. Gonzalez, Z. Ranarijaona and J. Mougenot, *Energy equation formulations for two-temperature modelling of 'thermal' plasmas*. J. Phys. D: Appl.Phys. 2012;45:465206.

[44] J. J. Lowke, *Prediction of arc temperature profiles using approximate emission coefficients for radiation losses*. J. Quant.Spectrosc. Radiat.Transfer.1974;14:111-122.

[45] R. Siegel and J. R. Howell, *Thermal Radiation Heat Transfer*. New York:McGraw-Hill,1981.

[46] R. W. Liebermann and J. J. Lowke, *Radiation emission coefficients for sulfur hexafluoride arc plasmas.* J. Quant.Spectrosc. Radiat. Transfer.1976;16:253-264.

[47] Y. Vitel, A. Siyacoun , L. Giry and G. Louvet, *The continuum absorption of argon, krypton and xenon denseplasmas produced in flashlamps.* J. Phys. B: At. Mol. Opt.Phys.1993;26:4333-4342.

[48] L. M. Biberman, G. E. Norman and K.N. Ulyanov, *On the Calculation of Photoionization Absorption in Atomic Gases*. Opt.and Spectr. 1961; 10:297.

[49] L. G. D'yachkov, *Simple formula for the average Gaunt factor*. J. Phys. B: At.Mol.Opt.Phys.1990;23: 429-432.

[50] C. M. Dixon, J. D. Yan and M. T. Fang, *A comparison of three radiation models for the calculation of nozzle arcs*. J.Phys. D: Appl. Phys.2004;37:3309-3318.

[51] W. K. Widger, and M. P. Woodall, *Integration of the Planck blackbody radiation function*. Bulletin of the Am. Meteorological Society.1976; 57:1217-1219.

[52] J. Menart and S. Malik, *Net emission coefficients for argon-iron thermal plasmas*. J. Phys. D: Appl. Phys. 2002; 35:867-874.

[53] K.D. Goodfellow, *A Theoretical and Experimental Investigation of Cathode Processes in Electric Thrusters.* Thesis (Ph.D.) —Faculty of Graduate School, University of Southern California, 1996.

[54] P. A. Schoeck, *An investigation of the energy transfer to the anode of high intensity arcs in argon*. Thesis (Ph.D.) —University of Minnesota, 1961.

[55] P. A. Schoeck, *An investigation of anode energy balance of high intensity arcs in argon*. Modern Development in Heat Transfer. New York: Academic Press,1963:353-400.

[56] A. Fridman and Y. I. Cho, *Transport Phenomena in Plasma - Advances in Heat Transfer*, Elsevier, 2007.

[57] H. A. Dinulescu and E. Pfender, *Analysis of the anode boundary layer of high intensity arcs*. J.Appl.Phys.1980;51:3149.

[58] F. Cayla, P. Freton and J. J. Gonzalez, Arc/cathode interaction model. IEEE Trans. Plasma Sci. 2008; 36:1944-1954.

[59] S. Lichtenberg, L. Dabringshausen, O. Langenscheidt and J. Mentel. *The plasma boundary layer of hid-cathodes: modelling and numerical results*. J.Phys.D: Appl.Phys.2005;38:3112.

[60] A. Fridman, *Plasma Chemistry*. Cambridge University Press, August 2009.

[61] J. Wendelstorf. *Ab initio modelling of thermal plasma gas discharges (electric arcs).* Thesis (Ph.D.) — Braunschweig University of Technology, 2000.

[62] A. Anders, *Cathodic Arcs: From Fractal Spots to Energetic Condensation*. Springer-Verlag New York. 2008.

[63] V. F. Puchkarev, and M. B. Bochkarev, *Cathode spot initiation under plasma*, J. Phys, D: Appl. Phys.1994;27:1214-1219.

[64] I. V. Uimanov, *A two-dimensional nonstationary model of the initiation of an explosive center beneath the plasm a of a vacuum arc cathode spot*. IEEE Trans. Plasma Sci.2003;31:822-826.

[65] J. P. Trelles, *Computational study of flow dynamics from a dc arc plasma jet*. J. Phys.D: Appl.Phys,2013;46: 255201.

[66] F. R. Menter, M. Kuntz and R. Langtry, *Ten Years of Industrial Experience with the SST Turbulence Model*. Turbulence, Heat and Mass Transfer 4,2003.

[67] W. P. Jones, and B. E. Launder, *The prediction of laminarization with a two-equation model of turbulence*. International Journal of Heat and Mass Transfer.1972;15:301-314.

[68] D. C. Wilcox, *Re-assessment of the scale-determining equation for advanced turbulence model*, AIAA Journal. 1988; 26: 1299-1310.

[69] C. J. Greenshields, *OpenFOAM-The Open Source CFD Toolbox-Programmer's Guide*, OpenFOAM Foundation Ltd. 2015.

[70] J. B. Scarborough, *Numerical Mathematical Analysis*. Johns Hopkins University Press, Baltimore.1958.

[71] F. S. Lien, and M. A. Leschziner, *Upstream Monotonic Interpolation for Scalar Transport with Application to Complex Turbulent Flows*. Int. J. Numer. Methods Fluids.1993;19:527-548.

[72] P. K. Sweby, *High Resolution Schemes Using Flux Limiters for Hyperbolic Conservation Laws*. SIAM J. Numer. Anal.1984;21:995-1011.

[73] B. V. Leer, *Towards the Ultimate Conservative Difference Scheme II. Monotinicity and Conservation Combined in a Second-Order Scheme*. J. Comput. Phys. 1974; 14:361-370.

[74] P. L. Roe, *Some Contributions to the Modelling of Discontinuous Flows*. Lectures in Applied Mechanics. Springer Verlag, Berlin.1985;22:163-193.

[75] B. P. Leonard, *Simple High-accuracy Resolution Program for Convective Modelling of Discontinuities.* Int. J. Numer. Methods Fluids.1988;8:1291-1318.

[76] L. Davidson, *A Pressure Correction Method for Unstructured Meshes with Arbitrary Control Volumes*. Int. J. Numer. Methods Fluids. 1996; 22:265-281.

[77] S. R. Mathur, and J. Y. Murthy, *A Pressure-Based Method for Unstructured Meshes*. Numer. Heat Transfer Part B. 1997; 31:195-215.

[78] A. Haselbacher, *A Grid-transparent Numerical Method for Compressible Viscous Flows on Mixed Unstructured Grid*. Ph.D. Thesis, Loughborough University, 1999.

[79] D. M. Young. *Iterative Solution of Large Linear Systems*. Academic Press, 1971.

[80] R. I. Issa, *Solution of the Implicitly Discretized Fluid Flow Equations by Operator-Splitting*. Journal of Computational Physics.1985; 62:40-65.

[81] M. Peric. *A Finite Volume method for the prediction of three-dimensional fluid flow in complex ducts.* Thesis (Ph.D.) —Imperial College, University of London,1985.

[82] K. R. Cramer and Shih-l Pai, *Magnetofluid Dynamics for Engineers and Applied Physicists*. Scripta Publishing Company. ISBN 0-07-013425-1.1973.

[83] J. A. Shercliff, *Steady motion of conducting fluids in pipes under transverse magnetic fields.* Mathematical Proceedings of Cambridge Philosophical Society. 1953; 49:136-144.

[84] G. N. Haddad and A. J. D. Farmer, *Temperature Measurements in Gas Tungsten Arcs.* Welding Journal. 1985; 64:339-342.

[85] J. Haidar and A. J. D. Farmer*, Surface temperature measurements for tungsten-based cathodes of high-current free-burning arcs.* J. Phys. D: Appl. Phys. 1995; 28:2089-2094.

[86] J. A. Sillero, D. Ortega, E. M. Serrano and E. Casado, *An experimental study of thoriated tungsten cathodes operating at different current intensities in an atmospheric-pressure plasma torch*. J.Phys.D: Appl.Phys.2010;43:185204.

[87] V. Rat and J. F. Coudert, *Acoustic stabilization of electric arc instabilities in non-transferred plasma torches*. Appl. Phys.Lett. 2010; 96:101503.

[88] C. K. Li et al., *Scaled laboratory experiments explain the kink behavior of the Crab Nebula jet*. Nature Communications.2016.

[89] P. Fauchais, R. Etchart-Salas, V. Rat, J. F. Coudert, N. Caron and K. Wittmann-Teneze, *Parameters controlling liquid plasma spraying: Solutions, sols, or suspensions.* Journal of thermal spray technology. 2008; 17:31-59.

[90] J. L. Marqués, G. Forster and J. Schein, *Multi-Electrode Plasma Torches: Motivation for Development and Current State-of-the-Art.* The Open Plasma Physics Journal, 2009, 2: 89-98.

[91] M. Dzulko, *Entwicklung des Mehranoden DC-Plasmagenerators „Delta Gun".* Thesis (Ph.D.) — University of Federal Armed Forces Munich,2007.

[92] H. Fukanuma. Japanese Patent 230300JP.04/24/1988,1988.

[93] K. Landes. Plasmaspritzgerät. German Patent DE 4105408C1,21.02,1991.

[94] R. N. Szente, R. J. Munz and M. G. Drouet, *Arc velocity and cathode erosion rate in a magnetically driven arc burning in nitrogen.* J. Phys.D: Appl. Phys.1988;21:909-913.

[95] E. Y. Choueiri, A. J. Kelly and R. G. Jahn, *Current-driven plasma acceleration versus current-driven energy dissipation.* III- *Anomalous Transport*. NASA Technical Report. 1992.

[96] S. Tashiro, K. Tanaka, T. Iwao, F. Koshiishi, K. Suzuki and K. Yamazaki, *Plasma properties of helium gas tungsten arc with metal vapour*. Sci. Technol. Weld. Join. 2007; 12:202-207.